NUMERICAL SIMULATION OF SPRAY COMBUSTION CONSIDERING SOOT FORMATION AND THERMAL RADIATION

Submitted

By

PRAKASH GHOSE

Doctor of Philosophy
(Engineering)

DEPARTMENT OF POWER ENGINEERING
FACULTY COUNCIL OF ENGINEERING AND TECHNOLOGY
JADAVPUR UNIVERSITY
KOLKATA, INDIA
YEAR: 2016

JADAVPUR UNIVERSITY

KOLKATA -700 032, INDIA

INDEX NO. 287/12/E

List of Publications

1. Title of the Thesis

Numerical Simulation of Spray Combustion Considering Spray Formation and Thermal Radiation.

2. Name, Designation & Institution of the Supervisors:

Prof. Amitava Datta, Professor, Department of Power Engineering, Jadavpur University Salt Lake Campus, Kolkata, INDIA

Prof. Achintya Mukhopadhyay, Professor, Department of Mechanical Engineering, Jadavpur University, Jadavpur, Kolkata, INDIA

3. List of Publications (Referred Journals):

i. **Prakash Ghose**, Amitava Datta, Achintya Mukhopadhyay. Effect of dome shape on static pressure recovery in a dump diffuser at different inlet swirl. ***International Journal of Emerging Technology and Advanced Engineering***. Volume 3, Special Issue 3: ***ICERTSD*** 2013, Feb 2013, pages 465-471.

ii. **Prakash Ghose**, Jitendra Patra, Amitava Datta , Achintya Mukhopadhyay**.** Effect of Air Flow Distribution on Soot Formation and Radiative Heat Transfer in a Model Liquid Fuel Spray Combustor firing Kerosene. ***International Journal of Heat and Mass Transfer, (Elsevier),*** 74 (2014) 143-155.

iii. **Prakash Ghose**, Amitava Datta, Achintya Mukhopadhyay. Modeling non-equilibrium combustion chemistry using constrained equilibrium flamelet model for kerosene spray flame. **ASME Journal of Thermal Science and Engineering application,** MARCH 2016, Vol. 8 / 011004-1-10.

iv. **Prakash Ghose**, Amitava Datta, Achintya Mukhopadhyay. Effect of pre-diffuser angle on the static pressure recovery in flow through a casing-liner annulus at various swirl levels. **ASME Journal of Thermal Science and Engineering application,** MARCH 2016, Vol. 8 / 011017-1-7.

v. **Prakash Ghose**, Jitendra Patra, Amitava Datta , Achintya Mukhopadhyay (2016)**:** Prediction of Soot and Thermal Radiation in a Model Gas Turbine Combustor Burning Kerosene Fuel Spray at Different Swirl Levels. **Combustion theory and modelling,** DOI: 10.1080/13647830.2016.1147607

4. List of Patents: **NIL**

5. List of Presentations in National/ International Conferences:

i. **Prakash Ghose,** A. Datta, A. Mukhopadhyay, R. Ganguly, S. Sen. Comparison of Cold flow analysis in a swirled dump combustor with standard k-ε and RNG k-ε turbulent models", National Conference on Advances in Simulation and Optimization Techniques in Mechanical Engineering, 2012 (KIIT University, Bhubaneswar).

ii. **Prakash Ghose,** Amitava Datta, Achintya Mukhopadhyay. Effect of pre-diffuser angle on the static pressure recovery in flow through casing-liner annulus of a gas turbine combustor at various swirl levels in 11th international ISHMT-ASME Heat and mass transfer conference, December 28-31, 2013, IIT Kharagpur, India.

iii. **Prakash Ghose,** Amitava Datta, Achintya Mukhopadhyay. Numerical prediction of kerosene spray combustion using different combustion models: a comparison in 11th international ISHMT-ASME Heat and mass transfer conference, December 28-31, 2013, IIT Kharagpur, India

iv. **Prakash Ghose,** Amitava Datta, Achintya Mukhopadhyay, prediction of kerosene spray combustion in a model gas turbine combustor at different inlet swirl and turbulence levels on 2nd KITSAAT International symposium held on 20th & 21st Dec 2013, KIIT University Bhubaneswar.

CERTIFICATE FROM THE SUPERVISOR

*This is to certify that the thesis entitled "**Numerical Simulation of Spray Combustion Considering Spray Formation and Thermal Radiation**" submitted by **Shri Prakash Ghose** who got his name registered on **22nd March, 2012** for the award of **Ph.D. (Engineering)** degree of **Jadavpur University**, is absolutely based upon his own work under the supervision of **Prof. Amitava Datta** and **Prof. Achintya Mukhopadhyay** and that neither the thesis nor any part of the thesis has been submitted for any degree/diploma or any other academic award anywhere before.*

Signature of the Supervisor
and Date with Official Seal

Signature of the Co-Supervisor
and Date with Official Seal

Dedicated

to

Parents

ACKNOWLEDGEMENT

The author takes this opportunity to express his profound gratitude and deep regards to his supervisors, Dr. A. Datta and Dr. A. Mukhopadhyay for their valuable suggestions, exemplary guidance, monitoring and constant encouragements throughout the course of this dissertation work.

The author highly acknowledges the GTRE, a research laborotary of DRDO, since a great financial support has been given by them towards my research.

The author would like to thanks Mr. Jitendra Patra and Dr. Bireswar Paul. Who extended their support during each stage of this thesis work.

The author expresses his thanks to Dr. Ranjan Ganguly for his valuable suggestion during the work.

The author wishes to express thanks to Mr. Malay Ghosh, for his assistance at various stages of the experiments. The author is thankful to Mr. Atish Nandy, who extended his support during each stage of this thesis work.

The author wishes to express his profound gratitude to his wife, Soma for maintaining the necessary atmosphere of understanding and providing the encouragement and support in spite of being in the midst of hardships and taking all cares of his daughter Pallavi, whom he missed a lot during the tenure of research. The author specially thanks to his brother Bikash for continuous encouragement during the work.

Finally, the author is grateful to all his well wishers and other concerned persons who helped him directly or indirectly to complete the present work.

(Prakash Ghose)

List of Figures

List of tables

Abstract

The main aim of this work is to simulate the combustion process through a model gas turbine combustor. The effects of mass flow distribution and inlet air swirl on soot formation, temperature distribution, species concentration and the efficiency of combustor have been discussed thoroughly in this work. Moreover the selection of the turbulent model among different two equation turbulent models for the simulation of swirl flow has been studied. It is validated with the experimental results obtained by Rahim et al.[126]. It has been found that Realizable k-ε model is the best suited turbulent model for mild swirled flow. This turbulent model is used throughout the simulation of combustion processes. LISA model is used to simulate the atomization process of a pressure swirl atomizer. Eulerian-Lagrangian frame has been considered to simulate the interaction in between droplet phase and continuous phase.

Modelling of soot is one of the major contributions of this work. A semi-empirical two equation soot model is used [98] to simulate the soot in flame. The source term has been modified for kerosene fuel ($C_{12}H_{23}$). It is compared with the experimental results of Young et al. [142] and the computational results of acetylene and PAH model of Wen et al. [104]. In this work, benzene and phenyl are not considered as surface growth species. Here acetylene is considered as a precursor and surface growth species as well. The predictions through our proposed acetylene model becomes very good with experiments. However the constants proposed by Brookes and Moss for methane fuels are modified to a suitable value. Discrete ordinate (DO) radiation model is used to simulate radiation effect. The gas is considered as participating media. Effect of soot in radiation also has been incorporated.

Three different combustion models such as: Eddy dissipation model, Laminar flamelet model and Constrained equilibrium model are compared with the experimental results which has been obtained from the experiments conducted in our laboratory. It has been found that Eddy dissipation model predicts very poor as compare to other two models. However a major conclusion from this part is that, the Constrained equilibrium model can predicts good if a proper value of RFL (rich

flammability limit) will be chosen. On the other hand Laminar flamelet model does not need any such uncertain parameters and still it predicts nicely. But the computational economy of this model is little poor as compared to Constrained equilibrium model. However a detailed chemical kinetics is required to simulate in Laminar flamelet model.

The effect of airflow distribution on flame formation and heat transfer through model gas turbine combustor has been studied. It has been found that more air supply through primary swirled inlet decreases the flame length. When the primary air increases to 50%, the flame is broken. Therefore with a higher supply of primary air, the centreline temperature decreases. Moreover in same case the soot formation also becomes lesser but the wall temperature increases. Due to the higher wall temperature heat loss increases through wall. Therefore the overall combustor efficiency decreases but the pattern factor at outlet becomes better. The effect of radiation on injector tip has also been studied.

The effect of swirl level on soot and heat transfer also has been studied. It has been depicted that, at lower swirl, the flame length increases. As the swirl level increases the flame length become shorter. At a certain swirl level (60^o vane angle), the flame is broken and the centreline temperature decreases. However the soot formation does not affect much with swirl level. But at higher swirl the soot laden zone become closer to injector tip. The injector plane area also becomes hotter at swirl level increases. The combustor efficiency is being better at lower swirl due to comparatively a small heat loss has been occurred in this case. The species mass fraction distributions along the axis also have been studied. The effect of radiation on injector tip has also been studied.

Table of Contents

Nomenclature

A	surface area, m^2
A	activation energy
a_k	weighting factor
C_d	coefficient of discharge
C_{Drag}	drag coefficient
C	species concentration in the continuous phase
C_L	ligament constant
c_p	specific heat, J/kg-K
D	diameter of the combustor, m
D	diffusivity
Da	Damkohler number
DG	dump gap
d	diameter, m
d_L	ligament diameter, m
d_o	mean droplet diameter, m
$d_{p_{soot}}$	mean diameter of soot particle, m
F_D	drag force, N
G	acceleration due to gravity, m/s^2
G_T^0	Gibbs function
ΔH_v	latent heat of vaporization, J/kg
h , H	enthalpy
h_c	heat transfer coefficient, W/m^2-K
h_D	mass transfer coefficient, m/s
I	radiation intensity, W/m^2.sr
K_p	equilibrium constant
k	turbulent kinetic energy, m^2/s^2
k_w	wave number
LS	length scale
M	soot mass concentration, kg/m^3
MW	molecular weight
m	mass, kg
$\dot{m}$	mass flow rate, kg/s
N	particle number density, $1/m^3$
N	spread parameter
N_A	Avogadro number
Oh	Ohnesorge number
p	pressure, N/m^2
$p_{d\text{-}in}$	inlet dynamic pressure
P	probability density function
Q	ratio between gas and liquid density
q	radiative heat flux, W/m^2

R	universal gas constant
Re	Reynolds number
R_u	Universal gas constant
S	source term
Sc	Schmidt number
SN	swirl number
STP	standard temperature and pressure
T	temperature, K
TI	turbulent intensity
t	liquid sheet thickness, m
u , U	velocity, m/s
u'	fluctuating velocity
We	Weber number
w_i	quadrature weight
X	mole fraction
X	axial direction
Y	mass fraction
Y_d	mass fraction of droplet class
Z	Axial distance
z	path length

Greek symbols

$\bar{\tau}_{ij}$	stress tensor
Γ	diffusivity. m^2/s
ε	rate of dissipation of turbulent K.E.,
θ	spray cone half angle
κ	absorption coefficient
λ	thermal conductivity, W/m K
μ	dynamic viscosity
μ_t	dynamic eddy viscosity
ν	kinematic viscosity, m^2/s
ξ	mixture fraction
ξ''	variance of mixture fraction
ρ	density, kg/m^3
σ	Prandtl/Schmidt number
σ_s	surface tension of the liquid
ϕ	scalar variable
ϕ'	fluctuation of scalar variable
χ	scalar dissipation rate, s^{-1}
$\dot{\omega}$	reaction rate
ω_r	growth rate of sinuous wave
δ_{ij}	chroneker delta
χ	scalar dissipation rate

Subscript

b	blackbody
$crit$	critical
d	droplet
eff	effective
f	fuel
g	gas
i,j,k	coordinate direction
in	inlet
k	k^{th} species
inj	injection
l	liquid / fuel
lam	laminar
mix	mixture
or	orifice
rad	radiation
st	stoichiometric
t	turbulent
ϕ	scalar variable
θ	tangential direction
0	reference value
w	wall
z	in z-direction

Super script

k	k^{th} species

Chapter 1

Introduction

1.1 Motivation for this work

Study of combustion has a great practical relevance in various spheres of the society even today. Starting from the tiny domestic burner for cooking of food, to heating of rooms and accessories, running automobiles, and finally in the huge burners of engines for aircrafts, marine engines and power plants– combustion plays a vital role in many modern devices, either directly or indirectly.

Controlled combustion is an intricate phenomenon, as it includes various physical transports and complex chemical reactions together in a coupled manner. Today, there is a global interest towards the clean power generation addressing the concern towards sustainability. Therefore, tremendous efforts have been put by the researchers to improve the combustion system that focus on reducing emissions, increasing combustion efficiency and lowering costs without forfeiting the reliability.

Gas turbine is a power generating device which is used in aircraft and marine engines and also in stationary electrical power plants. In the gas turbine combustor, chemical energy of the fuel is converted to heat energy for its subsequent conversion to mechanical work in the turbine. The gas turbine combustors operate at a very high air-fuel ratio in order to keep the turbine inlet gas temperature within the metallurgical limit. Normally the air supplied from the compressor is split and admitted at different points of the combustor as primary, secondary and dilution air. Out of them, the primary air oxidizes the fuel and helps in stabilizing the flame, secondary air completes the combustion of left-over combustible species and the dilution air decreases the gas temperature leaving the turbine by maintaining the right

pattern factor [1,2,3]. Either a single or a set of fuel injectors are placed centrally to the combustor to supply the fuel continuously, particularly in case of aviation gas turbines. Stationary gas turbines often use gaseous fuels, like natural gas, for their operation.

The development of the aviation gas turbine engines saw a remarkable progress in the last century. Amongst the various components of the engines, combustors have experienced many important modifications. The major criteria, over which the developments in gas turbine combustor take place, are high combustion efficiency, stabilization of flame, ready re-ignition following flame extinction and reduced emission of the pollutants. In addition, significant research work is being carried out on the use of alternative liquid fuels in gas turbines– mainly derived fuels like bio-ethanol and biodiesel, and on the material aspects of various parts.

However, despite the keen interest on alternate fuels in gas turbine applications for the future, the present day aviation engines almost entirely run on kerosene based jet fuels. The fuel is sprayed in the stream of air using an atomizer and is burned as a non-premixed flame. Considering the present day concern over carbon loading on the environment, a lot of emphasis is being given on reducing the specific fuel consumption of the engines. The big players in the field are competing with one another in developing engines with higher fuel efficiency and therefore lower emission. One important means of achieving this target is to make the engine lighter in weight using suitable materials. Ceramic and composite materials are being developed for various parts. However, one important concern in the development of the materials is the temperature of the gas which they have to withstand.

Computational fluid dynamics is being used widely to study the combustion phenomena and the resulting temperature distribution in the gas turbine combustor. Simulation results can reduce the cost of development to a great extent by obviating the challenge of cut and try method. In addition to the complex turbulent, swirling flow and the existence of the two phases (continuous gas phase and discrete liquid phase) in the combustor, formation of soot and energy exchange due to radiation play significant roles in the prediction of gas turbine combustion behaviour. Both the gas temperature leaving the combustor and the temperature of the different combustor parts (like combustor wall, fuel injector and primary air swirler) get affected by the soot distribution in the flame and the radiative energy exchange. Therefore, numerical

studies on spray combustion considering soot formation and radiative energy exchange in a combustor firing kerosene fuel have been taken up as focus of the present research.

1.2 State of the art literature review

A host of research works have been carried out in the field of gas turbine combustion by various researchers across the globe. The complex flow pattern in the combustor has been analyzed using cold flow analyses, either experimentally or numerically. In order to stabilize the flame in the combustor, the primary air is generally admitted through a swirler, which establishes a recirculating zone close to the burner. The turbulent, swirling flow imposes additional modelling challenge. The reacting flow analysis is even more challenging, since it includes chemical reactions that largely affect the physical properties of gas as well as liquid phase due to local heat generation. Generally gas turbine combustors are fed with liquid fuel through an injector that atomizes the fuel into fine droplets. Various modelling techniques have evolved in spray combustion modelling to account the combustion of the liquid fuels. Moreover during combustion not only various species in the gas phase are formed but solid particles, called soot, are also formed. Presence of soot particles in flame affects the temperature distribution throughout the combustor as they strongly participate in the radiation exchange. Many researchers studied the combustion processes including atomization, combustion, soot and radiation by using various computational methods. In this section, some important studies related to the cold flow and reacting flow in the combustor have been discussed.

1.2.1 Flow patterns inside the combustor and Turbulent models

A lot of research in the area of gas turbine combustion has been done over the last few decades to improve the performance characteristics of the combustors [4,5]. In order to minimize the flow losses, flame stability, heat loss, emission and to increase the efficiency, the flow pattern inside the combustor either by experimentation or by cold flow simulation has been studied by many researchers.

In gas turbine combustor, the primary air enters into the combustor through a set of inclined vanes called swirlers. Due to the swirl imparted to flow by the vanes, the

pressure near the combustor axis falls to create an adverse pressure gradient; as a consequence of which a central toroidal recirculation zone is formed. Swirl flows are used widely in gas turbine combustors to promote flame stability, improve combustion efficiency and control emission of pollutants [6].

Effects of inlet swirl levels on isothermal flow pattern in gas turbine combustors, either by experimentation or through computation, have been studied by Mondal et al. [2], Yehia et al. [7], Vasudevan and Ganesan [8], Favaloro et al. [9], Benim et al. [10], Koutmos and McGuirk [11], Kenbar et al. [12]. From their work it can be concluded that the central toroidal recirculation zone (CTRZ) is formed in the combustor above a certain swirl level of the inlet flow, due to the augmentation in the tangential momentum. The central recirculation pulls back the gas from a downstream location towards upstream and helps to stabilize the flame. Foster et al. [13] used a range of swirl number SN=0 to SN= 0.12 in their computational work for both isothermal and reactive flows. Two isothermal models, one comprising a single equivalent jet flow and another compound jet flow, have been studied. They reported that in a compound jet flow the eddy size is nearly the same irrespective of swirl number. On the other hand, a large variation of the vortex size has been found in a single jet system and reactive system with the swirl number variation. In order to study the flame stability for a non premixed flame, De et al. [14] have done a computational work along with experimentation by supplying the air-fuel mixture through a swirler. They reported that the vortex has been formed at the core along with a corner recirculation zone near the wall both in cold flow simulation and reactive flow simulation. Moreover it has been found that the flame becomes stretched along the axis for reactive flow. Feikema et al. [15] conducted an experiment on gas turbine combustor to study the flame blowout limits by using swirler. They found that a central recirculation vortex reduced the flame velocity that stabilizes the flame. In addition to that an overall lean mixture can be used with the addition of the swirler. Fureby et al. [16] did experimentation as well as a numerical analysis of reactive and non-reactive flow through a gas turbine combustor. They found that the non-reacting case is dominated by an annular swirling jet with the formation of a central toroidal recirculation zone, where as in the reacting case the CRZ remains and dominates the flow in the upstream section of the combustor including the flame and the resulting wall jets.

The flow inside the gas turbine is generally turbulent in nature due to the high velocity air inflow. Many computational models are used to predict the accurate velocity and pressure variations inside the flow field. To simulate the turbulent quantities in a model combustor, LES [17,18, 14, 19] and DNS [20, 21] have been used by different researchers, but all these models suffer from the limitation of very large computational time. Two equation k-ε models along with Favre averaged Navier-Stokes equations are popularly used to simulate the flow in the combustors [22,23,24].

Guo et al. [25] applied different turbulent models such as standard k-ε model, RNG k-ε model, low Reynolds number k-ε model and the differential Reynolds stress model to a submerged jet. They strongly recommended the k-ε models due to their consistency to predict the results during oscillation because the rate of vortices dissipation are slower with k-ε models. However German and Mahmud [26] compared k-ε turbulence model with RST model by using inlet air through a swirler for both reactive and isothermal flow. For Isothermal flow it is observed that the length of centre toroidal recirculation zone become stretched when simulated with k-ε model, where as RST model gives shorter recirculation zone, which is validated fairly with experimentation. Zhu and Shih [27] predicted the flow of a confined jet in a cylindrical duct and found that RNG k-ε model predicts fairly similar results as the standard k-ε model, while a realizable Reynolds stress algebraic equation model perform significantly better in resolving the essential flow features captured in the experiments. On the other hand, Karagoz and Kaya [28] computed turbulent swirling flow in a cyclone using RNG k-ε model and found the results to be in agreement with the experimental data.

Xia et al. [29], have done experiments as well as computational work in a system with strong inlet swirl and used water as the fluid. They used swirl number up to 1.6. By comparing the standard k-ε model, the RNG k-ε model and a differential Reynolds stress model (DRSM), they concluded that, prediction of CRZ, CTRZ and mean velocity profile is better by DRSM, but the prediction of other parameters is less satisfactory near the inlet and central region. The two eddy viscosity models somewhat give good results for radial velocity but they over predict the turbulent intensity.

Escue et al. [30], have experimentally measured and compared various parameters with the results determined by RNG k-ε model and Reynolds stress model. They studied that both the turbulence models yielded an unrealistic decay of the turbulence quantities immediately downstream of the simulation inlet. For lower swirl number (SN), i.e. SN≤1, RNG k-ε model predicts better. If SN≥2 neither of them predicts good result. Yajun et al. [31] compared five different two equation turbulence models for the simulation of flow in a gas turbine combustor and found the realizable k-ε model to perform the best.

All the above works show a wide disagreement in the assessment of predicted results using various k-ε models for computing the turbulent swirling flow. Karim et al. [32] found that the standard k-ε model is often over-diffusive in predicting highly swirling flow and recommended the use of realizable k-ε model instead. Joung and Huh [33] and Zeiniband Bazdidi-Tehrani [34] used realizable k-ε model in the combustor applications and got satisfactory results for the gas phase flow.

1.2.2 Spray break up from pressure swirl atomizer

The atomization process is one of the important subjects to study in which the fuel is converted into fine droplets. The fluid properties like viscosity, density and surface tension play important role in atomization. Also the velocity of fuel, size of the injector hole and orientation of the fuel path from the injector determine the quality of the droplet sizes and penetration of droplets. Surface tension has a tendency to convert the liquid to sphere, which are travelling through a gas medium. But the viscosity has the adverse tendency to form the droplets. However the surrounding gas exerts an aerodynamic force that acts on the droplet surface.

A lot of literature is available on the modelling of liquid sheet but the most significant contribution towards the modelling of hollow cone spray has been attempted by Dorfner et al. [35]. They studied the effects of surface tension and viscosity on liquid spray characteristics and concluded that the mean droplet size increases with the increase in surface tension and viscosity. Han et al. [36] proposed a new model on sheet break up and droplet formation for hollow cone injection by the pressure swirl atomizer for GDI engine. They used Rosin-Rammler distribution for droplet class distribution and found a good agreement for droplet size distribution and

spray penetration with experimentation. The Linearized Instability Sheet Atomization (LISA) model, proposed by Schimdt et al. [37], has been used by many researchers to simulate the droplet formation. In this model, the film formation is followed by sheet break up and atomization. Here the physical concepts are utilized to determine the important spray parameters along with a limited number of empirical constants to evaluate the injection velocity. Senecal et al. [38] studied the primary break up of a liquid spray and have given a linear stability analysis of the planar sheet (neglecting the curvature effect for thin sheets) considering the effect of continuous phase along with the effect of viscosity and surface tension of droplet phase on wave growth. They considered sinuous wave due to its predominant nature over varicose wave for low jet velocity as well as low gas to liquid density ratio. Finally the highest unstable growth rates, sheet break up length and droplet size have been determined by using the developed dispersion relation. The predictions were found to be satisfactory when compared with experimentation. Xue [39] developed a two dimensional axisymmetric computational model to simulate the spray characteristics of pressure swirl atomizers. The model is validated well enough for large scale prototype whereas for small scale prototype semi- empirical correlations are used. Many researchers worked on primary as well as secondary break up models and developed different hybrid models to predict the spray characteristics of hollow-cone nozzle.

Shim et al. [40] developed a hybrid spray model by taking LISA model for primary break up along with APTAB (Aerodynamically Progressed Taylor Analogy Breakup) model for secondary break up. Rosin-Rammler distribution for droplet class distribution has been considered for primary breakup. They suggested their model for high pressure region injection like GDI engine. Bafekar et al. [41] studied the spray characteristics of iso-octane through a pressure swirl injector exposed to a static gas medium. LISA model for primary break up and Taylor Analogy Breakup (TAB) model for secondary break up has been used. Rosin-Rammler distribution has been adopted for droplet distribution. They found that the model predicted good agreement with experiments for spray penetration, spray structure and drop size distribution. Lee et al. [42] proposed six hybrid models by using LISA and WAVE as primary break up models and DDB (Dynamic Drop Breakup), TAB and RT(Rayleigh-Taylor)as secondary break up models. They revealed that, all the models predict satisfactorily

for spray penetrations with experiments but accuracy for SMD hugely differs from each other.

Throughout the last decade many studies on spray break up behaviour, droplet size and their distribution through either a confined or flow gas medium has been done by various people. Different types of injectors such as solid cone injector, effervescent injector and pressure swirl atomizers are used to convert the fuel into fine droplets. Especially pressure swirl atomizer is preferred in gas turbine combustor due to its better atomization, wide spray cone angle and low penetration [43, 44, 45].

Zeoli and Gu [46] developed a numerical model to simulate the breakup of liquid metal during secondary atomization. The momentum and energy exchanges between droplet and continuous phase have been simulated as well. They found that the break up process starts immediately as the liquid metal is exposed to the gas phase and the size of drops become smaller and smaller up to a certain size. The heat energy transfer rate from the droplet to the gas phase become faster as the droplets become finer. Tratnig and Brenn [47] used Dombrowski and Johns model to predict the disturbance wavelength (ω), sheet break up length and gas Weber number. Finally a relationship between the global Sauter mean drop size and the global drop size RMS is established. Also a method is developed for predicting the global drop size spectra in the sprays.

1.2.3 Modelling of Combustion process

Combustion processes may be categorized into different types. According to the flow velocity it may be laminar or turbulent combustion. In a laminar flow combustion system, the molecular diffusion in between fuel and reactant molecules has been occurred where as in turbulent flame, turbulent mixing is predominant over molecular diffusion. To simulate the turbulent combustion process, many computational models has been developed and adopted by different researchers.

Eddy break up model by Spalding [48] was a pioneering and one of the early contributions towards the field of turbulent combustion. In this model the chemical reaction rate has been obtained through an explored relation with the large eddy mixing scale (k/ε) or on the rate of eddy break up. Magnussen and Hjertager [49] followed Spalding and established two semi empirical relations to evaluate the

reaction rate (Eddy dissipation model). One of them calculates the reaction rate following chemical kinetics while the other calculates it as mixing controlled phenomenon. The mixing controlled reaction rate is considered to be governed by the large eddy mixing scale (k/ε). The smaller value out of two reaction rate has been considered as the actual rate of reaction.

Khalid et al. [50] used Eddy dissipation model to study the effects of turbulence level on soot and NOx formation. They validated the predicted temperature along the axis and variation of temperature along the radial direction with the results of Brookes and Moss [98]. However the radial variations depicted some deviation from the experimental results. Gassoumi et al. [51] also used Eddy dissipation combustion model to study the effect of swirl in a co-axial combustor. From their validation it has been found that near the inlet, the radial distribution of temperature deviates more from the experimental data whereas at downstream the agreement is very good with the experiments. The same combustion model has been used by Kamnis and Gu [52] to simulate the combustion of propane with pure oxygen. The authors compared the maximum flame temperature within the combustion chamber with the adiabatic flame temperature of propane and established a good agreement with the experimental results.

However both of the above models suffer the limitation of using the global reaction mechanism in calculating the rate of reaction. Consequently a combustion model (Eddy dissipation concept) has been developed by Magnussen [53] to treat the multi step reactions in a turbulent combustion process. Further, this model [54] was extended to include the chemical kinetics of reaction with many assumptions. This model can be used for either premixed or diffusion flame. This model is being popularly used by many researchers to study the turbulent combustion characteristics [55,56,57]. But the computational economy of the model is relatively poor as it involves the solution of a large number of species transport equations including all of the intermediate species.

An elegant computational procedure to simulate the diffusion flame has been developed by Spalding [58] (Simple chemical reacting system). But the method was limited to assumptions that the chemical reactions had to be single step and infinitely fast occurring with the stoichiometric proportion of fuel and oxidiser. Instead of Reynolds averaging of the governing equations a density weighted averaging method

has been suggested by Favre [59] to incorporate the turbulent effect in a flow system. By this method many extra terms from the governing equations has been eliminated and almost all the transport equations became similar in appearance. Therefore a single scalar variable may represent all other scalar variables.

A generalized state-relationship correlations that gives the mass fractions of major gas species and temperature as functions of local fuel-equivalence ratios (mixture fraction) were studied for hydrocarbon-air diffusion flames by Sivathanu and Faeth [60]. The Favre averaged mixture fraction called mean mixture fraction is used as a key scalar variable that represent all other scalar variables.

However to evaluate the mean value of the scalar variables, which are the functions of mean mixture fraction, a probability density function is used. Pope [61], Chen et al. [62] have given the early contribution towards this study. The PDF(Probability Density Function) technique is a very powerful tool in order to study the reactive or non-reactive turbulent flows. In addition to that by this method the reacted source term has been treated without any assumption of turbulent fluctuations [63,64,65,66]. The mathematical description of PDF has been clearly described in detail in [67].

The concept of flamelet was introduced by Williams [68] considering that a diffusion flame can be represented by an ensemble of laminar opposed flames with one stream of oxidant and another stream of fuel. The work considered the rate of chemical reaction to be much faster than the rates of transport. The model was extended by Peters [69] by incorporating the detailed chemistry considering finite rate of reaction. High turbulence level in the combustor causes straining of the flames, resulting departure from the equilibrium. The non-equilibrium effects have been accounted by decoupling the chemistry calculation from the flow calculation. Many vital contributions towards the development of flamelet method have been found in [70,71].

Li et al. [72] investigated in a bluff-body stabilized non-premixed jet flame to show that the prediction using the equilibrium chemistry model fails near the fuel jet and results into under-prediction of temperature. Under such a situation, the species concentration and temperature distributions across an individual flamelet can be uniquely described by mixture fraction and strain rate (or scalar dissipation rate) as observed in a laminar flame considering detailed chemical reaction mechanism [73].

Furthermore, in the flamelet model, the effect of turbulence can be accounted statistically through a presumed probability distribution function. Fallot et al. [74] studied the effect of finite rate chemistry in a non premixed turbulent combustion through a bluff-body stabilized flame. Seunghwan et al. [75] also used laminar flamelet model to study the spray combustion inside a DI engine. Baba and Kurose [76] established the validity of a flamelet modelling on spray combustion. However, some of the researchers also used an equilibrium model with a constrained condition to overcome the limitation of the equilibrium chemistry model [77,78].

1.2.4 Soot in flame

Soot formation in combustion of hydrocarbon fuels is another complex phenomenon which needs to be addressed. Soot is formed during the combustion of hydrocarbon fuel at rich mixture condition at high temperature. Soot formation starts with the precursor species such as acetylene (C_2H_2), benzene (C_6H_6) and phenyl radical (C_6H_5), in the rich side of the flame zone. Consequently, the nucleated precursors grow to become polycyclic aromatic hydrocarbons known as soot [79,80].

A lot of works both using experimental and/or theoretical approach have been reported on soot in flames. Comprehensive reviews on soot formation have been given by Haynes and Wagner [81], Glassman [82], Frenklach [83] and Mansurov [84]. Soot models can be broadly divided into three groups- empirical, semi empirical and detailed model. All three types of models have been discussed by Kennedy [85] for different fuels.

Probably the earliest contribution towards the modelling of soot was provided by Calcote and Manos [86]. In their model they used a direct relation that predicts the soot with respect to the local equivalence ratio called threshold sooting index. This is a quick method and consumes less computation memory. Khan and Greeves [87] proposed a one step soot model based on empirical soot formation rate for diesel fuel. They, for the first time, considered the soot particle inception during combustion and expressed it as the function of temperature, pressure and equivalence ratio. Both of the above models are based on number of assumed constants, therefore are purely empirical models. Tesner et al. [88] developed a two equation soot model that

includes some assumptive constants and predicts the nucleation rate. Consequently, soot was evaluated by solving the production and consumption of soot nuclei.

However, these early models are limited to predict the final soot concentration without going into the actual physical and chemical processes that actually happen. Nowadays, detailed chemical kinetics is generally used to study the combustion phenomenon. Therefore in order to understand the effects of the chemical and physical processes on soot formation, different semi empirical as well as detailed soot models have been developed by various researchers incorporating detail chemistry.

From the review of literature it has been found that many researchers such as Young et al. [89], Kollmann et al. [90], Kronenburg et al. [91], Bai et al. [92] focused on the use of semi empirical soot model along with PDF and flamelet based combustion model by incorporating the detailed chemistry. In the last couple of decades many semi-empirical soot models have been developed by Kennedy et al. [93], Coelho and Carvalho [94], Moss et al. [95], Kumar et al. [96], Christopher et al. [97]. However most of the works on modelling of soot is done for lower hydrocarbon fuels. Kronenburg [91], Brookes and Moss [98], Sivathanu and Gore [99], Kaplan et al. [100], Mandal et al. [101], Smooke et al. [102] made significant contributions towards the modelling of soot formation for methane fuel. A few works towards predicting soot in kerosene fuel combustion have been found in the literature. Moss and Aksit [103] used a semi empirical soot model in order to predict the soot in a laminar diffusion flame by using a surrogate kerosene fuel by modifying the model constants. Whereas, Wen et al. [104] and Watanabe et al. [105] devoted their contributions towards the modelling of soot for the diffusion flame of surrogate kerosene fuel.

Some researchers developed detailed model of soot formation by considering the precursors from chemical kinetics. Christopher et al. [106] developed a simple soot model for ethylene, propylene and propane flames. Wang et al. [107] developed a soot model for n-heptane, n-butanol and diesel. Massimiliano et al. [108] developed a detailed soot model for gas turbine combustor by using the fuels ranging from surrogate kerosene to methane with a single set of constants and they tested it with different operating condition. However from the literature it has been revealed that it does need further research to predict the soot concentration with more accuracy for heavier hydrocarbon fuels.

1.2.5 Role of Soot in radiation

Soot behaves like a black body in radiative heat transfer. Therefore the soot in flame radiates significant thermal energy and as a consequence flame temperature is reduced and the temperature of periphery such as combustor wall of gas turbine combustor increases. Many computational models have been developed and employed by researchers to predict the surface radiation. However, radiation inside the combustor is a volumetric phenomenon and the products such as carbon dioxide and water vapour also participates in radiative exchanges along with soot. P1 model [109] and DO (Discrete ordinate) [110, 111] models are the most frequently used radiation models in combustible flow due to their capability to simulate the volumetric radiation along with the interaction of particulates in radiative heat transfer [117]. Monte Carlo method (MCM) [112, 113] also has been used by various researchers to predict the radiative heat transfer in combustible flow. However, MCM requires much longer computational times as compared to DO model, though its accuracy is better [114, 115]. A finite volume approach of radiation model (DO) was first introduced by Chandrashekhar [116]. This model predicts better for the case of higher optical thickness [117]. Many authors considered the effect of soot on radiation to study the temperature field inside the combustor [118, 119, 120, 121] by using different radiation models. DO radiation model along with the incorporation of soot effect has been successfully used by [119, 121,122].

1.3 Present contribution

The major contributions of the present work are

- The selection of a turbulent model for mild swirling flow in combustor has been done verifying different two equation k-ε models carefully along with their technical details.
- A comparison among three combustion models, such as Eddy dissipation model, Laminar flamelet model and Constrained equilibrium model, has been done along with discussing their methods of calcution for various thermo physical parameters.

- In order to solve the liquid fuel spray combustion problem, LISA spray atomization model in Eulerian-Lagrangian frame has been included.
- A semi-empirical soot model for kerosene fuel combustion with optimized model parameters has been proposed. DO radiation model is used to simulate the radiation effect inside the combustor.
- Effect of air flow distribution on soot and radiative heat transfer has been studied in a 3-D model combustor.
- Effect of swirl on soot and radiative heat transfer has been studied in a 3-D model combustor.

1.4 Outline of the thesis

The work has been described in Chapters 2 to 8. Chapter 2 describes the theoretical formulation followed in the work. In the first part of Chapter 2, Reynolds average governing equations, which are used to simulate the cold flow simulation, are discussed. Then the details of three different two equation k-ε models are carefully elaborated. Consequently the turbulent models are verified by using the experimental data of Rahim et al. [126]. It has been found that for mild swirl at inlet, realizable *k-ε* performs better than the other two k-ε models. Therefore realizable *k-ε* model is used in the following simulations.

In Chapter 3, the governing equations for reactive flow in Reynolds avaraged form and Favre avaraged form are discussed. The dispersed phase model and the atomization model, which are used to simulate the liquid fuel combustion, are also discussed here. The details of three combustion models along with the physical fundamentals and chemistry that has been used to determine the various physical and chemical parameters in side the computational domain are explained. In the last part of the chapter, DO radiation model and numerical methods that have been used in the simulation are studied.

In chapter 4, the physical fundamentals of soot formation, surface growth of soot, coagulation and oxidation are described. The detail of Brookes and Moss soot models along with their governing equations and source terms have been explained. Accetylene is used as the soot precursor and surface growth as well. Fenimore Jones [123] oxidation model is used to oxidation of soot during combustion. Finally, the

soot model is validated against the results produced by Young et al. [142] and Wen et al. [104].

In chapter 5, three different combustion models are compared with the help of an axi-symmetric model by comparing the results obtained from them. The experimental details of our in-house experimental set up of the combustor is explained. The detail physical pictures and the schematic of combustor set up along with fuel control, air control to both primary and secondary inlet, temperature measurement on the combustor wall and exit have been given.

In chapter 6, the combustion process has been simulated by using laminar flamelet model. The effects of mass flow distribution through primary and secondary inlets on temperature distribution and soot distribution have been studied.

In chapter 7, the combustion process has been simulated by using laminar flamelet model and the effects of inlet swirl angle at primary inlet on temperature distribution and soot distribution have been studied.

In chapter 8 , the over all conclusion of the entire work and the scope for future extentions have been discussed.

Chapter 2

Modelling of isothermal turbulent swirling flow using two-equation models

2.1 Introduction

The fluid flow in a combustor is highly turbulent with random fluctuations of the flow variables occurring in the flow. Due to the random fluctuations, the turbulent flow becomes highly diffusive in nature. As a result the mass, momentum and energy transport parameters are enhanced in turbulent flow. Generally, turbulent flow satisfies the same basic conservation equations as the laminar flow. However, turbulent flow is characterized by a wide range of eddies of various length scales. Thus, in order to simulate a turbulent flow, the conservation equations need to be applied in a sufficiently fine grid system, which is capable to capture the smallest length scales. This approach is called Direct Numerical Simulation (DNS). But it needs very fine grid to catch the fluctuating behaviour of the flow parameters and the minimum number of grids required is of the order $Re^{9/4}$ [124]. As a result the computational cost becomes very high. Therefore in order to reduce the computational cost, an approximate treatment of the governing equations is done with the help of a statistical approach called averaging. In this approach, the instantaneous values of all the variables are disintegrated into a mean and a fluctuation and only the transport equations for the mean quantities for all the variables are solved. The approach needs separate models to solve the fluctuating components.

2.2 Conservation equations for isothermal flow simulation using different turbulence models

In order to obtain the average quantities of the flow variables in a cold flow simulation, the continuity and the momentum (Navier-Stokes) equations are averaged across finite time span. Consequently new forms of momentum equations have been derived called Reynolds average Nervier-Stokes (RANS) equations. The forms of RANS equations are same as the Navier-Stokes equations, but the variables in these equations are the average quantities rather than the instantaneous values. Along with that, some new parameters called Reynolds stresses are formed. The formation of Reynolds stresses increases the complexity to solve the momentum equations and it becomes a cumbersome job to solve the equations directly. The governing equations required to simulate the steady isothermal turbulent flow in universal tensor notation have been presented below.

Conservation of mass

$$\frac{\partial}{\partial x_i}(\rho \bar{u}_i) = 0 \tag{2.1}$$

Conservation of momentum

$$\frac{\partial}{\partial x_i}\left(\rho \bar{u}_i \bar{u}_j\right) = -\frac{\partial \bar{p}}{\partial x_i} + \frac{\partial}{\partial x_j}\left(\bar{\tau}_{ij} - \rho \overline{u_i' u_j'}\right) \tag{2.2}$$

where, ρ is the density of the fluid and $\bar{u}_i$ and $\bar{p}$ are the time average mean flow velocity and time average mean pressure. The stress tensor in the momentum equation is expressed as $\bar{\tau}_{ij}\left(= \mu\left(\frac{\partial \bar{u}_i}{\partial x_j} + \frac{\partial \bar{u}_j}{\partial x_i}\right)\right)$. $-\rho \overline{u_i' u_j'}$ is the Reynolds stress and it is an additional term that has been formed due to time averaging.

2.2.1 *k-ε* turbulent models

In order to simulate the Reynolds stresses present in the momentum equation, separate models are required. There are many turbulent models used by different researchers found in the available literature. Still k-ε two equation models are popularly used by various people to simulate the turbulence effect for moderate as well as high Reynolds number flow. These equations also prove their capability to

predict good results for swirling flows. The Reynolds stresses in the momentum equation are expressed as the product of turbulent viscosity (μ_t) and the fluid strain rates in terms of the mean velocities. In order to evaluate Reynolds stresses, the generalised form of Boussinesq approximation equation has been used given as follows,

$$-\rho\overline{u_i' u_j'} = \mu_t\left(\frac{\partial \bar{u}_i}{\partial x_j} + \frac{\partial \bar{u}_j}{\partial x_i}\right) - \frac{2}{3}\rho k \delta_{ij} \tag{2.3}$$

In the two equation k-ε model of turbulence, the turbulent viscosity is expressed in terms of turbulent kinetic energy (k) and its dissipation rate (ε). The two turbulence quantities are evaluated by solving the respective conservation equations. It has been observed from the literature available that there are three different types of k-ε models used to simulate the turbulent flow, such as standard k-ε model, RNG (Renormalizing group) k-ε model and Realizable k-ε model. The major differences among these models are:

1. The methodology behind the calculation of turbulent viscosity

2. The turbulent Prandtl number that governs the eddy diffusion of k and ε

3. The destruction and production of ε in the ε equation.

2.2.1.1 Standard k-ε turbulent model

This is one of the simplest and complete two equation turbulent model developed by Launder and Spalding [125] in which two transport equations are solved to obtain the rate of generation of turbulent kinetic energy (k) and dissipation rate of turbulent kinetic energy (ε), respectively. The assumption for this model is that the flow is fully turbulent (high Reynolds number). In the standard k-ε model, the governing equations for k and ε are expressed as follows:

$$\frac{\partial}{\partial x_i}(\rho k \bar{u}_i) = \frac{\partial}{\partial x_j}\left[\left(\mu + \frac{\mu_t}{\sigma_k}\right)\frac{\partial k}{\partial x_j}\right] + G_k - \rho\varepsilon \tag{2.4}$$

$$\frac{\partial}{\partial x_i}(\rho \varepsilon \bar{u}_i) = \frac{\partial}{\partial x_j}\left[\left(\mu + \frac{\mu_t}{\sigma_\varepsilon}\right)\frac{\partial \varepsilon}{\partial x_j}\right] + C_{1\varepsilon}\frac{\varepsilon}{k}G_k - C_{2\varepsilon}\rho\frac{\varepsilon^2}{k} \tag{2.5}$$

In the above equations, G_k represents the generation of turbulent kinetic energy, which is expressed in terms of the mean velocity values as,

$$G_k = \left(\mu_t \left(\frac{\partial \bar{u}_i}{\partial x_j} + \frac{\partial \bar{u}_j}{\partial x_i} \right) - \frac{2}{3} \rho k \delta_{ij} \right) \frac{\partial \bar{u}_j}{\partial x_i} \quad (2.6)$$

Turbulent viscosity can be obtained from the dimensional analysis as given below

$\mu_t = C \rho v l = C_\mu \rho \frac{k^2}{\varepsilon}$, where C_μ is a model constant and its value is taken as 0.09.

$v = k^{1/2}$, $l = \frac{k^{3/2}}{\varepsilon}$, where v is the velocity scale and l is the length scale

The model constants $C_{1\varepsilon}$, $C_{2\varepsilon}$, σ_k (turbulent Prandtl number for k) and σ_ε (turbulent Prandtl number for ε) in the k and ε equations have default values obtained empirically and given below in the table

Table 2.1 Various constants of standard k-ε turbulent model

C_μ =0.09	σ_ε=1.30	σ_k = 1.00	$C_{1\varepsilon}$ = 1.44	$C_{2\varepsilon}$ = 1.92

2.2.1.2 RNG k-ε turbulent model

Standard k-ε model has been improved with the help of rigorous statistical mechanism. In this model, the destruction of (ε) is not only the function of (ε) and (k) but also a function of constant term used in the destruction component. But that will not remain constant like standard k-ε model. It is a function of shear deformation. Therefore the destruction of (ε) largely varies with Reynolds number variation. However the effect of Reynolds number (for moderate Reynolds number flow) on turbulent Prandtl number and eddy viscosity can be incorporated in the RNG k-ε model. Since we simulate higher Reynolds number flow, the effect of Reynolds number has not been incorporated to evaluate eddy viscosity and turbulent Prandtl number.

The governing equations for RNG k- ε model to evaluate k and ε are expressed as follows:

$$\frac{\partial}{\partial x_i}(\rho k \bar{u}_i) = \frac{\partial}{\partial x_j} \left(\frac{\mu_{eff}}{\sigma_k} \frac{\partial k}{\partial x_j} \right) + G_k - \rho \varepsilon \quad (2.7)$$

$$\frac{\partial}{\partial x_i}(\rho\varepsilon\,\overline{u}_i) = \frac{\partial}{\partial x_j}\left(\frac{\mu_{eff}}{\sigma_\varepsilon}\frac{\partial\varepsilon}{\partial x_j}\right) + C_{1\varepsilon}\frac{\varepsilon}{k}G_k - C^*_{2\varepsilon}\rho\frac{\varepsilon^2}{k} \tag{2.8}$$

In the above equations, G_k represents the generation of turbulent kinetic energy, which is expressed in terms of the mean velocity values as,

$$G_k = \left(\mu_t\left(\frac{\partial\overline{u}_i}{\partial x_j} + \frac{\partial\overline{u}_j}{\partial x_i}\right) - \frac{2}{3}\rho k\delta_{ij}\right)\frac{\partial\overline{u}_j}{\partial x_i} \tag{2.9}$$

σ_k and σ_ε are the effective Prandtl number for k and ε respectively. μ_{eff} ($\mu_{eff} = \mu + \mu_t$) is the effective viscosity. Turbulent viscosity μ_t can be obtained from the relation as given below

$\mu_t = C_\mu\rho\dfrac{k^2}{\varepsilon}$, where C_μ is a model constant.

In ε transport equation $C^*_{2\varepsilon}$ term does not remain constant like standard k-ε model. It is determined as

$$C^*_{2\varepsilon} \equiv C_{2\varepsilon} + \frac{C_\mu\eta^3(1-\eta/\eta_o)}{1+\beta\eta^3} \tag{2.10}$$

Where, $\eta = S\dfrac{k}{\varepsilon}$ and $S = \left(2S_{ij}S_{ij}\right)^{1/2}$

where, S is the shear deformation. In this model, where $\eta < \eta_o$, $C^*_{2\varepsilon}$ will be greater than $C_{2\varepsilon}$ and vice versa. Here $C^*_{2\varepsilon}$ becomes a function of shear deformation. Therefore the destruction of ε largely varies with the Reynolds number variation. At higher Reynolds number flow, the value of $C^*_{2\varepsilon}$ decreases hence destruction of ε reduces. Similarly for lower Reynolds number flow, the effect becomes reverse. The destruction term in ε transport equation mainly differentiates RNG k-ε model from standard k-ε model. The RNG k-ε model predicts better for rapid strained flow.
The model constants are given in the table shown in below

Table 2.2 Various constants of RNG k-ε turbulent model

C_μ =0.0845	σ_k =0.7174	σ_ε =0.7194	$C_{1\varepsilon}$ =1.42	$C_{2\varepsilon}$ =1.68

2.2.1.3 Realizable k-ε turbulent model

Realizable *k-ε* model is the improved version of standard *k-ε* model. Two major modifications in the transport equation of *k* and *ε* have been incorporated to predict the better result of a turbulent flow system. Here the eddy diffusivity term is not only the function of k and ε but the term C_μ also becomes the function of the mean strain, mean rate of rotation and turbulence quantities. However the *ε* transport equation is quite different as compared to RNG *k-ε* model and standard *k-ε* model. The turbulent energy generation term from the *ε* equation has been eliminated. It is believed that the present form better represents the spectral energy transfer. The term C_1 also no longer remains constant, it is also become the function of *k*, *ε* and shear deformation. More over the destruction term in this equation is arranged such a way that, even though *k* term becomes zero, the destruction of *ε* will always be present there. The governing equations for k and ε are given below as;

$$\frac{\partial}{\partial x_i}(\rho k \bar{u}_i) = \frac{\partial}{\partial x_j}\left[\left(\mu + \frac{\mu_t}{\sigma_k}\right)\frac{\partial k}{\partial x_j}\right] + G_k - \rho\varepsilon \tag{2.11}$$

$$\frac{\partial}{\partial x_i}(\rho\varepsilon \bar{u}_i) = \frac{\partial}{\partial x_j}\left[\left(\mu + \frac{\mu_t}{\sigma_\varepsilon}\right)\frac{\partial \varepsilon}{\partial x_j}\right] + \rho C_1 S_\varepsilon - \rho C_2 \frac{\varepsilon^2}{k + \sqrt{\nu\varepsilon}} \tag{2.12}$$

In the above equations, G_k represents the generation of turbulent kinetic energy, which is expressed in terms of the mean velocity values as,

$$G_k = \left(\mu_t\left(\frac{\partial \bar{u}_i}{\partial x_j} + \frac{\partial \bar{u}_j}{\partial x_i}\right) - \frac{2}{3}\rho k \delta_{ij}\right)\frac{\partial \bar{u}_j}{\partial x_i} \tag{2.13}$$

σ_k and σ_ε are the effective Prandtl number for k and e respectively.

$C_1 = \max\left[0.43, \frac{\eta}{\eta + 5}\right]$, $\eta = S\frac{k}{\varepsilon}$, $S = \sqrt{2S_{ij}S_{ij}}$

$\mu_t = C_\mu \rho \frac{k^2}{\varepsilon}$, where C_μ is no longer a constant like standard k-ε model and RNG k-ε model.

$$C_\mu = \frac{1}{A_0 + A_s \frac{kU^*}{\varepsilon}} \tag{2.14}$$

where, $U^{*} \equiv \sqrt{S_{ij} S_{ij} + \tilde{\Omega}_{ij} \tilde{\Omega}_{ij}}$, $\tilde{\Omega}_{ij} = \Omega_{ij} - 2\varepsilon_{ijk}\omega_k$, $\Omega_{ij} = \overline{\Omega}_{ij} - \varepsilon_{ijk}\omega_k$

$\overline{\Omega}_{ij}$ is the mean rate of rotation tensor at an angular velocity ω_k

The model constant $A_0 = 4.04$ and $A_s = \sqrt{6}\cos\phi$

where $\phi = \frac{1}{3}\cos^{-1}\left(\sqrt{6}W\right)$, $W = \frac{S_{ij} S_{jk} S_{ki}}{\overline{S}^3}$, $\overline{S} = \sqrt{S_{ij} S_{ij}}$, $S_{ij} = \frac{1}{2}\left(\frac{\partial u_j}{\partial x_i} + \frac{\partial u_i}{\partial x_j}\right)$

The model constants are given below

Table 2.3 Various constants of Realizable k-ε turbulent model

C_2=1.9	σ_k =1.00	σ_ε =1.20

2.3 Selection of turbulent model for swirling flow

The three different two equation *k*-ε models, as discussed above, have been compared to predict the performance of turbulent swirling flow in different physical situations. In the present study we simulate the swirl flow across a dump diffuser and through the casing-liner annulus over the liner dome in a model combustor to compare the performance of different two equation turbulence models. Three different two-equation models, viz. standard *k*-*ε* model, RNG *k*-*ε* model and realizable *k*-*ε* model, have been used and their predictions have been compared against the experimental results presented by Rahim et al. [126] to choose the most suitable model from the three.

In this work the axial velocity distribution, radial velocity distribution and pressure variation along the radial direction has been compared with measured values at certain distance from the flow inlet. Moreover the radial distribution of axial velocity has also been compared at the annulus region of the dump diffuser. The pressure variation along the diffuser casing wall and the pressure variation along the liner wall also have been compared with the experimental values.

2.3.1 Model description

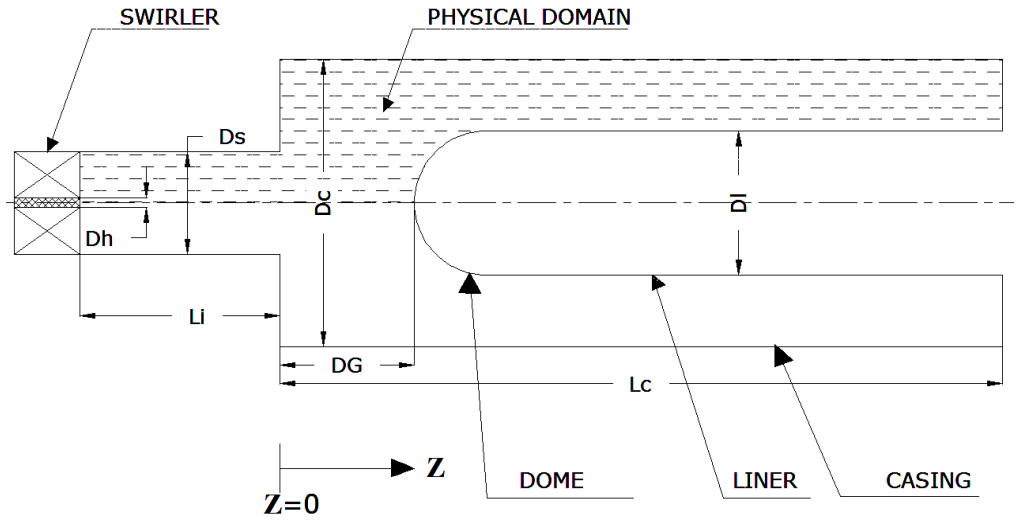

Figure 2.1 Physical model of dump diffuser

Figure 2.1 shows the physical model of the axi-symmetric combustor analyzed in the present work. The geometry and the size of the combustor are identical to those considered by Rahim et. al. [126], with hemispherical dome at the liner head. The length of the inlet pipe (L_i) and that of the casing (L_c) are 0.1m and 0.4572m, respectively. A swirler is considered at the inlet pipe to impart the necessary swirl to the flow simulating the condition of air flow from the compressor. Different vane angles of the swirler have been considered in order to vary the swirl level at the entry to the diffuser. The outer diameter of swirler (D_s), swirler hub diameter (D_h), air casing diameter (D_c) and liner diameter (D_l) are 0.054m, 0.005m, 0.1524m and 0.0762m, respectively. The position of the liner, with respect to the outer casing, can be varied to change the dump gap (L_d). The computational domain for the analysis of flow in the annulus has been marked in the **Figure 2.1**.

2.3.2 Boundary and operating conditions

Due to the elliptic nature of the governing equations, boundary conditions are to be specified at all the boundaries of the computational domain, i.e., the inlet, outlet, axis and wall of the axi-symmetric combustor (**Figure 2.1**), for the three components of the velocity, k and ε. At the inlet plane, the axial velocity has been considered to be uniform (plug flow), while the radial velocity is taken to be zero. The mass flow rate

of air is so chosen that the Reynolds number based on the inlet axial velocity ($U_{z\text{-}in}$) and the diameter of the inlet pipe (D_s) is 1.2×10^5. The local tangential velocity is computed considering constant swirl angle (θ) as

$$U_{\theta-in} = U_{z-in} \tan\theta \tag{2.15}$$

The vane angle and geometry of the swirler have been represented by a non dimensional number called swirl number [127] to present the results. The swirl number is calculated as

$$SN = \frac{2}{3}\frac{\left(D_s^3 - D_h^3\right)}{\left(D_s^2 - D_h^2\right)\left(D_s - D_h\right)}\tan\theta \tag{2.16}$$

The turbulent kinetic energy (k) and its dissipation rate (ε) at the inlet plane are computed from the assumed turbulent intensity and the length scale there. The turbulent intensity (TI) and the length scale (LS) at inlet conditions are set by using the empirical relations as given below [128]

$$TI = \frac{U'}{U_{avg}} = 0.16\left(\mathrm{Re}_{Ds}\right)^{-1/8} \tag{2.17}$$

$$LS = 0.07\, D_s \tag{2.18}$$

At the outlet, the axial gradient of all the variables have been set to zero. No slip boundary condition with the standard law of wall has been considered on the solid walls, while the symmetric boundary condition is set on the axis.

The numerical code in polar co-ordinate for the axi-symmetric geometry is validated by comparing its predictions against the experimental data of Rahim et al. [126] for the same operating conditions. Accordingly, a swirl number (SN) = 0.38, $U_{z|in}$=32.37 m/s, $U_{\theta|in}$=18.68 m/s and a non-dimensional dump gap DG = 1 have been used in the computation. The validation has been made by comparing the velocity and pressure distributions in the inlet pipe before the dump plane, in the diffuser after the dump plane and inside the casing-liner annulus.

2.4 Results and Discussions

2.4.1 Flow properties in the inlet pipe before the dump plane

Figures 2.2 (a), (b) and (c) show the comparisons of measured and predicted radial distributions of axial velocity, tangential velocity and static pressure, respectively, in their non-dimensional forms, at 0.05 m downstream to the inlet plane. The flow parameters predicted by the three different turbulence models, employed in the study, have been plotted in these figures along with the experimental data of Rahim et al. [126].

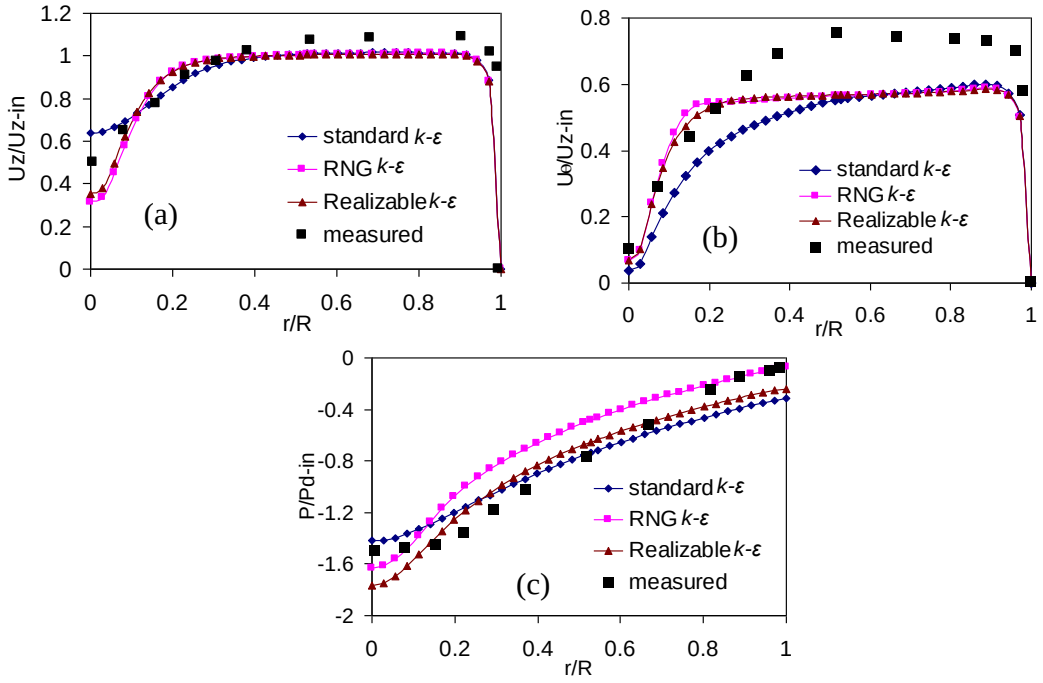

Figure 2.2 comparisons of measured and predicted radial distributions of (a) axial velocity (b) tangential velocity (c) static pressure in their non-dimensional forms, at 0.05 m downstream of the inlet plane.

A qualitative agreement is observed between all the predicted results and the measured values, though some quantitative differences exist among them. **Figure 2.2(a)** shows that the peak axial velocity occurs at an off-axis radial location due to the swirling motion in the flow. The figure further reveals that the axial velocity is somewhat over predicted by the standard k-ε model near the axis while, the other two turbulence models (RNG k-ε model and realizable k-ε model) under predict the axial velocity there. Subsequently, beyond 40% of the pipe radius, all the three models

predict nearly the same axial velocities, which remain within 4.6% of the measured values in [126]. The tangential velocity distributions predicted by the RNG k-ε and realizable k-ε models also show good agreement with the measured data up to 20% of the pipe radius (**Figure 2.2(b)**). However, some quantitative difference has been noticed in the predicted results of all the three models at higher radii. The static pressure distribution (**Figure 2.2(c)**) shows a low pressure region near the axis as a result of the swirling motion in the flow. All the predictive models show pressure variations similar to that of the measured one. The differences in the quantitative data reveal that the realizable k-ε model predicts the pressure with the least variation from the measurement.

2.4.2 Axial velocity distribution inside the casing and annulus

The comparison of the radial distributions of the axial velocities predicted by the numerical models and the measured data at four different axial locations (i.e. Z/D_c=0.1, 0.3, 1.5 and 2.1) following the dump plane have been investigated in **Figures 2.3a-d.** Both the velocity and the distance have been plotted as non-dimensional quantities in the figures. **Figure 2.3(a)** shows the velocity profile at Z/D_c=0.1, which lies between the dump plane and the dome head close to the dump plane. The measured data shows a flow reversal on the axis at this axial location, while a very weak back flow is also reported adjacent to the peripheral wall. Out of the three k-ε models, only the RNG k-ε model has predicted the on-axis back flow at this axial location, while the standard k-ε model prediction shows the maximum deviation in the value. However, all the three models predict very good results near the outer wall of the casing. The peak axial velocity and its corresponding location have also been predicted fairly well by the three models.

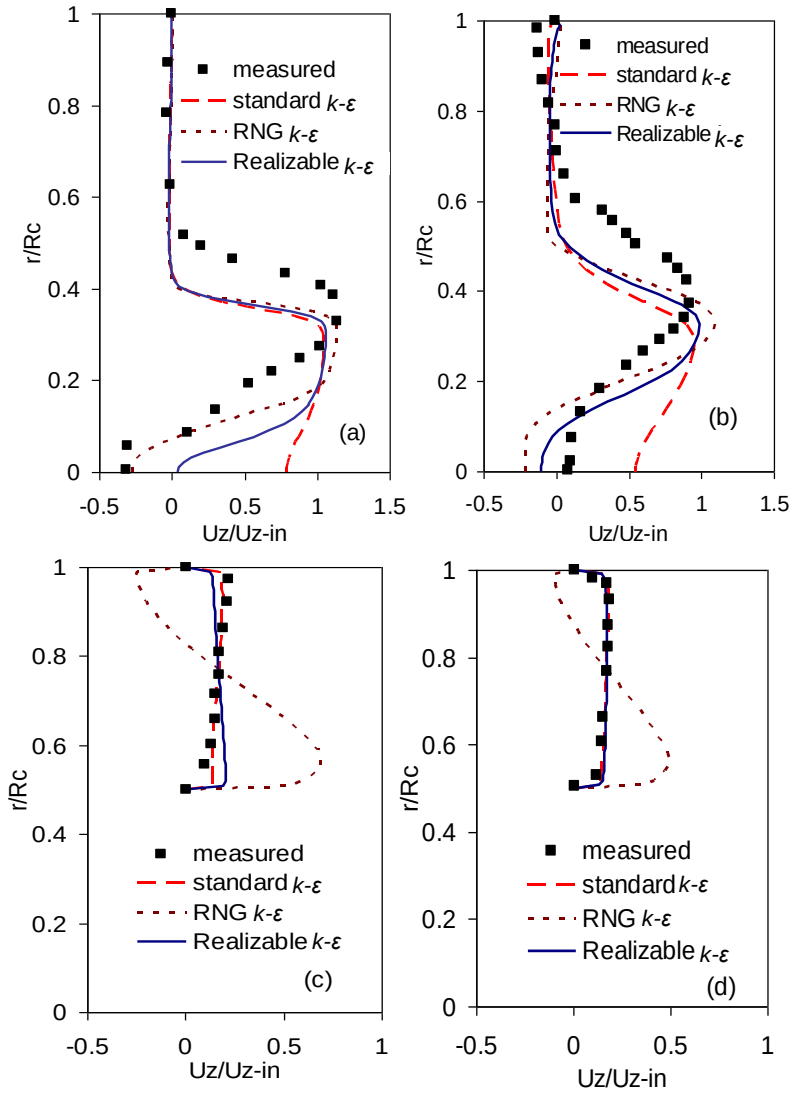

Figure 2.3 Radial variation of Axial Velocity at different axial locations (a) *Z/Dc*=0.1 (b) *Z/Dc*=0.3 (c) *Z/Dc*=1.5 (d) *Z/Dc*=2.1

At *Z/Dc*= 0.3 (shown in **Figure 2.3(b)**), which is near to the dome head, some change in the velocity pattern has been noticed. The measured value shows positive axial velocity on the axis, while the velocity predicted by both RNG and realizable k-ε models are negative there. Standard k-ε model predicts a much higher positive velocity on the axis at this plane as well. Again the peak velocity has been predicted fairly accurately by all the models.

The measured axial velocities at Z/D_c=1.5 and 2.1 (**Figures. 2.3c and 2.3d**) show that the flow tends to become almost uniform as it proceeds along the casing-liner annulus. Considerable differences between the measured velocities and those

predicted by the RNG *k-ε* model have been observed in these two cases inside the annulus. In fact, RNG *k-ε* model even predicts reverse flow near the outer wall in the annulus, which is in complete disagreement with the experimental data. The axial velocity predictions from the standard and realizable *k-ε* models, on the other hand, agree very well with the experimental measurements at these two axial locations.

2.4.3 Casing and Liner wall pressure distributions

Further to the velocities, a comparison is also made between the predicted and measured variations in the wall pressure along the casing and liner walls in **Figures. 2.4a and 2.4b**, respectively. The measured pressure variation shows that starting from the dump plane the pressure first decreases a little along the casing wall and then increases suddenly with a strong adverse pressure gradient. The adverse pressure gradient causes reverse flow in the recirculating vortex following the expansion. After the flow reattaches on the outer casing again the pressure changes only a little till the exit plane is reached. It is observed from **Figure 2.4(a)** that the standard *k-ε* model and the realizable *k-ε* model show trends of pressure variation along the casing wall which give fairly good agreement with the measured values. For these two models the pressure decreased to the minimum value at Z/Dc=0.52, then suddenly increased to the maximum at Z/Dc=1.5 and then drop only a little till the exit. However, the RNG *k-ε* model collapses completely in its pressure prediction and shows an unrealistic pressure variation on the casing wall.

Figure 2.4(b) shows the non dimensional pressure over the dome and liner surface. The predicted value of the pressure is low at the dome centre because of the swirl induced recirculation on the centreline close to the dome head. The predicted pressure first increases to reach the maximum and then falls down to a low value before increasing again more gradually and becoming almost uniform. The experimental data lacks sufficient resolution to describe the pressure variation on the dome surface probably due to insufficient measurement locations there. However, comparing the results it is observed that the standard k-ε model and the realizable k-ε model show similar trends of pressure, which are close to the measured values over most part of the liner wall.

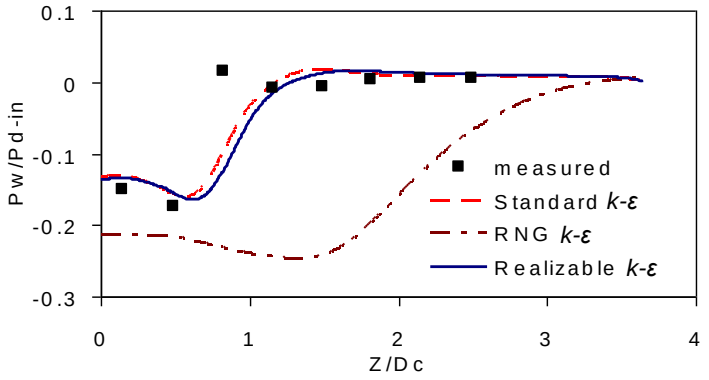

(a)

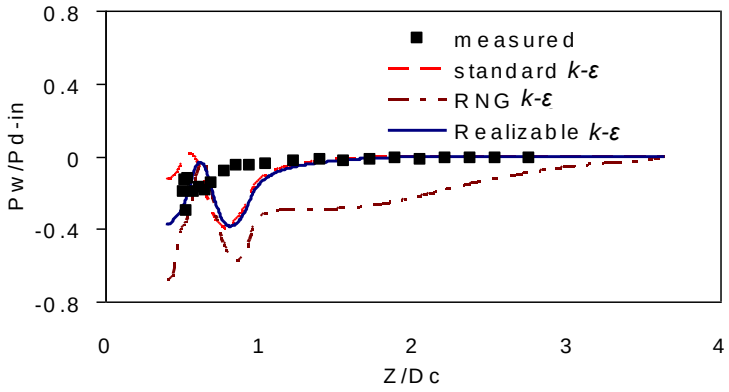

(b)

Figure 2.4 Predicted and measured variations in the (a) wall pressure along the casing and (b) liner walls

2.5 Conclusion

It is detected from the predictions of the three models that the standard *k-ε* model performs poorly in predicting the flow in the inlet pipe after the swirler. The reverse flow observed there in the experimental measurements could not be reproduced by the standard *k-ε* model. On the other hand, the RNG *k-ε* model fails completely in predicting the flow velocity and pressure distribution inside the annulus region between the casing and the liner. Realizable *k-ε* model, on the other hand, performs reasonably well over the entire domain of interest in predicting the flow velocity and pressure distribution. Therefore, the realizable *k-ε* model has been chosen to comprehend the variation in the flow characteristics under varying operating conditions.

Chapter 3

Modeling of Liquid Fuel Spray Combustion in a Swirl Combustor

3.1 Gas phase conservation equations for reacting flow

Most of the turbulent flow and heat transfer problems found in literature are solved by averaging the fluctuating variables in a transport equation through a time averaging method. In this approach, all the fluctuating quantities are averaged across a finite time span, except density. Density is considered as a constant term in RANS equations, because it has been observed that small density fluctuations, that is up to 5% of the mean velocity, do not affect the flow variables much even if the Mach number is around 3 to 5 [129]. But if the velocity fluctuation becomes greater than 20% of the mean velocity, the density fluctuations affect the flow variables at Mach number 1 or even less. In combustion system even though the Mach number is subsonic for the entire flow field, a wide range of density fluctuation will be there due to the local heating during combustion. Therefore the density fluctuations also have to be considered and it is required to average this term. In time averaging method, many additional terms are formed in all the transport equations when we consider density as a fluctuating variable. It enhances the complexity in solving the equations through numerical methods. In order to eliminate the extra terms a density averaging method has been adapted to average all the transport equation. This technique of averaging is known as Favre averaging and the equations are called Favre averaged equations.

3.1.1 Favre-averaged conservation equations in gas phase

It is well known that the instantaneous value of a variable in a turbulent flow field is decomposed into mean and fluctuating terms and it is expressed as;

$$\phi = \bar{\phi} + \phi' \tag{3.1}$$

where, $\bar{\phi}$ is the time averaged mean and ϕ' is the fluctuating component. The density weighted averaging of variables (Favre average) is defined as

$$\tilde{\phi} = \frac{\overline{\rho\phi}}{\bar{\rho}} \tag{3.2}$$

The Favre decomposition form of a flow variable has been written as

$$\phi = \tilde{\phi} + \phi'' \tag{3.3}$$

The Favre averaged governing equations are given as;

Conservation of overall mass (Continuity)

$$\frac{\partial}{\partial x_i}(\bar{\rho}\tilde{u}_i) = 0 \tag{3.4}$$

Conservation of momentum

$$\frac{\partial}{\partial x_i}\left(\bar{\rho}\tilde{u}_i\tilde{u}_j\right) = -\frac{\partial \bar{p}}{\partial x_i} + \frac{\partial}{\partial x_i}\left(\bar{\tau}_{ij} - \bar{\rho}\,\widetilde{u_i'' u_j''}\right) \tag{3.5}$$

Conservation of general scalar variable

$$\frac{\partial}{\partial x_i}\left(\bar{\rho}\tilde{u}_j\tilde{\phi}\right) = \frac{\partial}{\partial x_i}\left(\Gamma_{\phi,lam}\frac{\partial \tilde{\phi}}{\partial x_i} - \bar{\rho}\,\widetilde{\phi'' u_i''}\right) + \bar{S}_\phi \tag{3.6}$$

Conservation of energy

$$\frac{\partial}{\partial x_i}\left(\bar{\rho}\tilde{u}_j\tilde{h}\right) = \frac{\partial}{\partial x_i}\left(\frac{\mu}{\sigma}\frac{\partial \tilde{h}}{\partial x_i} - \bar{\rho}\,\widetilde{h'' u_i''}\right) + S_{rad} + S_E \tag{3.7}$$

Conservation of species mass

$$\frac{\partial}{\partial x_i}\left(\bar{\rho}\tilde{u}_j\tilde{Y}_k\right) = \frac{\partial}{\partial x_i}\left(\frac{\mu}{Sc}\frac{\partial \tilde{Y}_k}{\partial x_i} - \bar{\rho}\,\widetilde{Y_k'' u_i''}\right) + \dot{\omega}_k \tag{3.8}$$

It can be observed that few new terms have appeared through the averaging process. These new terms are $-\bar{\rho}\,\widetilde{u_i'' u_j''}$, called Reynolds stresses or turbulent stresses (this is similar in form described in section 2.2, but that was obtained through

time averaging method). However the Favre averaged form of Boussinesq approximation equation is almost similar to the time averaged form of this equation. But here density is not considered as a constant term. The generalised form of Favre averaged Boussinesq approximation equation to determine the Reynolds stresses has been given as follows,

$$\tau_{ij} = -\overline{\rho}\,\widetilde{u_i'' u_j''} = \mu_t\left(\frac{\partial \tilde{u}_i}{\partial x_j} + \frac{\partial \tilde{u}_j}{\partial x_i}\right) - \frac{2}{3}\overline{\rho}\tilde{k}\,\delta_{ij} \tag{3.9}$$

Here i and j represents the directional vector for x and y respectively. δ_{ij} is the Kronecker delta. δ_{ij} =1 if $i = j$ and δ_{ij} =0 if $i \neq j$. μ_t is the turbulent viscosity (eddy viscosity).

Moreover the new terms $-\overline{\rho}\,\widetilde{h'' u_i''}$, $-\overline{\rho}\,\widetilde{Y_k'' u_i''}$ and $-\overline{\rho}\,\widetilde{\phi'' u_i''}$ are also formed during the time averaging of energy and general scalar variable equation. These are known as turbulent fluxes. However these terms are also unknown quantities and required to be approximated. The turbulent fluxes for enthalpy, species and general scalar variable can be expressed as per Boussinesq approximations are $-\overline{\rho}\,\widetilde{h'' u_j''} = \left(\frac{\mu_t}{\sigma_{ht}}\frac{\partial \tilde{h}}{\partial x_i}\right)$, $-\overline{\rho}\,\widetilde{Y_k'' u_i''} = \left(\frac{\mu_t}{Sc_t}\frac{\partial \tilde{Y}}{\partial x_i}\right)$ and $-\overline{\rho}\,\widetilde{\phi'' u''}_j = \left(\Gamma_{\phi,turb}\frac{\partial \tilde{\phi}}{\partial x_i}\right)$ respectively where, μ_t is the turbulent viscosity, σ_{ht} is the turbulent Prandtl number and Sc_t is the turbulent Schmidt number. $\Gamma_{\phi,turb}$ is the turbulent diffusivity of scalar variable ϕ .

Favre averaged species transport equation is used to simulate the species distribution during the simulation of Eddy dissipation combustion model. However it is not required in the flamelet combustion models, since species are the function of a variable called (discussed in chapter 3.4.2) mean mixture fraction and by using a special treatment for species distribution has been calculated.

Favre averaged form of Realizable k-ε model

The governing equations of k and ε in Favre averaged form are

$$\frac{\partial}{\partial x_i}\left(\bar{\rho}\tilde{k}\tilde{u}_i\right)=\frac{\partial}{\partial x_j}\left[\left(\mu+\frac{\mu_t}{\sigma_k}\right)\frac{\partial \tilde{k}}{\partial x_j}\right]+\tilde{G}_k-\bar{\rho}\tilde{\varepsilon} \tag{3.10}$$

$$\frac{\partial}{\partial x_i}\left(\bar{\rho}\tilde{\varepsilon}\tilde{u}_i\right)=\frac{\partial}{\partial x_j}\left[\left(\mu+\frac{\mu_t}{\sigma_\varepsilon}\right)\frac{\partial \tilde{\varepsilon}}{\partial x_j}\right]+\rho C_1 S_\varepsilon-\rho C_2\frac{\tilde{\varepsilon}^2}{\tilde{k}+\sqrt{\nu\tilde{\varepsilon}}} \tag{3.11}$$

In the above equations, G_k represents the generation of turbulent kinetic energy, which is expressed in terms of the mean velocity values as,

$$\tilde{G}_k=\left(\mu_t\left(\frac{\partial \tilde{u}_i}{\partial x_j}+\frac{\partial \tilde{u}_j}{\partial x_i}\right)-\frac{2}{3}\bar{\rho}\tilde{k}\delta_{ij}\right)\frac{\partial \tilde{u}_j}{\partial x_i} \tag{3.12}$$

σ_k and σ_ε are the effective Prandtl number for k and ε respectively.

$$C_1=\max\left[0.43,\frac{\eta}{\eta+5}\right],\ \eta=S\frac{\tilde{k}}{\tilde{\varepsilon}},\ S=\sqrt{2S_{ij}S_{ij}}$$

$\mu_t=C_\mu\bar{\rho}\frac{\tilde{k}^2}{\tilde{\varepsilon}}$, where C_μ is no longer a constant like standard k- ε model and RNG k-ε model.

$$C_\mu=\frac{1}{A_0+A_s\frac{kU^*}{\tilde{\varepsilon}}} \tag{3.13}$$

Where, $U^*\equiv\sqrt{S_{ij}S_{ij}+\tilde{\Omega}_{ij}\tilde{\Omega}_{ij}}$, $\tilde{\Omega}_{ij}=\Omega_{ij}-2\varepsilon_{ijk}\omega_k$, $\Omega_{ij}=\bar{\Omega}_{ij}-\varepsilon_{ijk}\omega_k$

Where $\bar{\Omega}_{ij}$ is the mean rate of rotation tensor at an angular velocity ω_k

The model constant $A_0=4.04$ and $A_s=\sqrt{6}\cos\phi$

Where $\phi=\frac{1}{3}\cos^{-1}\left(\sqrt{6}W\right)$, $W=\frac{S_{ij}S_{jk}S_{ki}}{\bar{S}^3}$, $\bar{S}=\sqrt{S_{ij}S_{ij}}$, $S_{ij}=\frac{1}{2}\left(\frac{\partial \tilde{u}_j}{\partial x_i}+\frac{\partial \tilde{u}_i}{\partial x_j}\right)$

The model constants are given in table 2.3

3.2 Spray atomization model

Different types of atomizers are used to convert the liquid into fine droplets in engineering applications. Pressure swirl atomizer is one of the atomizers that has been referred by the gas turbine community to atomize the fuel in gas turbine combustor.

In this atomizer, two helical slots are presents on the way of fuel coming out from the injector. The slots provide a helical motion to the fuel. Consequently the fuel coming out from the nozzle converted into a planner sheet and an air core has been formed at the central portion of the injection. The transition from the internal hydrodynamics within the atomizer to the fully developed spray occurs in three steps: sheet formation at the atomizer exit, sheet break up and atomization. These steps have been modelled using the linearized instability sheet atomization (LISA) model [37], considering primary atomization following break up to form the spray. Secondary atomization, coalescence and collision of the droplets in the spray have been neglected. However the advantages of this injector are: it has less penetration of droplet particles and higher cone angle that keep the flame length shorter.

The liquid fuel is injected into the combustor through a pressure swirl atomizer fitted at the centre of the swirler. The mass flow rate of the liquid ($\dot{m}_f$), injector orifice diameter (d_{or}), injection pressure differential (Δp_{inj}) and spray cone angle (2θ) have been given as input to the model. These quantities are obtained from experiments performed in a separate test rig for spray with a pressure swirl atomizer.

In the model, the injection velocity of the liquid at the atomizer exit is calculated using the injection pressure differential and the coefficient of discharge (C_d) of the nozzle in use as,

$$U_{inj} = C_d \sqrt{\frac{2\,\Delta p_{inj}}{\rho_f}} \tag{3.14}$$

A mass balance of the liquid fuel at the atomizer exit evaluates the thickness of the liquid sheet (t) emanating from the nozzle as,

$$\dot{m}_f = \pi \rho_f \left(U_{inj} \cos\theta\right) t \left(d_{or} - t\right) \tag{3.15}$$

From the knowledge of the liquid sheet thickness and sheet velocity, the breakup of the liquid sheet leading to the formation of droplets is modelled. The liquid sheet first breaks up into ligaments as a result of growth of the instabilities developing on the liquid surface. The ligaments, in turn, further break up into drops. The linear stability analysis of Senecal et al. [38] is used for investigating the instability of the liquid sheet. Since the liquid sheet thickness is much smaller than the mean radius of

the sheet, for the purpose of stability analysis, the curvature of the liquid sheet is neglected and the results for planar liquid sheet moving with a prescribed velocity U_{inj} in a stationary gas phase is used. The sinuous mode of instability dominates over the varicose mode at low velocities and low gas-to-liquid density ratios while the two modes become indistinguishable at large velocities. Hence instability of only sinuous mode is used for the instability analysis. Following Senecal et al. [38], the dispersion relation is given by

$$\omega_r = -\frac{2\nu_l k_w^2 \tanh\left(k_w \frac{t}{2}\right)}{\tanh\left(k_w \frac{t}{2}\right) + Q} + \frac{\sqrt{4\nu_l^2 k_w^4 \tanh^2\left(k_w \frac{t}{2}\right) - Q^2 U^2 k_w^2 - \left[\tanh\left(k_w \frac{t}{2}\right) + Q\right]\left(-QU^2 k_w^2 + \sigma k_w^3/\rho_l\right)}}{\tanh\left(k_w \frac{t}{2}\right) + Q} \quad (3.16)$$

In deriving the above equation, second order terms in viscosity have been neglected as they are very small in value. For Weber number $We_g > \frac{27}{16}$, a condition satisfied by most modern pressure-swirl atomizers, the most unstable waves are short waves. For short waves, the ligament diameter is assumed to be proportional to the most unstable wavelength that breaks up the sheet. Thus the ligament diameter is given by

$$d_L = \frac{2\pi C_L}{k_{w_{crit}}} \quad (3.17)$$

In the above equation, k_{wcrit} is the most unstable wave number giving the highest growth rate as obtained from the dispersion relation. C_L is a ligament constant, equal to 0.5. The breakup of the ligament into drops is obtained from Weber's analysis for capillary jets. The resulting drop size is given by

$$d_o = 1.88\, d_L (1 + 3Oh)^{1/6} \quad (3.18)$$

In the above equation, *Oh* is the Ohnesorge number defined as $Oh = \mu_l / (\rho_l \sigma_s d_L)^{1/2}$.

Droplet distribution model

The droplet sizes during spray vary through a wide range from a minimum size to a maximum size. The variation of droplet sizes followed by Rosin-Rammler expression is one of the most convenient representations that has been adopted by various researchers. In this approach the entire mass of liquid injected is divided into finite number of droplet classes as an input and the droplet classes are spread about its mean diameter size in both the directions, with a regular interval from the minimum value of zero to the maximum value. Then the mass fractions of droplet classes are calculated by following the relation as given below:

$$Y_d = 1 - e^{-(d/\bar{d})^n} \tag{3.19}$$

where, Y_d is the mass fraction with diameter less than d, d is the diameter of any droplet class, $\bar{d}$ is the mean droplet diameter class and n is the dispersion parameter. The spread parameter takes an important role in order to obtain the mass fraction distribution for the droplet classes. It has been found from most of the works available in literature that, the dispersion parameter is always kept in between 3 to 4. However in this work, the dispersion parameter is taken as 3.5 [130].

3.3 Dispersed phase flow model

The Eulerian approach is a well known method to solve the continuous or gas phase problem. In order to obtain the flow field in a turbulent, reacting flow, the Favre averaged governing equations are solved simultaneously. On the other hand, the mass, velocity and temperature histories of the liquid droplets are tracked in the continuous phase using a Lagrangian approach. When both continuous phase and discrete phase are considered together in a flow system, the solution methodology is called as Eulerian-Lagrangian approach. With the consideration of evaporative liquid droplet travelling inside the gas phase region, the exchange of momentum takes place between the two phases due to drag resistance. Moreover the exchange of heat energy

in between the two phases also occurs if a temperature difference exists between the phases. The mass exchange in between the two phases occurs due to the evaporated fraction of the liquid diffusing into the continuous phase. In order to compute the inter-phase source terms over the life time of the droplets, the spray is considered to comprise of a finite number of droplet classes distributed over an initial dispersion angle. The velocity, mass and temperature histories of each of the droplet classes can be obtained along their trajectories using the respective conservation equations in a Lagrangian frame.

The trajectory of a droplet of the k_{th} class is computed by evaluating the velocity and position of a representative droplet of the class along its motion. The velocity of the droplet is found out from the conservation of momentum equation considering only inertia and drag forces to be significant. The equation can then be written as,

$$m_d(k)\frac{du_{d_i}(k)}{dt} = \frac{\pi}{8}\overline{\rho}\left[d(k)\right]^2\left|u_i - u_{d_i}(k)\right|\left[u_i - u_{d_i}(k)\right]C_{drag} \tag{3.20}$$

where, C_{drag} is the drag coefficient on the droplet, which is evaluated following the spherical drag law [131]. The effect of gas phase turbulence on the droplet dispersion is simulated using a stochastic approach. Instantaneous gas phase velocity (u_i) around the droplet is obtained in the above equation by computing the fluctuating velocity following a discrete random walk model. The position of the droplet is obtained by integrating the velocity over short time range. If any droplet, in course of its motion, strikes the combustor wall, it is assumed to reflect from the wall following elastic collision.

Evaporation of the liquid from the surface of the droplets takes place considering the vapour pressure on the droplet surface to be equal to the saturation pressure at the droplet temperature. A piecewise linear variation of the saturation pressure for the liquid fuel with temperature is considered for evaluation. The mass transfer coefficient (h_D) is calculated from the Sherwood number correlation of Ranz and Marshall [132,133]. The change in droplet mass of the kth class can therefore be accounted as,

$$\frac{dm_d(k)}{dt} = \pi d(k)_d^2 h_D\left(C_{f_s} - C_f\right) \tag{3.21}$$

where, C_{f_s} and C_f are the mass fractions of the fuel vapour on the droplet surface and in the surrounding gas.

In order to find out the variation of temperature of the droplet an energy balance across the droplet surface for the k^{th} class is considered as,

$$m_d(k) c_{d_p} \frac{dT_d}{dt} = h_c A_p (T - T_p) - \frac{dm_d(k)}{dt} \Delta H_v \tag{3.22}$$

The heat transfer coefficient (h_c) is found out from the Nusselt number correlation of Ranz and Marshall [132,133] and the radiation exchange with the gas phase is neglected.

The liquid phase conservation equations are solved for each of the droplet classes along their trajectories till each class gets completely evaporated. The inter-phase source terms for mass, momentum and energy are accordingly computed at different grid points depending upon the positions of the droplets and are used in the gas phase equations.

3.4 Combustion models

In order to simulate turbulent combustion, many models are used, which have been discussed in the literature review. We compared three different turbulent combustion models in this work, viz. eddy dissipation model, constrained equilibrium model and laminar flamelet model, to study diffusion flame inside the gas turbine combustor. The details of these models are discussed in the following.

In non-premixed combustion, (diffusion flame) the fuel and oxidiser mix at the flame surface during combustion. During the mixing process, reaction occurs at a certain temperature within a thin region (reaction zone), where the reactant components reach at stoichiometric ratio. As a consequence huge amount of heat releases, which increases the temperature of the entire system. If the rate of transport from the flame zone increases, the reaction process retards with fast decrease in temperature of the flame and finally the reaction stops. In order to physically describe the phenomenon, a non-dimensional number called Damkohler number (Da) is used which is expressed as

$$Da = \frac{\text{Diffusion time scale}}{\text{Reaction time scale}}$$

Damkohler number signifies whether the chemical reaction rate is very fast ($Da >> 1$) or slow ($Da << 1$), as compared to the diffusion (transport) rate. With the increase in turbulence, diffusion time scale decreases thus reducing *Da*. On the other hand, reaction time scale depends on the temperature of the flame. With the increase in temperature, reaction time scale decreases increasing *Da*. At equilibrium state, when the rates of formation of the products become high (the reaction time scale is smallest), the Damkohler number becomes much greater than one ($Da >> 1$). At this condition the temperature and pressure of the system also reach high values.

3.4.1 Eddy dissipation model

In a diffusion flame, the oxygen and fuel eddies occur separately. Since the rates of reactions are assumed to be very fast, the reaction rate is determined by the intermixing rate of species in a turbulent scale. Therefore this model considers that the dissipation of eddies containing different species determine the reaction rate for different conditions. The chemical time scale is replaced by turbulent time scale $\left(k/\varepsilon\right)$ to determine the reaction rate. In addition to that, the mean species mass fraction of the deficient species takes an active part to determine the rate of reaction. Therefore, when the fuel species is deficient, the reaction rate is determined as

$$\tilde{\dot{\omega}}_f = B\bar{\rho}\frac{\varepsilon}{k}\tilde{Y}_f \tag{3.23}$$

where, *B* is a model constant that may depends up on flame structure and reaction rate between fuel and oxygen. $\tilde{Y}_f$ is the mean mass fraction of fuel.

In the flame, where the mass concentration of fuel is dominant as compared to the oxygen concentration, oxygen will be the controlling reacting species. Therefore the dissipation of oxygen eddies will be predominant. Thus the expression for the reaction rate is

$$\tilde{\dot{\omega}}_{O_2} = B\bar{\rho}\frac{\varepsilon}{k}\left(\frac{\tilde{Y}_{O_2}}{\gamma}\right) \tag{3.24}$$

where, $\tilde{Y}_{O_2}$ is the mean mass concentration of oxygen and γ stoichiometric ratio of oxygen to fuel.

In order to obtain the reaction rate where the mass fraction of hot products are less, the dissipation of hot products eddies must be considered. In this case the reaction rate is expressed as

$$\tilde{\dot{\omega}}_p = B\bar{\rho}\frac{\varepsilon}{k}\left(\frac{B_1\sum\tilde{Y}_P}{1+\gamma}\right) \tag{3.25}$$

where, B_1 is another constant, $\sum\tilde{Y}_P$ is the mean mass concentration of the whole products.

Finally, the smallest rate among the above three reaction rates (Eqn. 3.23, 3.24and 3.25) has been considered to determine the local combustion rate.

3.4.2 Flamelet models

In this model, the turbulent non-premixed flame is assumed to be an ensemble of a number of small laminar diffusion flamelets, where chemical reaction is solved following a detailed kinetics of reaction. Here the entire thermo-chemistry is transformed into a function of a single parameter called mixture fraction under the consideration of unique diffusivity among all the species. Therefore a large number of species transport equations are not required to solve. The model solves the Favre averaged transport equations of mixture fraction and its variance in the gas phase using their respective conservation equations. In this method, the complex combustion problem is simplified into a mixing problem. However, unlike the instantaneous cases, the mean scalar quantities are not linearly related to the mean mixture fraction under turbulent situation. Therefore in order to obtain the mean scalar quantities of species and temperature, a special statistical approach, called probability density function (PDF), has been considered.

In this approach the relation in between the instantaneous scalar variables and the instantaneous mixture fraction are previously known and the mean scalar quantities are evaluated with the help of a probability density function. The probability density function, also known as presumed probability density function, has been described in detail in the following.

In this work we considered two such flamelet base models for predicting the combustion process, viz. laminar flamelet model and constrained equilibrium flamelet model.

Mixture fraction approach

In non premixed modeling fuel and oxidizer are fed through separate inlets. Inside the flow domain where both oxidizer and fuel mix within the flammability limit, combustion starts provided the ignition criteria is satisfied. In this approach, a term has been introduced that represents the quality of the mixture inside the flow field within the range 0 to 1. The new term is called mixture fraction (ξ) which is mathematically expressed in terms of atomic mass fractions as

$$\xi = \frac{\phi_i - \phi_{i,ox}}{\phi_{i,fu} - \phi_{i,ox}} \tag{3.26}$$

where, ϕ_i is a passive scalar (have no source term in transport equation). $\phi_{i,ox}$ and $\phi_{i,fu}$ are the conserved scalars for the oxidiser and fuel stream, respectively. From the above relation it can be seen clearly that, the instantaneous value of scalar variable ϕ_i has a linear relationship with the mixture fraction. Therefore ξ represents all the scalar variables, since the scalar variables are the function of mixture fraction.

The transport equation for Favre mean mixture fraction equation is expressed as

$$\frac{\partial}{\partial x_j}\left(\overline{\rho}\tilde{u}_j\tilde{\xi}\right) = \frac{\partial}{\partial x_j}\left(\frac{\mu}{Sc}\frac{\partial\tilde{\xi}}{\partial x_j} - \overline{\rho}\,\widetilde{\xi''u_j''}\right) + \dot{S}_\xi \tag{3.27}$$

where, μ is the molecular viscosity and Sc is the molecular Schmidt number. $-\overline{\rho}\,\widetilde{\xi''u_j''}\left(=\frac{\mu_t}{Sc_\xi}\frac{\partial\tilde{\xi}}{\partial x_j}\right)$ is the turbulent flux of mixture fraction. μ_t is the turbulent viscosity and Sc_ξ is the turbulent Schmidt number. $\dot{S}_\xi$ is the source term used in liquid fuel combustions due to inter-phase transport.

Probability density function

Mixture fraction is a fluctuating quantity that fluctuates with respect to time due to turbulence in the flow. The concept of the probability density function is explained with the help of **Figure 3.1**. In this figure, x-axis represents the range of mixture fraction (0 to 1) and y-axis represents the probability density function of variable ξ. It

has been noted that the distribution curve is randomly chosen for a particular co-ordinate within the flow region for demonstration. The nature of curve is pre determined that has been drawn with the data obtained from a number of experiments. The probability for finding ξ within the range ξ_1 to ξ_2 for a particular coordinate inside the computational domain is $\int_{\xi_1}^{\xi_2} P(\xi) d\xi$. Probability for finding ξ within the entire range (0 to 1) for this particular coordinates in side the computational domain is $\int_0^1 P(\xi) d\xi = 1$.

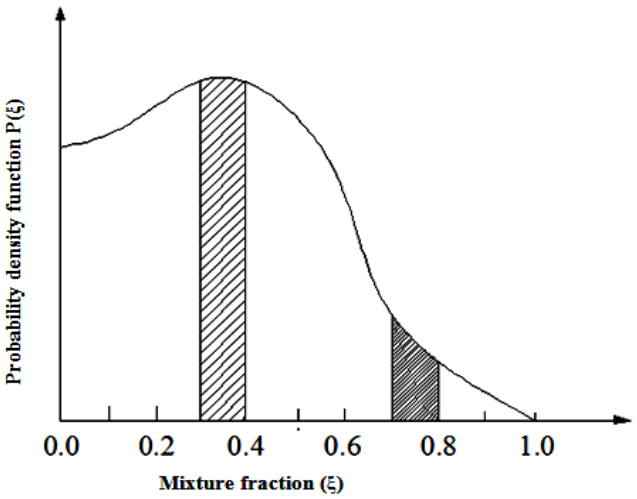

Figure 3.1 A conceptual graph between PDF and mixture fraction

Since, the instantaneous scalar variables are function of instantaneous mixture fraction, the mixture fraction probability density function can be used to determine the mean quantity of any scalar variable by integrating the scalar variables jointly with the corresponding probability density function.

Since Favre mean quantities are the required output in this work, the instantaneous probability density function ($P(\xi)$) is required to be converted to Favre PDF ($\tilde{P}(\xi)$) to calculate the Favre mean scalar variables within the flow field. The Favre PDF can be expressed as,

$$\tilde{P}(\xi) = \frac{\rho(\xi)}{\overline{\rho}} P(\xi) \tag{3.28}$$

The Favre mean scalar quantities are obtained by integrating the Favre PDF along with scalar variables $\phi(\xi)$ jointly. It is expressed as

$$\tilde{\phi} = \int_0^1 \phi(\xi)\tilde{P}(\xi)d\xi \tag{3.29}$$

In this work β-PDF distribution function has been used to determine the local probability density function. The β-PDF is not only a function of the instantaneous mixture fraction, but also of mean mixture fraction and mixture fraction variance. The β-PDF is defined as

$$\tilde{P}(\xi) = \frac{\xi^{\alpha-1}(1-\xi)^{\beta-1}\Gamma(\alpha+\beta)}{\Gamma(\alpha)\Gamma(\beta)} \tag{3.30}$$

$$\text{where, } \alpha = \tilde{\xi}\left[\frac{\tilde{\xi}(1-\tilde{\xi})}{\tilde{\xi}''^2} - 1\right] \text{ and } \beta = (1-\tilde{\xi})\left[\frac{\tilde{\xi}(1-\tilde{\xi})}{\tilde{\xi}''^2} - 1\right] \tag{3.31}$$

Mixture fraction variance

In order to generate the β-PDF, it is required to obtain the Favre mean mixture fraction ($\tilde{\xi}$) equation and mixture fraction variance ($\tilde{\xi}''^2$) as well [134].

The transport equation for the mixture fraction variance is expressed as

$$\frac{\partial}{\partial x_j}\left(\bar{\rho}\tilde{u}_j\tilde{\xi}''^2\right) = \frac{\partial}{\partial x_j}\left(\frac{\mu}{Sc}\frac{\partial\tilde{\xi}''^2}{\partial x_j} - \bar{\rho}\,\widetilde{\xi''^2 u_j''}\right) + C_{g1}\mu_t\left(\frac{\partial\tilde{\xi}''^2}{\partial x_j}\right)^2 - \bar{\rho}C_x\tilde{\chi} \tag{3.32}$$

where, μ is the molecular viscosity and Sc is the molecular Schmidt number. $-\bar{\rho}\,\widetilde{\xi''^2 u_j''}\left(=\frac{\mu_t}{Sc_\xi}\left(\frac{\partial\tilde{\xi}''^2}{\partial x_j}\right)\right)$ is the turbulent flux of mean mixture fraction variance. μ_t is the turbulent viscosity Sc_ξ is the turbulent Schmidt number and C_{g1} is the model constant. The second term of right hand side of the above equation is the generation rate of mean mixture fraction variance where as the last term of right hand side is the rate of destruction of mean mixture fraction variance. $\tilde{\chi}\left(=C_x\frac{\tilde{\varepsilon}}{\tilde{k}}\tilde{\xi}''^2\right)$ is the scalar dissipation rate and the detail of it has been discussed in following sub-section.

3.4.2.1 Laminar flamelet model

Laminar flamelet model is used to simulate the turbulent combustion by considering the multi step finite rate chemistry. It has been seen in an opposed flame that, if either of the velocity of fuel or oxidant is increased from the chemically correct supply, the flame is strained and the thin reaction zone diminishes in size. Consequently the rates of transport of scalars, such as temperature and species concentrations, increase as compared to the reaction rate. That means, the diffusion time scale becomes smaller than chemical time scale ($Da << 1$). Thus the reaction departs from equilibrium and finally the flame extinguishes. In the laminar flamelet model, a term called scalar dissipation rate (χ), represents straining of flame that signifies the departure of chemistry from equilibrium state. It is inversely proportional to Damkohler number. Physically the instantaneous scalar dissipation rate can be defined as

$$\chi = 2 D_{\xi} \left(\frac{\partial \tilde{\xi}}{\partial x_i} \right)^2 \tag{3.33}$$

where, D_{ξ} is the diffusivity of mixture fraction. The Favre mean of scalar dissipation rate is expressed as

$$\tilde{\chi} = C_{\chi} \frac{\tilde{\varepsilon}}{\tilde{k}} \tilde{\xi}''^2 \tag{3.34}$$

where, the value of constant C_{χ} is 2.0. A reference scalar dissipation rate called instantaneous stoichiometric scalar dissipation rate (χ_{st}) is set to differentiate the mixture quality on which only mixing calculation will be considered and where the combustion calculations will be performed. If the scalar dissipation rate is much greater than stoichiometric scalar dissipation rate (χ_{st}), the flame width will be diminished and there will be no chemical reaction in that region and only the mixing process will be calculated in this region. The minimum value of scalar dissipation (χ_{ext}) at which the combustion process will stop (flame quenching) is called extinction strain rate. However if scalar dissipation rate (χ_{st}) tends to zero, the chemistry will be near equilibrium. Therefore scalar dissipation rate (χ_{st}) measures the departure of flamelet from equilibrium and it is expressed as

$$\chi_{st} = \frac{a_s \exp\left(-2\left[erfc^{-1}(2\xi_{st})\right]^2\right)}{\pi} \tag{3.35}$$

where, a_s is the characteristic strain rate, ξ_{st} is the stoichiometric mixture fraction, $erfc^{-1}$ is the inverse complementary error function.

The relationship among the various scalar variables (like species concentrations and temperature) with instantaneous mixture fraction and instantaneous scalar dissipation rate across the finite numbers of laminar flamelets are generated by solving in an opposed laminar diffusion flame. The procedure for creating a library to establish a relationship among the various scalar variables with instantaneous mixture fraction is called flamelet generation. The flamelet equation for general scalar such as species in mixture fraction space is expressed as

$$\rho \frac{\partial \phi_k}{\partial t} - \rho \frac{\chi}{2} \frac{\partial^2 \phi_k}{\partial \xi^2} - \dot{\omega}_k = 0 \tag{3.36}$$

The flamelet equation for temperature in mixture fraction space is expressed as

$$\rho \frac{\partial T}{\partial t} - \rho \frac{\chi}{2} \frac{\partial^2 T}{\partial \xi^2} - \frac{1}{c_p} \frac{\partial p}{\partial t} + \sum_{i=1}^{N} \frac{h_k}{c_p} \dot{\omega}_k = 0 \tag{3.37}$$

where, $\dot{\omega}_k$ is the reaction rate of k_{th} species.

By using the above equations the entire chemistry is transformed in terms of mixture fraction and scalar dissipation rate. Therefore the entire problem is performed within two steps. In first step the relation between scalar variables and mixture fraction at different scalar dissipation rate is established along with turbulent interaction in chemistry by using PDF. Hence the computational time reduces by avoiding the calculations of numbers transport equations for different species.

The effect of heat loss on the flamelets, due to radiation and inter-phase transport (for spray combustion), are accounted through a non-adiabatic extension of the laminar flamelet model considering instantaneous enthalpy as a variable. The solution of the scalar equations generates a flamelet library, which is a collection of scalar variables as functions of mixture fraction, scalar dissipation rate and instantaneous enthalpy as, $\phi(\xi, \chi, H)$.

The effect of turbulent fluctuation on the scalar variables has been accounted using a statistical distribution employing a joint probability density function (PDF) in mixture fraction, scalar dissipation rate and enthalpy. A density-weighted joint PDF

$\tilde{P}(\xi, \chi, H)$ has been considered using which the mean scalar variables can be evaluated as,

$$\tilde{\phi} = \int_0^{\infty}\int_0^{\infty}\int_0^{1} \phi(\xi, \chi, H)\tilde{P}(\xi, \chi, H)\, d\xi\, d\chi\, dH \tag{3.38}$$

The variables in the joint probability density function have been assumed to be statistically independent. So the joint PDF can be expressed as the product $\tilde{P}(\xi)\tilde{P}(\chi)\tilde{P}(H)$. The PDF for mixture fraction ($\tilde{P}(\xi)$) is presumed to be a beta function as given in equation 3.52.

On the other hand, fluctuation in scalar dissipation rate is ignored and its PDF ($\tilde{P}(\chi)$) is taken as a delta function at the mean value [117]. Further, the enthalpy fluctuations are assumed to be mainly due to mixture fraction fluctuations and independent of the enthalpy levels [70]. Therefore, the PDF in enthalpy is also taken as $\tilde{P}(H) = \delta\left(H - \tilde{H}\right)$. Equation (3.29) is therefore, re-written as $\tilde{\phi} = \int_0^{1} \phi\left(\xi, \tilde{\chi}, \tilde{H}\right)\tilde{P}(\xi)\, d\xi$ and is used to determine the scalar variables in the flow field using the mean values of scalar dissipation rate and enthalpy.

A chemical kinetic model of kerosene ($C_{12}H_{23}$) combustion involving 17 species (such as $C_{12}H_{23}$ C_2H_2 CH CO CO_2 O_2 O OH H_2 H H_2O HO_2 NH N NO N_2O N_2) and 26 reactions, as proposed by Kundu et al. [135], has been adopted to generate the species source terms is given in **Table 3.1**. Total nine flamelets, having scalar dissipation rates of 0.01 s^{-1}, 0.1 s^{-1}, and then 1 to 13 s^{-1} with an increment of 2 s^{-1}, are considered in the present model. It has been found that extinction of flame occurs at a value of scalar dissipation rate higher than 13 s^{-1}.

Table 3.1 Chemical kinetics for kerosene surrogate fuel.

No	**Reaction**	**Pre-exponetial factor (*A*) cm^3/gmole**	**b**	**Activation energy (E_A) cal/gmole**
1	N2+C12H23=>12CH+11H+N2	4.35E+09	0.0	30000
2f	CH+H2+N2=>2NH+CH	1.00E+15	0.0	78000
2b	CH+2NH=>N2+H2+CH	1.95E+15	0.0	0.0

3	H2+OH=H2O+H	1.17E+11	1.3	3626
4	H2+O=H+OH	2.50E+15	0.0	6000
5	H+O2=O+OH	4.00E+14	0.0	18000
6f	N2+O2=>2O+N2	1.00E+18	0.0	122239.0
6b	H2+2O=>O2+H2	1.00E+18	0.0	0.0
7	H2+2H=2H2	2.00E+17	0.0	0.0
8	H+O2=HO2	1.00E+15	-1.01	0.0
9	H+HO2=H2+O2	6.50E+13	0.0	0.0
10	O+HO2=OH+O2	2.50E+13	0.0	0.0
11	CO+HO2=CO2+OH	5.80E+13	0.0	22934.0
12	CO+OH=CO2+H	1.51E+07	1.28	-758.0
13	CH+O=CO+H	3.00E+12	1.0	6000
14	CH+OH=CO+H2	3.00E+13	0.0	0.0
15	CH+NO=NH+CO	1.00E+11	0.0	0.0
16	N2+2CH=C2H2+N2	1.00E+14	0.0	0.0
17	C2H2+O2=2CO+H2	3.00E+16	0.0	19000.0
18	N2+O=N+NO	6.50E+13	0.0	75000
19	N+O2=NO+O	6.30E+09	1.0	6300
20	N+OH=NO+H	3.00E+11	0.0	0.0
21	NH+NO=N2O+H	2.00E+15	-0.8	0.0
22	N2O+OH=N2+HO2	3.20E+13	0.0	0.0
23	N2O+O=2NO	6.00E+14	0.0	28200
24	N2O+O=N2+O2	6.00E+14	0.0	28200
25	N2O+H=N2+OH	1.50E+12	0.0	0.0
26	NH+O=NO+H	2.50E+04	2.64	0.0

3.4.2.2 Constrained equilibrium model

In the equilibrium flamelet model, the species in the flamelets are assumed to be in chemical equilibrium depending on mixture fraction considering very fast chemical reactions. The equilibrium composition and temperature of the flame are calculated as a function of mixture fraction based on thermodynamic consideration using Gibbs free energy, obviating the necessity of any specific chemical mechanism. In the present work, sixteen chemical species (O_2, N_2, $C_{12}H_{23}$, CO_2, CO, H_2O, H_2, OH, H, O, HO_2, H_2O_2, HCO, CHO, HONO, HCOOH) have been considered in the equilibrium product mixture following chemical reaction.

However, the equilibrium assumption does not work well across the entire flame region because of flame stretch. It has been found in the literature that, in the fuel-rich region of the flame large departure from equilibrium is observed [136]. In the present work, a constrained condition, based on a limiting equivalence ratio, has been used to account the departure from equilibrium [77, 78]. At locations where the equivalence ratio limit is exceeded, the species are considered to be a mixture of pure fuel and a leaner equilibrium burnt mixture. The same methodology was earlier used by Hossain and Malalasekera [78] in a gaseous non-premixed flame. However, here the limiting criterion has been fixed by accounting the scalar variables in the rich region and the scalar dissipation rates in the corresponding zone of the spray flame. More details on the choice of the constrained condition based on the model predictions are given in Chapter 5.

3.5 Radiation model

Radiation is important in hydrocarbon fuel combustion because the product gases, especially CO_2 and H_2O, actively participate in radiation heat transfer. Moreover, the formation of soot enhances the radiation heat loss from the flame due to the high emissivity of soot. The radiative heat exchange has been simulated by using discrete ordinate (DO) model [137], with the radiative transfer equation solved for a finite number of angular directions ($\vec{s}_i$, $i = 1, 2, 3 \ldots\ldots\ldots n$) throughout the span of 4π solid angle. Scattering is neglected by assuming that the particles in the flame are extremely fine and well dispersed. The reduced form of the radiative heat transfer equation is given as

$$\frac{d\, I_i(r, \vec{s}_i)}{d\, s} = \kappa\, I_b(r) - \kappa\, I_i(r, \vec{s}_i) \tag{3.62}$$

where, I_i is the radiation intensity in the *i*th direction, I_b is the radiation intensity of blackbody, r is the position vector, $\vec{s}_i$ is the direction vector in *i*th direction and κ is the combined absorptivity considering both the absorptivity of the gas phase (κ_{gas}) and soot (κ_{soot}).

Absorptivity of bulk gas has been evaluated by weighted sum gray gas model (wsggm) [137] with the constant gray gas absorption coefficient (κ_k) for the

participating gases ($k = 0, 1, 2, 3 \ldots\ldots K = k - 1$) along with suitable weighing factors (a_k) given as

$$\kappa_{gas} = - \frac{\ln \left[1 - \sum_{k=0}^{k-1} a_k \left(1 - e^{-\kappa_k p_k} \right) \right]}{z} \tag{3.63}$$

where, p_i is the total partial pressure of all the participating gases and z is the path length. The weighing factor a_k is considered as a polynomial function of temperature and it is given as,

$$a_k = \sum b_{k,j} T^j \tag{3.64}$$

The absorption coefficient fraction contributed by soot (κ_k) is considered as a linear function of temperature and is given as [117],

$$\kappa_{soot} = 1232 .4 \rho_{soot} \left[1 + 4.8 \times 10^{-4} (T - 2000) \right] \tag{3.65}$$

The energy source term due to radiation has been evaluated as,

$$S_{rad} = \nabla . \overline{q}_{rad} = \kappa \left(4 \sigma T^4 - \sum_{i=1}^{N} w_i I_i \right) \tag{3.66}$$

where, w_i is the quadrature weight associated with the direction i in the discrete ordinate method.

Chapter 4

Modelling of Soot Formation in Combustion

4.1 Physical process of soot formation

Soot is an agglomerate of millions of carbon atoms along with few hydrogen and oxygen atoms. The size and configuration of soot particles are different for different flames. But most often soot particles are considered to be spherical in shape. Even though some differences in physical and chemical structures of soot has been observed in different flames, the basic physical and chemical processes involved in soot formation are same irrespective of the types of flames and fuels. Formation of soot occurs under fuel rich circumstance at higher temperature during combustion. Diffusion flame releases more soot than premixed flame due to the higher local equivalence ratio present in the flame. The formation soot occurs through various steps such as

1. Particle inception /Nucleation
2. Surface growth
3. Coagulation and Agglomeration
5. Oxidation

4.1.1 Particle inception/ Nucleation

It is the first process in which solid soot particles are formed from the gas phase of the species. However, the exact processes occurring during this first step of transition from the gas to solid phase is still a somewhat unknown phenomenon. Various

mechanisms for the inception of first soot particle have been proposed by different researchers. By using the fuel mass fraction at inlet [138,97,87], polyacetylene [104] and polycyclic aromatic hydrocarbons (PAH) [139] are used as precursor to evaluate the rate of soot inception. The current studies on soot formation are conducted on the basis of large polycyclic aromatic hydrocarbons.

An example of poly aromatic hydrocarbon model proposed by Hall et al.[139] for higher hydrocarbons is that, the rate of soot inception is based on the formation of two and three ring aromatics ($C_{10}H_7$ and $C_{14}H_{10}$) from acetylene (C_2H_2), benzene (C_6H_6) and Phenyl (C_6H_5) species. It is based on the mechanism given as,

$$2C_2H_2+C_6H_5 \leftrightarrow C_{10}H_7+H_2 \quad (4.1)$$

$$C_2H_2+C_6H_6+C_6H_5 \leftrightarrow C_{14}H_{10}+H+H_2 \quad (4.2)$$

In this model acetylene (C_2H_2), benzene (C_6H_6) and Phenyl (C_6H_5) are used as precursor to determine the rate of soot formation.

In fuel mass fraction at inlet models, fuel mass fraction is used as a soot precursor. But in the current study we use poly-acetylene model. Here only acetylene is used as precursor species to determine the soot formation rate.

4.1.2 Surface growth

Although nucleation of soot particles contributes a major fraction to determine the quantity of soot particles but, most of the soot mass is not resulted by the nucleation process. A major mass of soot has been formed by the reaction between soot particles and gas phase species [81]. Most of the hydrocarbons (especially C_2H_2) react on the surface of the nucleated soot particles and hence the particles become grown up [140]. Therefore, both in acetylene model and PAH model [98 ,104] only acetylene (C_2H_2) is used as surface growth species of soot.

4.1.3 Coagulation and Agglomeration

Once the soot particles have been formed, they collide with each other and stick among themselves forming larger particles. From experiments it has been observed that relatively small particles coalesce into almost spherical form during collision and this growth mechanism of particle called coagulation. However this process is a

physical phenomena and it depends upon the frequency of collision between the particles. Therefore after all, the rate of coagulation may be evaluated through a direct relationship with soot number density (number of soot particles per unit volume) multiplied with some proportionality constant called coagulation rate constant. However, the coagulation rate constant depends up on the ratio of mean free path to diameter of soot particle. If the diameter of the particle is much smaller as compared to the mean free path, the coagulation is said to be in free-molecular regime and the collision frequency is governed by the kinetic theory. However, as most of the soot particle diameter is too small, the assumption behind the coagulation process has been considered as in the free-molecular regime.

Moreover, the collision between relatively larger particles form chains and developed into larger masses. The development of bigger mass from large particles is called agglomeration. The process of agglomeration is much slower than coagulation, and therefore the shapes of agglomerated soot are not spherical and its surface is also less smooth than the coagulated soot. However, since there are few larger soot particles present as compared to many small particles, the agglomerated soot has not been considered by most of the researchers and only the coagulation process is taken into account.

4.1.4 Oxidation

During the surface growth process not only a major mass of soot has been formed by the reaction between soot particles and gas phase species, but the combustion of soot also occurs during this period. O_2 and OH are the most active oxidisers that oxidised the soot inside the flame. The reaction mechanisms for oxidation of soot are given as

$$1/2O_2+C(S)\rightarrow CO \quad (4.3)$$

$$OH+C(S)\rightarrow CO+H \quad (4.4)$$

The rate of reactions have been determined by considering the kinetic theory of gases.

4.2 Soot model

It has been discussed in the literature review that basically three types of soot models are used in the computational works, viz. empirical, semi-empirical and detailed models. Brookes and Moss [98] proposed one of the semi-empirical acetylene-based

soot model that has been developed for lower hydrocarbon such as methane (CH_4). However since the rate of soot formation is much slower than the combustion reactions, separate transport equations for soot mass fraction and nuclei concentration are to be solved. The transport equations are given as

$$\frac{\partial}{\partial x_i}\left(\overline{\rho}\tilde{u}_i\tilde{Y}_{soot}\right)=\frac{\partial}{\partial x_i}\left(\frac{\mu_t}{\sigma_{soot}}\frac{\partial\tilde{Y}_{soot}}{\partial x_j}\right)+\frac{dM}{dt} \tag{4.5}$$

(4.5)

$$\frac{\partial}{\partial x_i}\left(\overline{\rho}\tilde{u}_i\tilde{b}_{nuc}\right)=\frac{\partial}{\partial x_i}\left(\frac{\mu_t}{\sigma_{nuc}}\frac{\partial b_{nuc}}{\partial x_j}\right)+\frac{1}{N_{norm}}\frac{dN}{dt} \tag{4.6}$$

Where $\tilde{Y}_{soot}$ is the soot mass fraction, M is the soot mass concentration, $\tilde{b}_{nuc}\ (=N/\rho N_{norm})$ is normalized radical nuclei concentration, N is soot number density (particles per cubic meter) and N_{norm} =10^{15} particles. σ_{soot} and σ_{nuc} are Prandtl number in soot mass fraction transport equation and nuclei transport equation respectively and their values are taken as 0.6.

The source term for number density (N) has been calculated by considering nucleation and coagulation of soot particles and is given as,

$$\frac{dN}{dt}=\underbrace{C_\alpha N_A\left(\frac{X_{C_2H_2}P}{RT}\right)exp\left(-\frac{T_\alpha}{T}\right)}_{Nucleation}-\underbrace{C_\beta\left(\frac{24\ RT}{\rho_{soot}\ N_A}\right)^{1/2}d_{p_{soot}}^{1/2}\ N^2}_{Coagulation} \tag{4.7}$$

The source term for mass concentration (M) has been evaluated by taking into account nucleation, surface growth and oxidation of soot. The oxidation process has been modelled using the Fennimore-Jones model of soot oxidation. The overall equation of the source term of mass concentration is given as,

$$\begin{aligned}\frac{dM}{dt}=&\underbrace{C_\alpha M_p\left(\frac{X_{C_2H_2}P}{RT}\right)\exp\left(-\frac{T_\alpha}{T}\right)}_{Nucleation}+\underbrace{C_\gamma\left(\frac{X_{C_2H_2}P}{RT}\right)\exp\left(-\frac{T_\gamma}{T}\right)\left[(\pi N)^{1/3}\left(\frac{6M}{\rho_{soot}}\right)^{2/3}\right]^n}_{Surface\ \ Growth}\\&-\underbrace{C_{oxid}C_\omega\eta_{coll}\left(\frac{X_{OH}P}{R\ T}\right)\sqrt{T}\,(\pi N)^{1/3}\left(\frac{6\,M}{\rho_{soot}}\right)^{2/3}}_{Oxidation}\end{aligned} \tag{4.8}$$

4.3 Soot model optimization and validation

In this work, we have considered acetylene (C_2H_2) as the precursor of soot, both in the nucleation and surface growth reactions as shown in the equations above. However we did not consider the C_2H_2 concentration from the adopted chemical kinetic model, as it predicts the soot concentration poorly. Instead, we have considered the empirical data of Moss and Aksit [103], showing the variation of C_2H_2 mole fraction with mixture fraction in the non-premixed combustion of kerosene surrogate fuel.

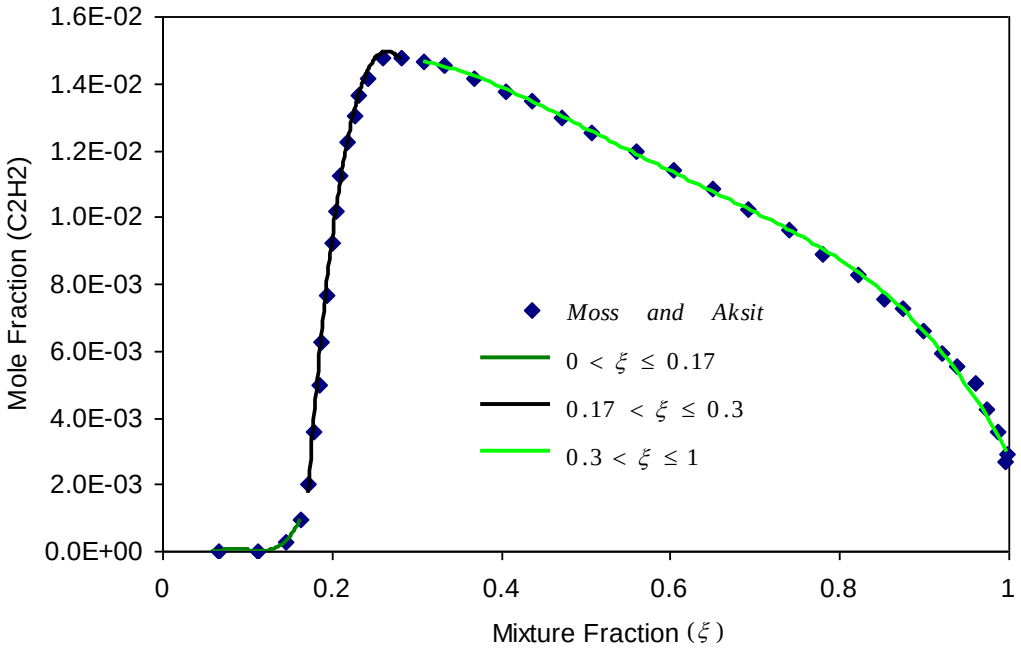

Figure 4.1 Flamelet relationship for mole fraction of C_2H_2 and mean mixture fraction in non-premixed kerosene flame

A curve fitting exercise into the flamelet data of Moss and Aksit, as shown in **Figure 4.1**, gives the following relations between C_2H_2 mole fraction ($X_{C_2H_2}$) and mixture fraction (ξ) in kerosene flame:

For $0 < \xi \le 0.17$: $X_{C_2H_2} = 4.9944\ \xi^3 - 1.5145\ \xi^2 + 0.1481\ \xi - 4.6065 \times 10^{-3}$; (4.9a)

For $0.17 < \xi \le 0.3$: $X_{C_2H_2} = 6.1369\ \xi^3 - 5.8333\ \xi^2 + 1.7998\ \xi - 0.1666$; (4.9b)

For $0.3 < \xi \le 1$: $X_{C_2H_2} = -0.133\ \xi^4 + 0.3081\ \xi^3 - 0.2637\ \xi^2 + 0.08604\ \xi + 0.0053$;(4.9c)

The turbulence-chemistry interaction on soot formation has been accounted using a probability distribution function in mixture fraction. The original model of Brookes and Moss [98] was designed to predict the soot formation in non-premixed flames of lower hydrocarbons, like methane. The values for model constants C_α, C_γ are prescribed as 54, 11700, respectively, for methane [98]. Kerosene has a much higher tendency of forming soot than methane, which is evident in its lower smoke point [141]. Therefore the model constants of the source terms in Equation (4.7) and (4.8) are required to be suitably modified for use with kerosene fuel ($C_{12}H_{23}$).

In order to optimize the model constants in a kerosene non-premixed flame a validation study of the soot model has been separately done for an axi-symmetric burner. Study of soot formation in a similar burner for kerosene-vapour non-premixed flame burning in air was earlier conducted experimentally by Young et al. [142] and computationally by Wen et al. [104]. Laminar Flamelet combustion model is used to simulate the combustion parameters. The Physical model and the computational domain are schematically shown in **Figure 4.2**.

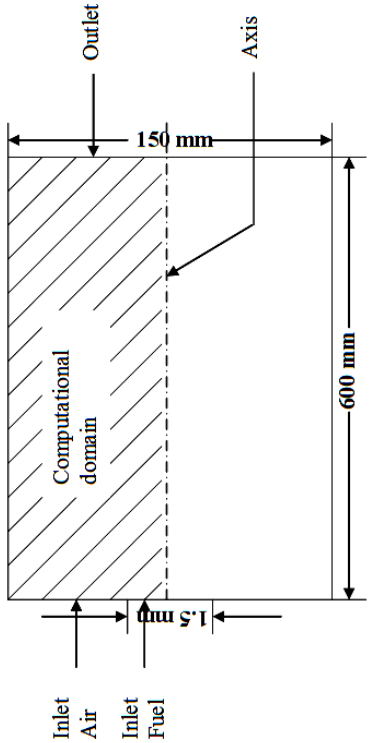

Figure 4.2 Schematic of computational model same as Wen et al.

The choice of the model parameters for kerosene flame have been made by comparing the predictions of soot concentrations with the experimental results of Young et al. [142], as shown in **Figure 4.3.** The prediction of Wen et al. [104], using the PAH concentrations as the precursor in the inception reaction, for the same flame is also plotted in the **Figure 4.3.** We have considered acetylene as the precursor both in nucleation and surface growth reactions. **Figure 4.3** shows a gross under prediction in the soot concentrations when C_α, C_γ values proposed for methane fuel [98] are used in the model for kerosene flame. However, we have also found that even after the modifications in the model constants, the local acetylene concentrations predicted from the adopted chemical kinetics show under prediction of soot concentration with respect to experiments. Therefore, the acetylene concentrations in the flame are taken from the correlations as developed in **Figure 4.1** (Equation 4.9(a) to 4.9(c)) for use in the soot model. Eventually, the predicted soot volume fraction along the axis is found to be fairly close to the experimental results by considering the values of C_α and C_γ as 648 and 140400, respectively, along with a C_{oxid} value of 0.015 for the oxidation process in the soot model of Brookes and Moss [98].

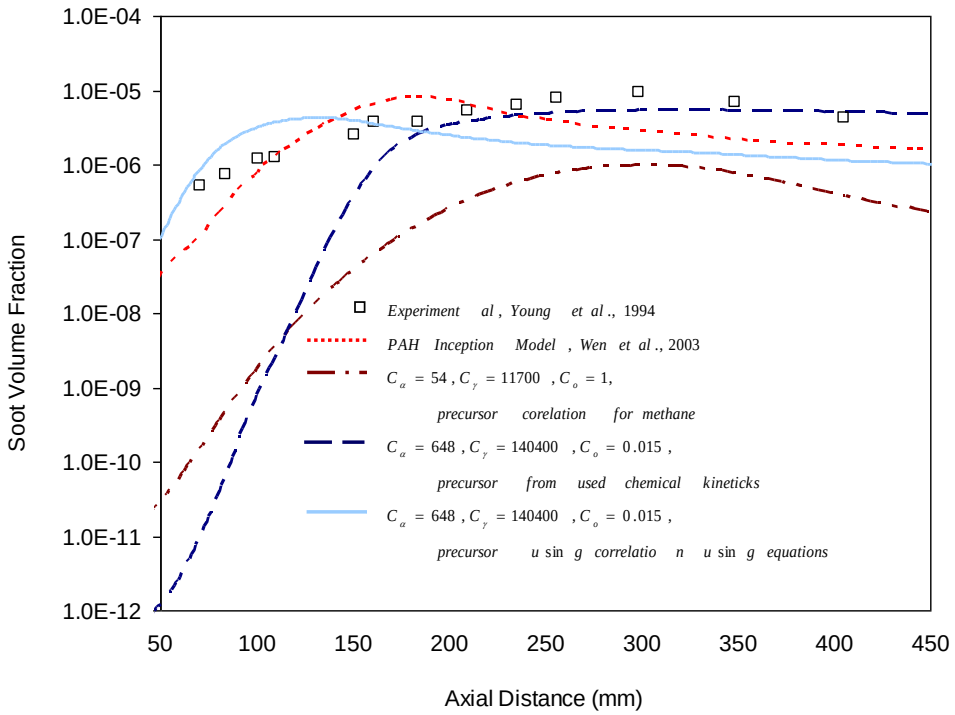

Figure 4.3 Soot volume fraction along the axis of the kerosene jet flame with different model constants and different precursor calculation routes

The radial distributions of soot volume fraction at different location from the inlet are also validated. **Figure 4.4** portrays the soot volume fraction distribution along the radius at 100 mm above the inlet. From this figure it has been shown that, the predicted soot volume fraction near the axis is much better, where as from 7 mm from the axis up to the wall, the predicted soot volume fraction deviate from the experimental results. The **Figure 4.5** that shows the soot volume fraction 300 mm above the inlet reveals that, at the axis, the difference between the predicted and experimental result is in the order of 10. However it becomes closer to the experimental along radial direction and it is much closer near 20 mm from the axis.

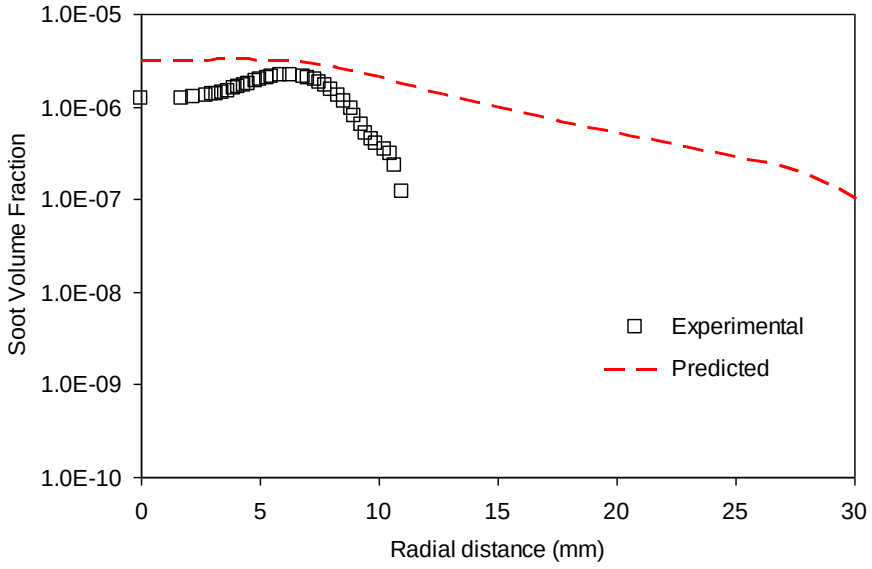

Figure 4.4 Soot volume fraction 100 mm above the inlet

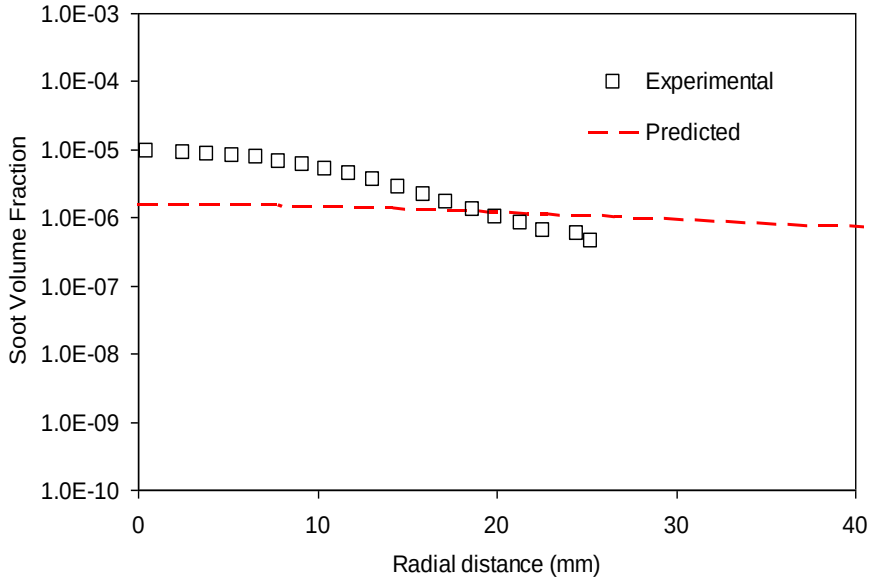

Figure 4.5 Soot volume fraction 300 mm above the inlet

Moreover the temperature along the axis and the radial distribution of temperature above 100 mm and 300 mm from inlet are also validated as shown in **Figure 4.6, 4.7 and 4.8** respectively. It is important because the presence of soot in flame affects the entire temperature field due to the higher emissive property of soot particles. Therefore flame temperature always decreases with increase in soot volume fraction inside the flame. The temperature along the axis (**as shown in Figure 4.6**) with proposed acetylene model is much closer to the experimental from inlet to 150 mm from the inlet. However the maximum deviation of only16% in the temperature distribution has been found at 280 mm from the inlet plane. Moreover near the outlet region the prediction is better. From **Figure 4.7** it has been revealed that the temperature near the axis and near the wall are predicted much better but in the middle region the prediction is not so good where as the nature of distribution follows experimental results. Radial temperature distribution at 300 mm from inlet has been shown in **Figure 4.8**. In this figure also the similar trend has been found like previous figure. The temperature near the axis and wall predicted better but still in the middle region the prediction is not good where as the nature of distribution is similar as experimental results.

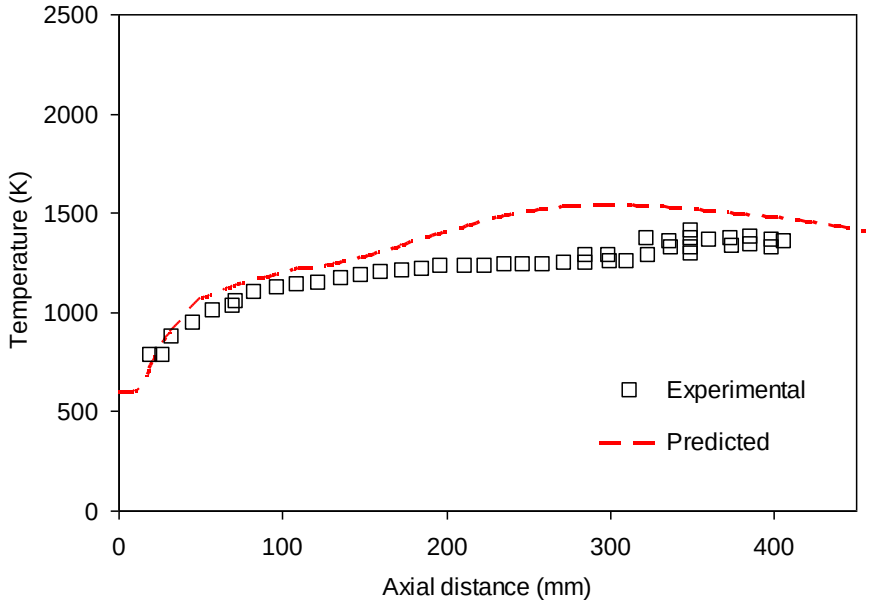

Figure 4.6 Mean temperature along the axis

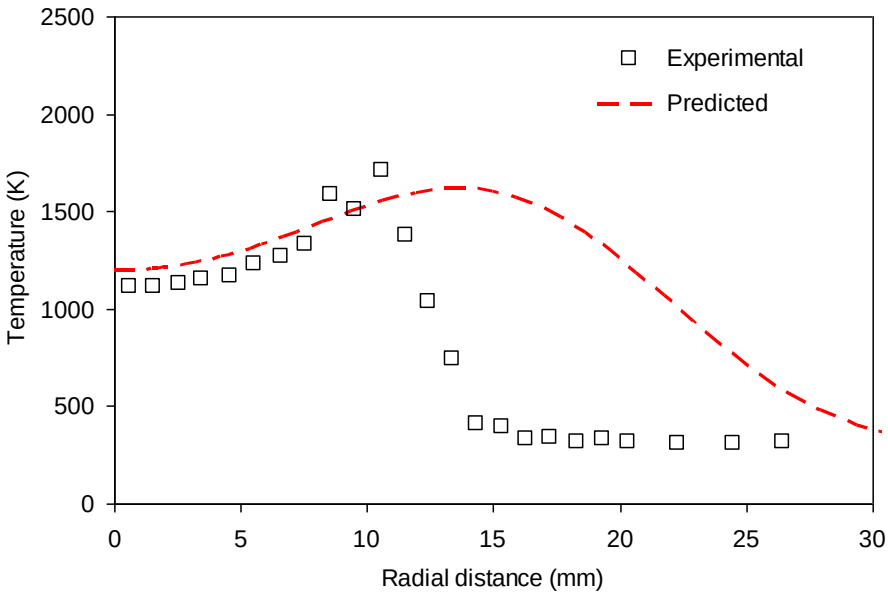

Figure 4.7 Mean temperature 100 mm above the inlet

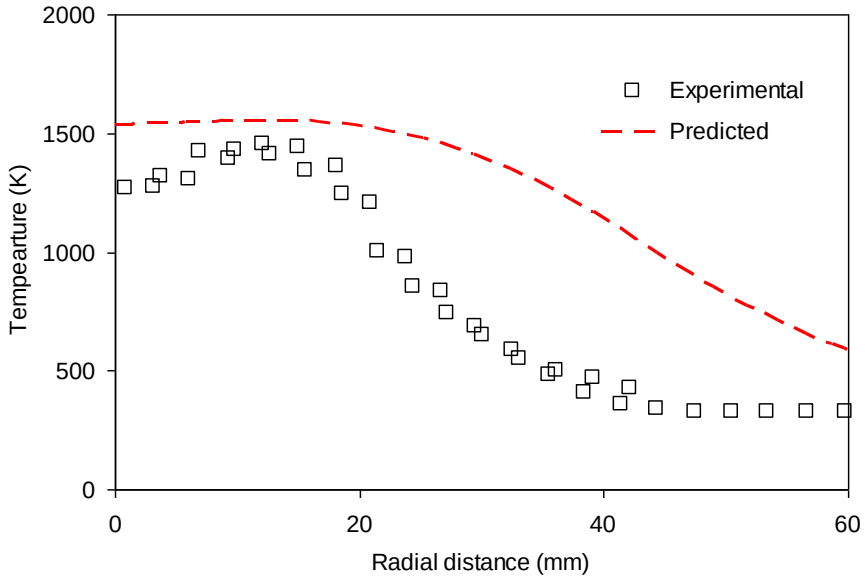

Figure 4.8 Mean temperature 300 mm above the inlet

Other two soot parameters such as soot mass density and soot number density are also compared with PAH model of Wen et al. [104]. In **Figure 4.9** the soot mass density predicted by proposed acetylene model has been compared with PAH model of Wen et al. [104]. In the proposed acetylene model the maximum concentration of soot mass density has been obtained 125 mm from the inlet where as with PAH model it is occurred at 180 mm from the inlet. However, the maximum value of soot mass density has been obtained in order of 1×10^{-2}, where as PAH model gives maximum mass density in order of 1.3×10^{-2}. The minimum values of both the models are also much closer to each other. The minimum soot mass density predicted by acetylene model and PAH model are 2.2×10^{-3} and 3.8×10^{-2} respectively. However the soot mass density predicted by proposed acetylene model may be within the acceptable range. Soot number density prediction has been portrayed in **Figure 4.10.** It has been revealed that the maximum soot number density predicted by proposed acetylene model is less in order of two as compare to PAH model proposed by Wen et al. Where as the minimum soot number density predicted by proposed acetylene model is less in order of three as compare to PAH model.

There is a little deviation of computational results from experimental value is there because surface growth of species may not be predicted much better with

methane as precursor for surface growth. Also the limitation of turbulent model is also a cause behind it. The experimental uncertainty and error is also one of the reason, that may not provides exact results. However due to many assumptions and many empirical constants in a computational model, it always depicts some variation with computational model

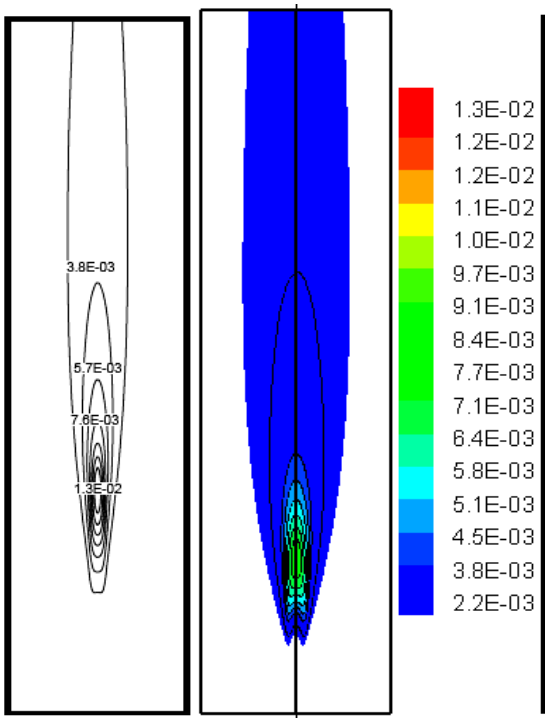

Figure 4.9 Soot mass density (kg/m3)

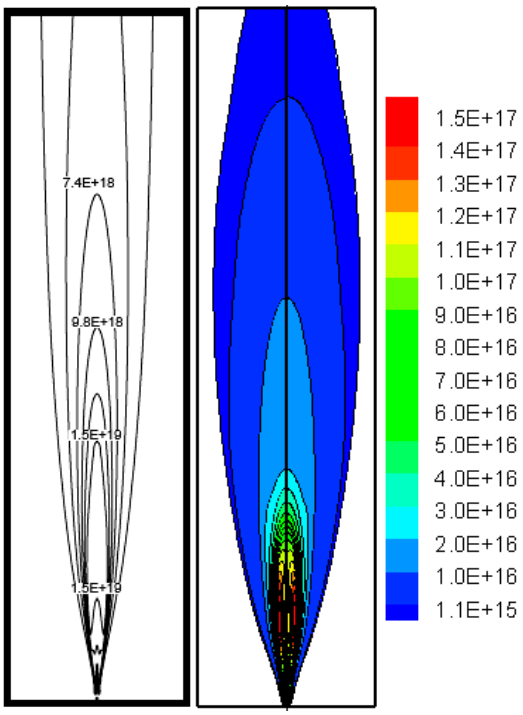

Figure 4.10 Soot number density (Particles/m^3)

4.4 Conclusion

Modelling of soot has been validated with Wen et al. [104]. It has been found that the prediction of soot is good enough along the axis. Predicted soot distribution through radial direction is also fairly closer to experiment. However the temperature distributions along the axis and across the axis have been validated nicely. Moreover soot mass density and soot number density are also predicted through better accuracy since comparing with PAH model of Wen et al. Therefore current developed soot model parameters are used in the following chapters in simulation of combustion process.

Chapter 5

Combustion models: A comparison

5.1 Introduction

The fundamental details of three combustion models, viz. eddy dissipation model, laminar flamelet model and constrained equilibrium model, have already been discussed in chapter 3.4. In the present work, we have simulated a kerosene spray flame in a model combustor of axi-symmetric geometry (**Figure 5.1**) using the above combustion models to compare their predictions. In the eddy dissipation model, the combustion reaction rate is calculated considering single step global reaction chemistry. In the laminar flamelet model, combustion is simulated with detailed reaction kinetics. The turbulence interaction has been accounted using an assumed PDF distribution of mixture fraction. Finally, in the constrained equilibrium model, the flamelets are computed considering chemical equilibrium and using an appropriate constraint condition for accounting the non-equilibrium effects due to transport induced straining. The simulations have been performed using the commercial software ANSYS Fluent (version 13.0). The wall and exit gas temperature distributions and the distribution of soot in the combustor have been predicted using each of the combustion models and the results are compared. Experiments are also performed in a combustor of same geometry and the temperature variations are measured to validate the numerical predictions.

5.2 Physical model

The physical model of the combustor is shown in **Figure 5.1**. It comprises of a cylindrical combustion chamber of diameter 100 mm and length 500 mm. A vane swirler fitted at the entry of the primary air to the combustor contains constant angle (60^O) vanes. The diameters of the hub and tip of the swirler are 20 mm and 50 mm, respectively. Pressure swirl atomizer fitted at the center of the combustor has a 0.25 mm diameter orifice for injecting the kerosene fuel ($C_{12}H_{23}$) [12].

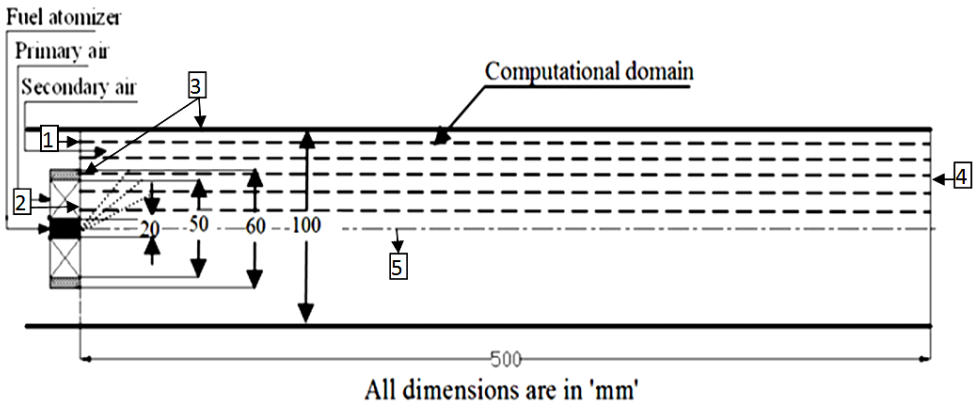

Surface Identity	Surface conditions	Boundary Conditions
1	Primary air entry	U_z=constant, $U_\theta = U_z \tan\theta$, U_r=0, T=T_{pr}, Species :air
2	Secondary air entry	U_z=constant, U_θ=0, U_r=0, T=T_{sec}, Species :air
3	Wall	No slip, Mixed thermal boundary condition with specified external heat transfer coefficient and emissivity. Impermeable wall for species.
4	Outlet	Outflow boundary conditions for variables (φ), $d\varphi/dz$=0
5	Axis	Symmetry boundary condition, $d\varphi/dr$=0

Figure 5.1 Physical model with boundary conditions

The two phase flow of spray combustion is modeled using the stochastic separated flow model with the Eulerian gas phase and Lagrangian droplet phase computations. In the gas phase, Favre averaged conservation equations of mass, momentum, energy and species concentration are solved. The turbulent transport in the gas phase is solved using the realizable k-ε model [143]. In addition, the conservation equations for the Favre averaged mixture fraction ($\tilde{\xi}$) and its variance ($\tilde{\xi}''^2$) are also solved for the requirement of the flamelet models. The gas phase

conservation equations are constituted with the inter-phase transport terms as sources, accounting the exchange between the two phases.

In the liquid phase, breakup of the injected liquid and the dispersion of the resultant droplets are accounted along with the evaluation of the inter-phase source terms till complete evaporation of the droplets. The injected spray from the atomizer with a particular cone angle is considered to break up following the linearized instability sheet atomization model (LISA) [37].

Radiation exchange in the gas phase is modeled using discrete ordinate (DO) model [144] considering the contributions of the participating gases and soot. The soot formation in the combustor is evaluated using the Brookes-Moss [98] soot model accounting suitable empirical constants for kerosene flame [145]. Acetylene (C_2H_2) is considered as the soot precursor species both for the nucleation and surface growth processes. However the relations between C_2H_2 mole fraction ($X_{C_2H_2}$) and mixture fraction (ξ) in kerosene flame (given in eq. 4.9a, 4.9b, 4.9c in chapter 4.3) is used to predicts the soot nucleation and surface growth a well in all the three combustion models. The model details and the governing equations for above models are given in chapter 3.4.

5.3 Experimental

In order to validate the predictions using different combustion models, experiments have been performed in a stainless steel combustor of the same geometry as considered in simulation. The experiments have been conducted in the model combustor, with a kerosene spray flame established with a pressure swirl atomizer placed at the centre of the combustor as shown in **Figure 5.2 (a)** and **(b)**. The primary and secondary air flow supplies to the combustor and the flow rates are measured by orifice meters. The fuel flow rate is measured using a calibrated rotameter. In order to measure the combustor wall temperature, eight thermocouples (K-type) are fitted with silicon heat sink compound close to the inner wall surface at an interval of 50 mm in the axial direction. A traversing thermocouple (K-type) near the exit plane measures the variation in exit gas temperature from the centreline to the wall. The radiation corrected data from thermocouple are used to plot the corresponding graphs.

Sample experiments also have been performed at our laboratory in a separate test rig to generate the spray data required for the model for the validation of combustion

model predictions. The spray data are obtained by conducting experiments in a spray test rig. The details and schematic of the spray test rig are given in literature [146]. In the test rig, kerosene is injected through the pressure swirl atomizer (Lechler (No. 212.085)) under consideration to generate sprays in open atmosphere. The injection pressure is measured by fitting a calibrated pressure gauge just before the nozzle and the corresponding volume flow rate is measured by collecting the liquid in a measuring flask over definite time. The coefficient of discharge of the nozzle is found out from the measured values of volume flow rate and injection pressure differential. The spray cone angles are measured by obtaining the spray images using a light sheet and a camera.

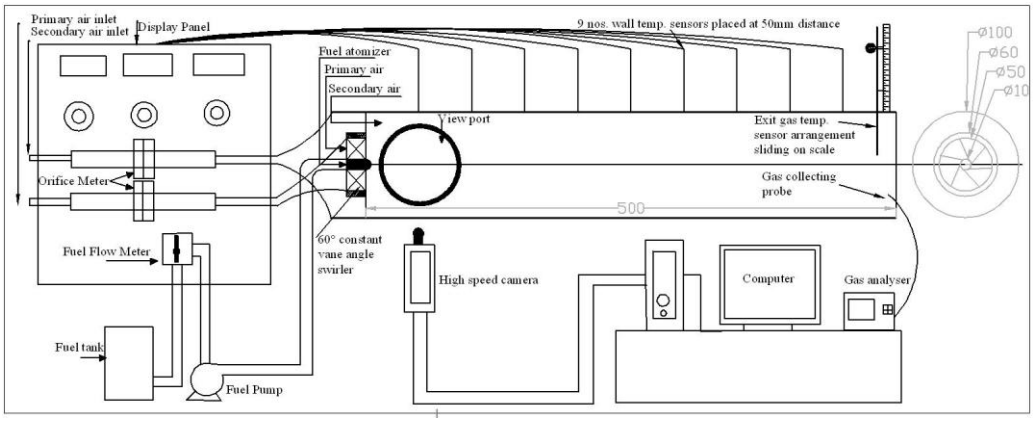

(a)

(b)

Figure 5.2 (a) Schematic of the experimental set up and (b) Picture of the experimental setup.

5.4 Operating and simulation conditions

The total air flow is split equally between the primary and secondary streams. The Reynolds number, corresponding to average axial velocity of air in the combustor and combustor diameter ($Re_D = 4\dot{m}_{air} / \pi D \mu$) is 26300, where $\dot{m}_{air}$ is the total mass flow rate of air (including primary and secondary), D is the combustor diameter and μ is the viscosity of air at inlet condition.

Plug flow velocity distributions of air have been considered for the axial velocity at the entry to the combustor, both for the primary and secondary air. In addition, tangential velocity is imparted to the primary air at inlet for the constant angle vane swirler. Both primary and secondary airs are at room temperature (300 K) at the inlet. The turbulent intensity (*TI*) and the length scale (*LS*) at inlet planes are set by using the relations given in equations 2.17 and 2.18.

No slip boundary condition is given on the wall with standard wall function for the turbulence calculation. A mixed (convection and radiation) boundary condition has been set to account the heat loss from the system to the atmosphere. A calculated value for heat transfer coefficient in between outer wall and atmosphere has been specified along with the emissivity for the wall surface material. Ambient temperature has been set at 300 K and the thickness of the wall is taken as 5 mm.The simulation in the combustor is run considering axi-symmetry and the symmetric boundary condition is given on the combustor axis.

The density in the gas phase is computed using the equation of state for ideal gas law. The specific heat of the component species are evaluated considering polynomial variation with temperature. The mixing laws have been adopted for finding the properties of the gas mixture. Both turbulent Prandtl number and turbulent Schmidt number are considered as one.

For the discrete phase simulation, injection pressure and spray cone angle are given as measured from the experiments with the atomizer under use. The liquid is injected as 20 diameter classes of droplets sprayed within an initial spray cone angle of 36^O. The dispersion angle of the spray is assumed to be 6^O. The details of operating and boundary conditions for the simulation are given in the **Table 5.1**.

Table 5.1 Operating parameters

Flow conditions	*Primary air*	*Secondary air*	*Others*
Mass flow rate (kg/s)	0.0124	0.018	-
Bulk velocity (m/s)	6.147	2.94	-
Temperature (K)	300	300	-
Swirl number	2.142	0.0	-
Air fuel ratio	-	-	110:1
Fuel flow rate (kg/s)			0.00036
Combustor pressure (atm)	-	-	1.0
Turbulent intensity	4%	4%	-
Length Scale	0.07D	0.07D	-
Liquid fuel temperature (K)	-	-	300
Spray cone angle (deg)	-	-	36
Injection Pressure (bar)	-	-	5
Droplet class	-	-	20

The variables have been defined in the domain using a staggered grid arrangement. The discretization of the governing equations has been done using power law scheme while, the radiation model equation is discretized using second order upwinding scheme. A pressure based solver is used in the simulation and the pressure-velocity coupling is solved with the SIMPLE algorithm.

5.5 Results and discussion

A grid independence study has been done to choose the mesh configuration for the numerical simulation. In the grid independence study the simulation was run with three different mesh configurations having 100×50, 200×100, and 400×200 grids in the axial and radial directions, respectively. The simulations for grid independence have been done considering the laminar flamelet model of combustion. The wall temperature variations for three mesh configurations, plotted in **Figure 5.3**, show that refining the mesh from 100×50 to 200×100 alters the wall temperature, and further refining to 400×200 makes only a very little difference in the temperature values. We adopted the 400×200 mesh configuration for the simulations with the other two combustion models as well in order to have sufficient resolutions of the variables.

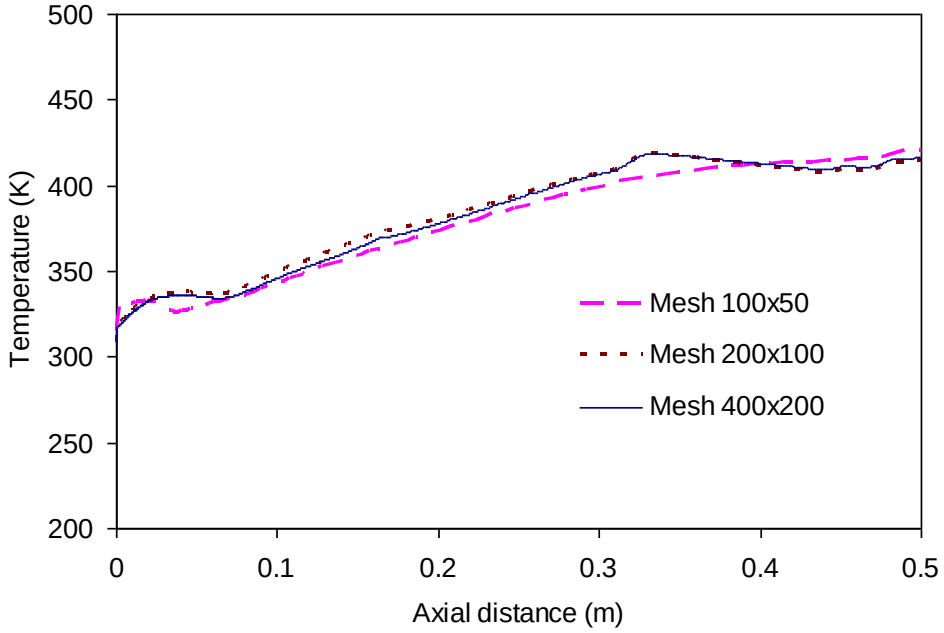

Figure 5.3 Wall temperature variations in the combustor with different mesh configurations

The results using the eddy dissipation model is presented in **Figure 5.4** where, the top half describes the distribution of (ε/k) while, the bottom half shows the distribution of rate of reaction in the combustor. In the combustor flow, ε/k represents the inverse of the turbulent time scale and indicates the turbulent mixing rate. It is already stated earlier that in the eddy dissipation combustion model, the rate of reaction is computed using the mixing rate. The top half of the figure shows that the high mixing rate zones are observed adjacent to the injector and in the turbulent shear layers of flows issued from the primary and secondary air jets. The high mixing rate on the axis and adjacent to the atomizer is attributed to the central recirculation zone formed on the axis due to the swirling entry of the primary air. However, based on the availability of the fuel vapour evaporated from the injected spray, the rate of reaction has high value only in the shear layer between the primary air jet and the recirculation core on the axis (as seen in the bottom half). The local mixing rate in the shear layer influence the rate of reaction and the thermal energy released is transported to the other parts of the combustor.

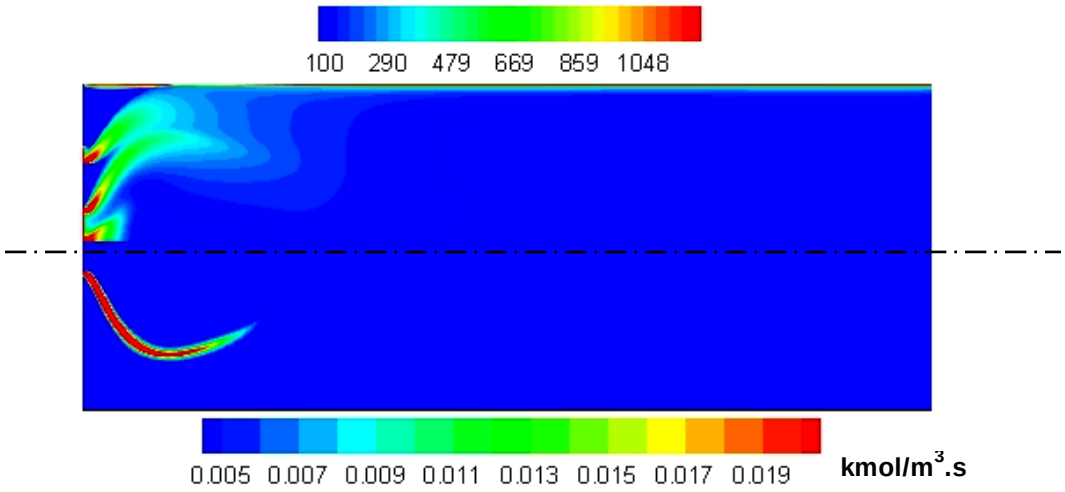

Figure 5.4 Variation of ε/k (top half) and reaction rate (bottom half) in the combustor predicted using the eddy dissipation model

Unlike the eddy dissipation model, the laminar flamelet model considers a detailed chemical mechanism with several intermediate species in computing the reacting flow. In **Figure 5.5**, the top half shows the variation of the mean mixture fraction and the bottom half shows the mean scalar dissipation rate in the combustor evaluated using the laminar flamelet model. The mean scalar dissipation rate is computed from the variance of the mean mixture fraction [103] as given in **Equation. 3.34**. The stoichiometric mixture fraction (χ_{st}) of kerosene ($C_{12}H_{23}$) is 0.064. Mixture fraction higher than χ_{st} represents the rich zone in the combustor while, the mixture fraction less than χ_{st} shows the lean zone. The rich zone is observed close to the combustor inlet as the fuel is evaporated from the spray. The mixture gets leaner with the distribution of fuel vapour over a larger volume and mixing with the oxidizer. On the other hand, the scalar dissipation rate in the combustor represents the rate of transport influenced by turbulence and governed by the mixing rate, ε/k, and the variance of the mixture fraction. The bottom half of **Figure 5.5** shows that the region of high scalar dissipation rate also occurs close to the inlet and adjacent to the central axis, where the central recirculation zone exists and the primary air shear layer occurs. Comparing, the distributions of the mean mixture fraction and the mean scalar dissipation rate, it can be clearly observed that the high scalar dissipation exists in the rich zone of the combustor, where the mixture fraction is much above the stoichiometric mixture fraction. The results suggest that in the region of mixture

fraction lower than 0.096, the scalar dissipation rate is very low in the combustor. On the other hand, in the zone where the mixture fraction increases from 0.096 to 0.3, the scalar dissipation rate sharply increases to 12 and beyond. When the scalar dissipation rate is high the flame is increasingly strained and departure from chemical equilibrium occurs. An excessively high scalar dissipation rate may even extinguish the flame. Rich fuel air mixture also causes departure from equilibrium due to the low temperature occurring in the flame. These observations guide towards a constraint condition based on the equivalence ratio to describe the departure from equilibrium in the flame.

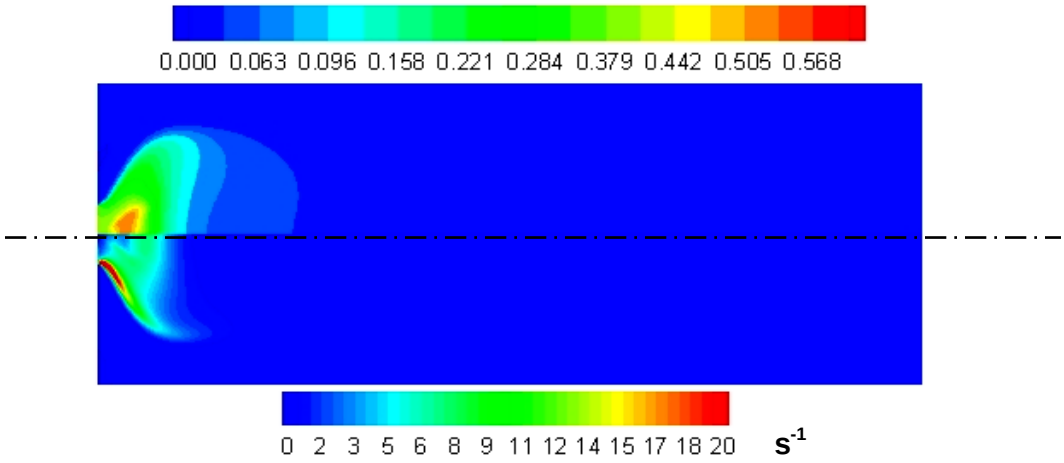

Figure 5. 5 Variation of mean mixture fraction (top half) and mean scalar dissipation rate (bottom half) in the combustor predicted using the laminar flamelet model

The choice of the rich limit of equivalence ratio, as the constrained condition, is further corroborated by comparing the mean temperature as a function of mean mixture fraction for different scalar dissipation rates. **Figure 5.6** shows the variation of mean temperature against mean mixture fraction at different scalar dissipation rates by solving in a counter flow, laminar, non-premixed flame and accounting the effect of turbulence with an assumed β-PDF distribution. A higher peak temperature and a narrower high temperature zone are observed at lower scalar dissipation rate. As the scalar dissipation rate increases, the peak temperature decreases and the high temperature zone spreads out due to increased rate of transport. Finally, with scalar dissipation rate above 13 s^{-1} the transport is so fast that the flame extinguishes. An additional variation of mean temperature against mean mixture fraction, shown in

Figure. 5.6 is for the constrained equilibrium flamelet model. This variation is achieved by setting the constrained condition, in terms of rich flammability limit. Following the observations shown in **Figure 5.5**, the constraint is set at equivalence ratio of 1.5 (corresponding to mixture fraction 0f 0.096). The distributions in the **Figure 5.6** show that the distribution for the equilibrium case agrees well with the distribution corresponding to the lowest scalar dissipation rate till a mixture fraction of 0.096. However, the imposition of the constrained condition changes the distribution pattern of the equilibrium case completely beyond the mixture fraction of 0.096. Due to the set constrained condition, the temperature variation with mixture fraction for the equilibrium case now agrees with the distributions of the high scalar dissipation rate cases. Therefore, considering the patterns of mixture fraction and scalar dissipation rate distributions in the combustor (as shown in **Figure 5.5**), it is expected that constrained equilibrium flamelet model will predict well in the entire combustor zone.

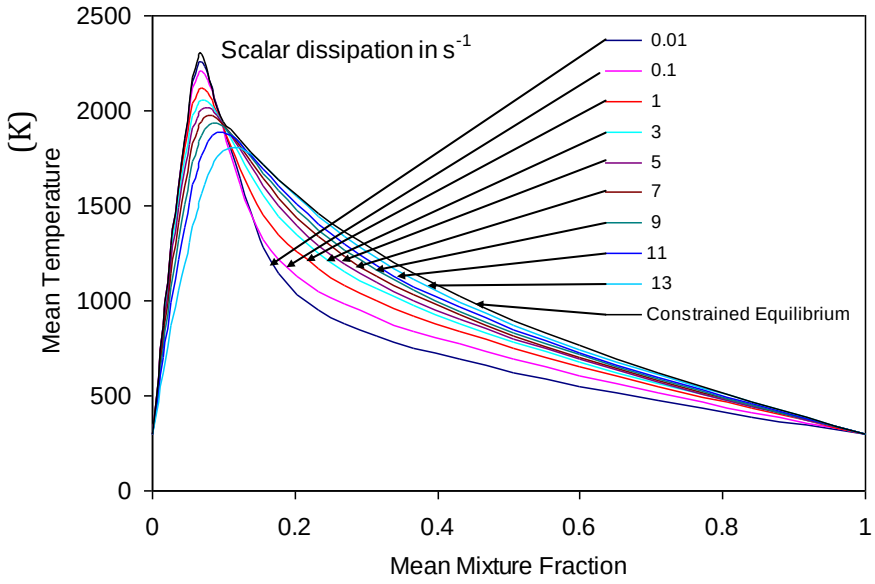

Figure 5.6 Variation of mean temperature with mean mixture fraction at different scalar dissipation rate (s^{-1}) from the laminar flamelet model and using the constrained equilibrium model with constraint set at equivalence ratio of 1.5

Figure 5.7 a-c shows the predicted temperature contours in the combustor, using the three combustion models, as a result of the burning of kerosene spray. The high temperature flame zone is observed to exist a little ahead of the inlet plane around the central axis. Within the flame contour a low temperature region exists, particularly

near the injector, where the evaporation of the injected fuel takes place. It is seen from the figures that the temperature contours predicted by the eddy dissipation model are much different from those predicted by the other two combustion models. The eddy dissipation model predicts a much higher peak temperature (2100K) in comparison to the laminar flamelet model (1770K) and constrained equilibrium flamelet model (1809K). Moreover, the peak temperature predicted by the eddy dissipation model is located further away from the inlet and is spread over a wider zone of the combustor. This shows that even though the combustion is mixing dominated, the effect of chemistry cannot be completely ruled out in the prediction of the combustion of fuel. On the other hand, the temperature contours predicted by the laminar flamelet model and the constrained equilibrium flamelet model are fairly close to each other. Thus the chosen constrained condition effectively captures the non-equilibrium effects in the flamelets and predicts the temperature distribution within the combustor quite well.

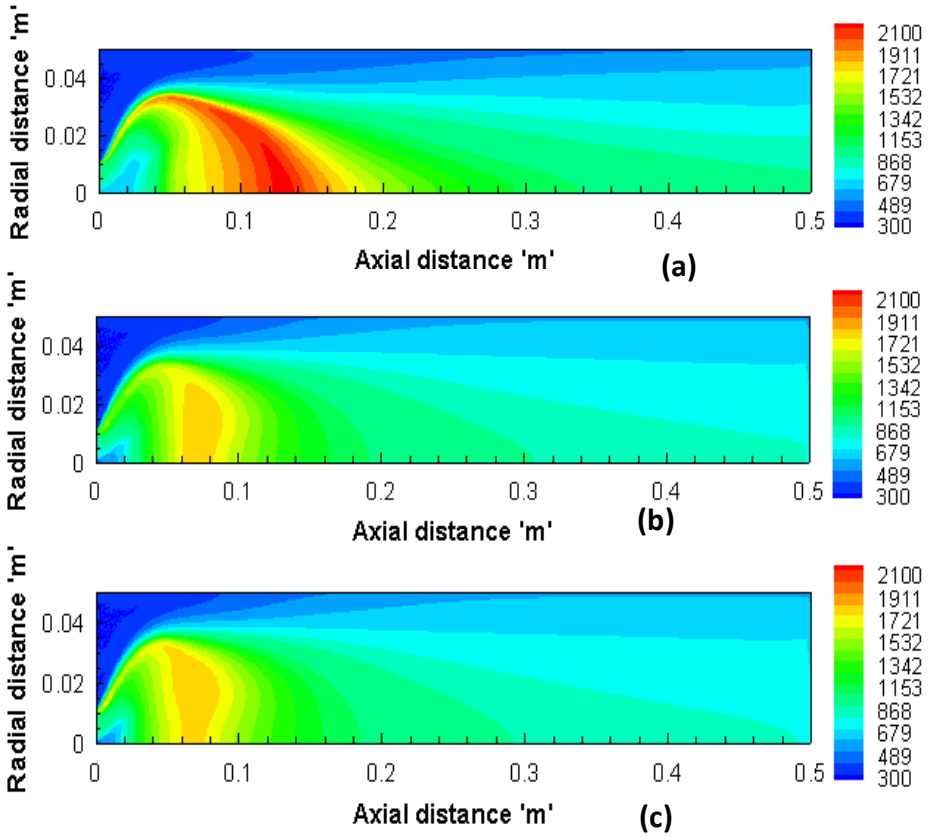

Figure 5.7 Temperature (K) distributions in the combustor using (a) Eddy Dissipation Model, (b) Laminar Flamelet Model, (c) Constrained Equilibrium Model

The quantitative deviation in the wall and exit gas temperature predictions from the different combustion models are shown in **Figures 5.8a and 5.8b**, respectively. The experimental data have also been plotted in the figures for validation. The prediction from the constrained equilibrium flamelet model and the laminar flamelet model differs only a little both for the wall temperature as well as for the exit gas temperature. The maximum percentage deviation in the wall temperature between the two flamelet predictions is 12% (which occurs near the inlet plane), though for most part of the wall the deviation lies well within 10%. The deviation in the exit gas temperature predicted by the two flamelet models remains much less, with the maximum deviation less than 3.5%. Moreover, the flamelet predictions agree quite well with the experimental data, particularly for the exit gas temperatures. The relatively larger deviation from the experimental data for the wall temperature close to the inlet may be attributed to the adopted axisymmetric model (which cannot account the effect of the swirler geometry in practice) and the assumed inlet boundary condition. The eddy dissipation model predicts much higher wall temperature near the inlet. It also predicts a higher exit gas temperature close to the axis. The wall heat transfer in the combustor occurs due to radiations and convection. The heating of the wall close to the inlet can be mostly attributed to radiation from the flame. The cold secondary air entering the combustor adjoining the outer wall results in cooling of the combustor wall. In case of eddy dissipation model the maximum temperature predicted in the flame is much higher. This results in a greater radiative heating of the wall when eddy dissipation model is used. The concentration of soot predicted in the flame will also contribute greatly towards the radiative heating of the wall and therefore needs attention. The higher flame temperature, predicted by the eddy dissipation model, results in the higher gas temperature near the combustor exit as well. The validation shows that both the flamelet models work satisfactorily in predicting the spray flame temperature. Therefore, in absence of a reliable chemical mechanism even the constrained equilibrium flamelet model can be used for describing the flame temperature satisfactorily.

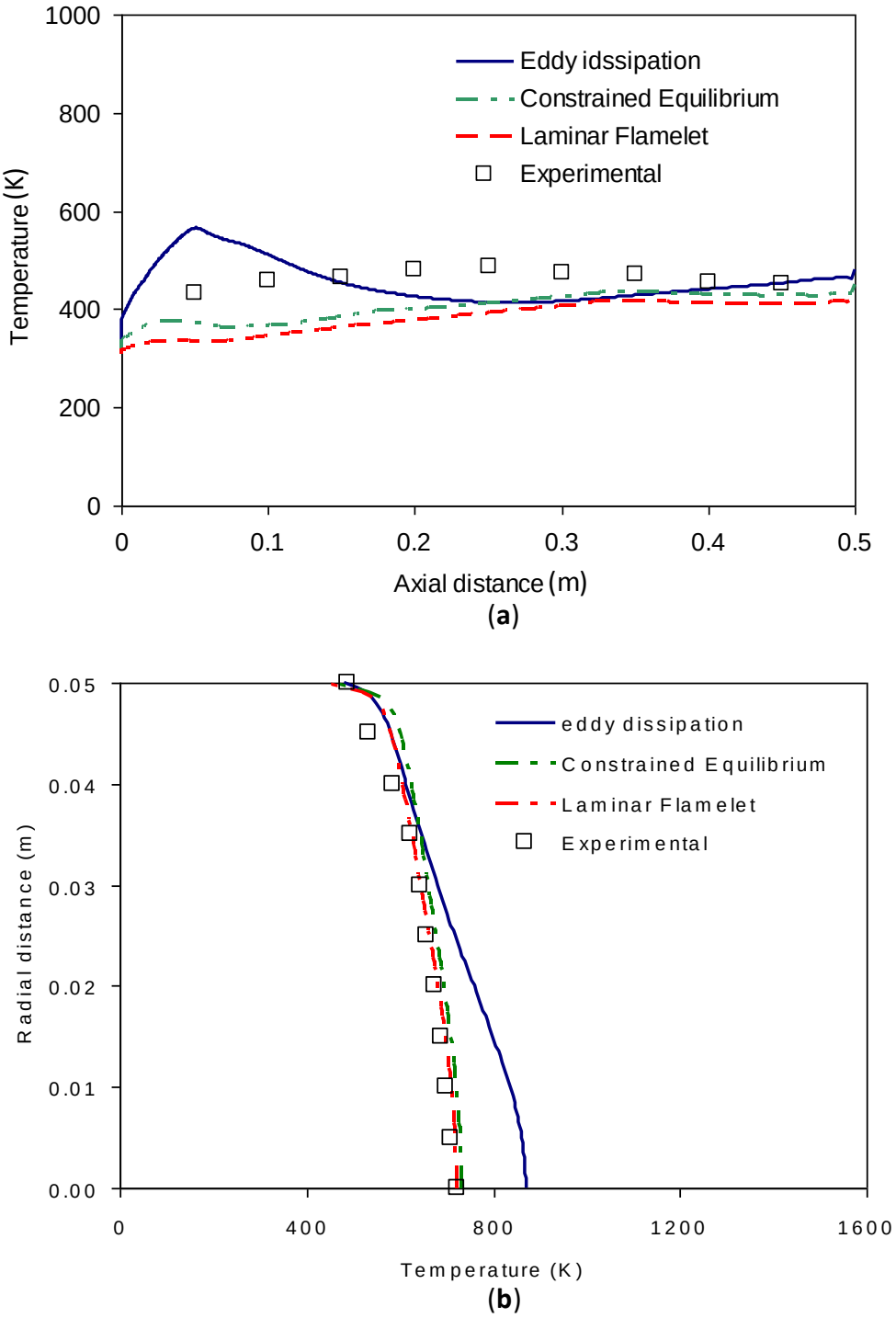

Figure 5.8 (a) Wall Temperature Distribution in the combustor using different combustion models and from experiments (b) Exit gas temperature distribution using different combustion models and from experiments

The prediction of soot formation in the kerosene spray flame of the present work with the different combustion models has been compared taking into account the

processes of nucleation, surface growth, coagulation and oxidation. **Figures 5.9 a-c** show the contours of soot volume fraction in the combustor as predicted by the three combustion models. It is clearly evident that the eddy dissipation model predicts much higher soot in comparison to the flamelet models. This is due to the prediction of higher temperature in the eddy dissipation model. As both the soot nucleation and surface growth are chemical processes, their rates are exponential functions of temperature. Therefore, at higher flame zone temperature, the soot nucleation and growth rate increases to result higher soot concentration in the flame. However, the soot predictions from the two flamelet models are close to each other. Both the models solve the mixture fraction equation with the same boundary conditions and the temperatures predicted by the two models have been shown to agree well. Therefore, the soot distributions predicted by the constrained equilibrium flamelet model and the laminar flamelet model are quite similar.

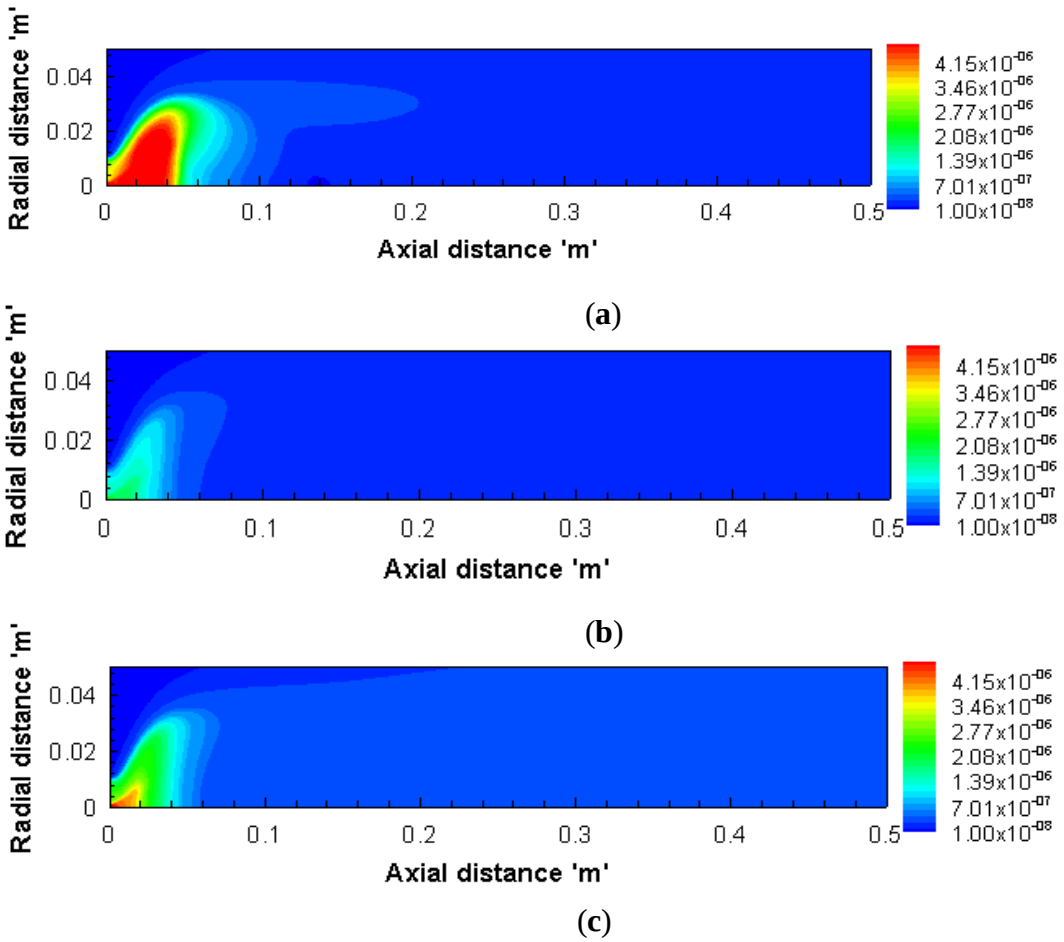

Figure 5.9 Soot Volume Fraction distributions in the combustor using (a) Eddy Dissipation Model, (b) Laminar Flamelet Model, (c) Constrained Equilibrium Model

The soot distributions predicted by the models further emphasize the cause of higher wall temperature prediction by the eddy dissipation model near the inlet zone of the combustor. Soot particles, having very high emissivity, contribute largely towards radiative heat transfer from the flame. As the eddy dissipation model of combustion predicts higher soot in the flame zone, the radiative heating of the combustor wall is higher with this model.

5.6 Conclusion

The effect of different combustion models on the predictions from numerical simulation in a spray combustor has been analyzed. The eddy dissipation model, laminar flamelet model using a detailed chemical reaction mechanism and constrained equilibrium flamelet model have been considered as combustion models. A proper constraint condition for the constrained equilibrium flamelet model is chosen by judiciously comparing the temperature predictions in the laminar flamelet and accounting the mixture fraction and scalar dissipation rate within the combustor. It has been found that the flamelet models predict wall and exit gas temperatures closely which also agree well to the measure values. On the other hand, the temperatures predicted by eddy dissipation model deviate from the measurements. The eddy dissipation model also predicts much higher flame temperature and higher soot concentrations in comparison to the flamelet models. These results clearly indicate the influence of chemistry in describing the highly turbulent non-premixed spray flame in the combustor. The relatively good agreements of temperature and soot concentrations between the predictions of the two flamelet models illustrate that with a proper choice of constraint the non-equilibrium conditions in the flames due to straining effect can be suitably addressed. This method can be useful to simulate flames in the combustor with fuels of unknown chemical mechanism.

Chapter 6

Effect of air flow distribution on soot and radiative heat transfer

6.1 Introduction

Gas turbine combustors operate with very high overall air-fuel ratio. The air flow supplied to the combustor should be distributed in order to maintain proper local equivalence ratio inside the combustor. Normally in a gas turbine combustor, the total air supplied from the compressor is admitted at different points. Out of them, the primary air is used purely for oxidizing the fuel, secondary air completes the combustion of left over species and the dilution air is used to maintain the gas temperature flowing to turbine within the metallurgical limit. Another function of the secondary air is to cool the combustor wall continuously.

In this chapter the effect of air flow distribution on various thermo physical and chemical parameters during combustion has been studied with the help of a 3-D combustor geometry (**Figure 6.1**). The total mass flow rate of air ($\dot{m}_{air}$) into the combustor is set at 0.04 kg/s, which is entering the combustor at 300 K. The Reynolds number ($Re = 4\dot{m}_{air}/\pi D \mu$) based on the air flow inlet conditions and combustor diameter is 26300. The air flow is split between the primary and secondary streams at the entry to the combustor. Three different air flow splits, with primary: secondary as 30:70, 40:60 and 50:50 have been considered in the analysis. A constant angle (60^{O}) vane swirler is fitted at the entry of the primary stream to the combustor (**Figure 6.1**). The inlet plane of computation is considered at 40 mm upstream to the swirler plane. The fuel, at 300 K temperature, is injected through a 0.25 mm diameter orifice of the pressure swirl atomizer at a rate of 0.00036 kg/s in all the cases. The spray cone angle

and the injection pressure differential corresponding to the liquid flow rate through the atomizer are experimentally obtained to feed to the model.

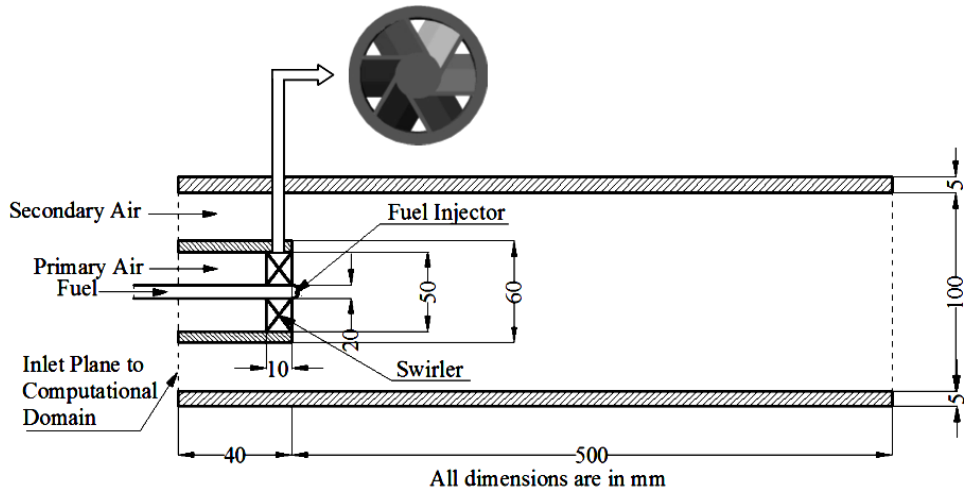

Figure 6.1 Physical geometry of the combustor under study

The plug flow velocity boundary condition is considered at the inlet planes of both primary and secondary streams, depending on their respective flow rates. A 4% turbulent kinetic energy and a turbulent length scale of 0.007 m are set at the inlet boundaries. The length scale has been chosen based on the maximum value of the mixing length in the combustor duct. Atmospheric pressure boundary condition is considered at the outlet plane of the combustor. A mixed heat transfer boundary condition is given on the peripheral wall of the combustor considering stainless steel body (5 mm thick) and a convective heat transfer coefficient on the outside. However, the injector and the other solid walls are considered as adiabatic.

However the entire simulation of combustion process in this current work has been performed with laminar flamelet model that has been described in chapter 3.4.2.1.

6.2 Grid independence test and validation of numerical model

The experimental details have already been discussed in chapter 5.3. The validation of soot model also explained in chapter 4.3. However the validation of numerical model for 3-D combustor is required to be established. Subsequent to the selection of the soot model parameters, we have computed the spray combustion of kerosene fuel in the model combustor considering the soot formation in flame. Experiments have been performed in the model combustor under the same flow and spray conditions as

in computation and with one air flow split (50:50 between primary and secondary). Validation of the model predictions has been made by comparing the predicted temperature distributions along the wall and across the exit plane against the experimental values. A grid independence test is first done by refining the grid over the computational domain and by observing the variation in predicted temperatures along the wall (**Figure 6.2a**) and over the exit plane (**Figure 6.2b**). An unstructured, quadrilateral mesh configuration is chosen with 254,720, 324,394 and 462,875 elements in the domain. It is found from the figures that with the first refinement of the grid (from 254,720 to 324,394 elements) the maximum changes in the wall temperature and the exit gas temperature are found to be 5.6% and 8.2%, respectively. While with further refinement (from 324,394 to 462,875 elements), the above two peak variations come down to 2.2% and 1.2%, respectively. Considering these, we have finally chosen the grid configuration with 324,394 elements in the mesh for further computation.

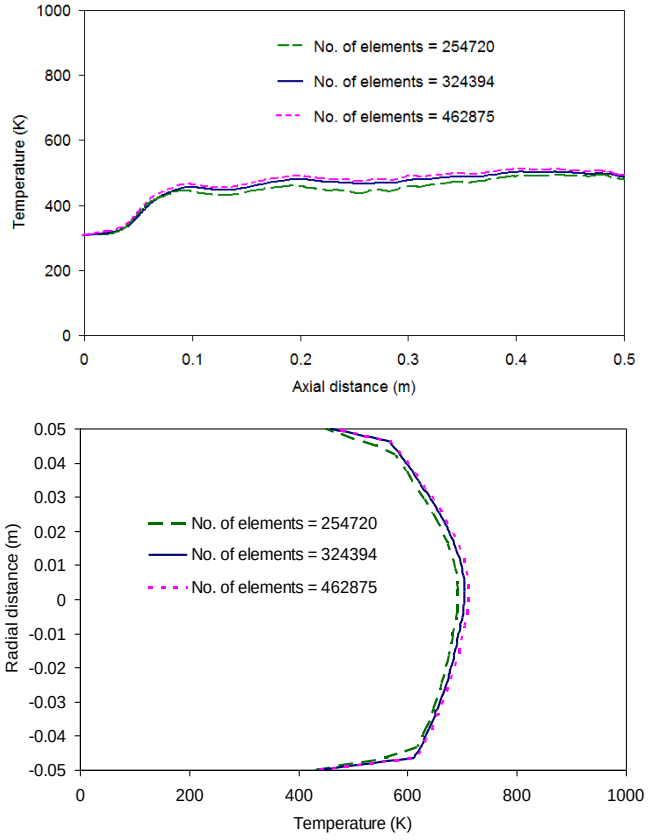

Figure 6.2 Comparison of predicted values of (a) wall temperature along the length of the combustor, (b) exit gas temperature across the radial direction for three different grid configurations.

The variations in temperature along the combustor wall (**Figure 6.3a**) and in the exit gas (**Figure 6.3b**) agree quite well with the measured values. A discrepancy in the temperature prediction is noticed on the wall around the flame zone, and may be attributed to the variation in radiative heat transfer from the flame. The predicted temperature distribution in the exhaust gas agrees very well with the experiments over the entire cross-section of the combustor. Overall considering all the compared variations of temperature and concentration it can be concluded that the adopted spray combustion model predicts the parameters reasonably well in the combustor.

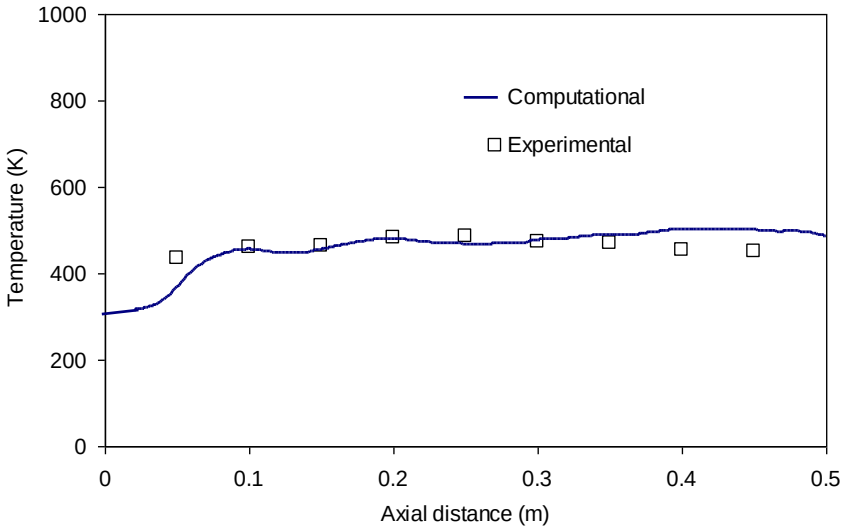

(a)

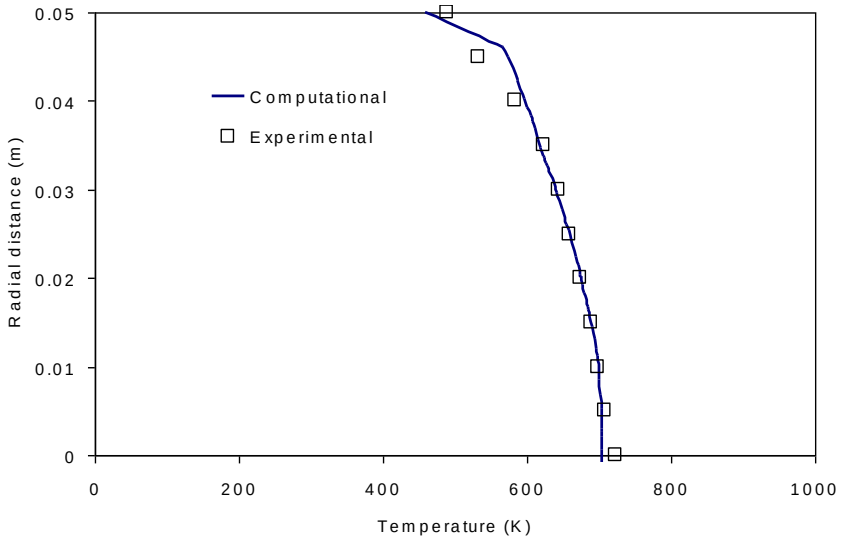

(b)

Figure 6.3 Comparison of predicted and measured values of (a) wall temperature along the length of the combustor, (b) exit gas temperature across the radial direction.

6.3 Velocity and temperature distribution in the combustor

We have applied the spray combustion model to predict results with different air flow splits between the primary and secondary streams. The total air and fuel flow rates are maintained same while, three different primary air to secondary air flow ratios (30:70, 40:60 and 50:50) have been considered. As the primary air fraction is increased the stoichiometry in the flame region becomes leaner. This alters the structure of the flame and the temperature distributions in the flame region. However, the corresponding reduction in the secondary air flow rate reduces the momentum in the flow adjacent to the combustor wall, affecting the flow mixing and the convective cooling of the combustor wall.

Figure 6.4(a)-(c) shows the mean temperature distributions in the vertical plane passing through the axis of the combustor for the three different air flow splits with superimposing velocity vectors. The axial distance in the figures has been measured from the plane of the swirler/atomizer, where x=0 is considered. The highest temperature zones in the figures, adjacent to the fuel injector, depict the flame regions. It is clearly evident from the figures that the flame becomes shorter in size with the increase in the primary air. The primary air is admitted in the combustor with a swirling motion. When the primary air flow rate increases the tangential momentum in the inlet stream also increases, and it generates a stronger central recirculation zone. Under the influence of the strong swirling motion, the mixing process intensifies in the flame zone. The kinetics of the reactions is considered to be very fast and therefore the overall combustion rate is controlled by the rates of physical processes. At higher primary air flow, the increased rates of the physical processes, like vaporization and mixing, increase the overall reaction rate in the combustor. As a result, the flame becomes shorter with increase in the primary air. When the primary air fraction is 50% of the total flow rate, the central recirculation bubble is so strong that it breaks the flame bubble on the axis and the highest temperature flame zone is confined within an annulus close to the inlet (refer **Figure 6.4(c)**). The flame is short and intense in this case due to the increased rates of the physical processes. All the temperature contours further show that there is only a little deviation from axi-

symmetry within the combustor. A closer look reveals that the deviation somewhat increases with the increase in primary air fraction in the combustor.

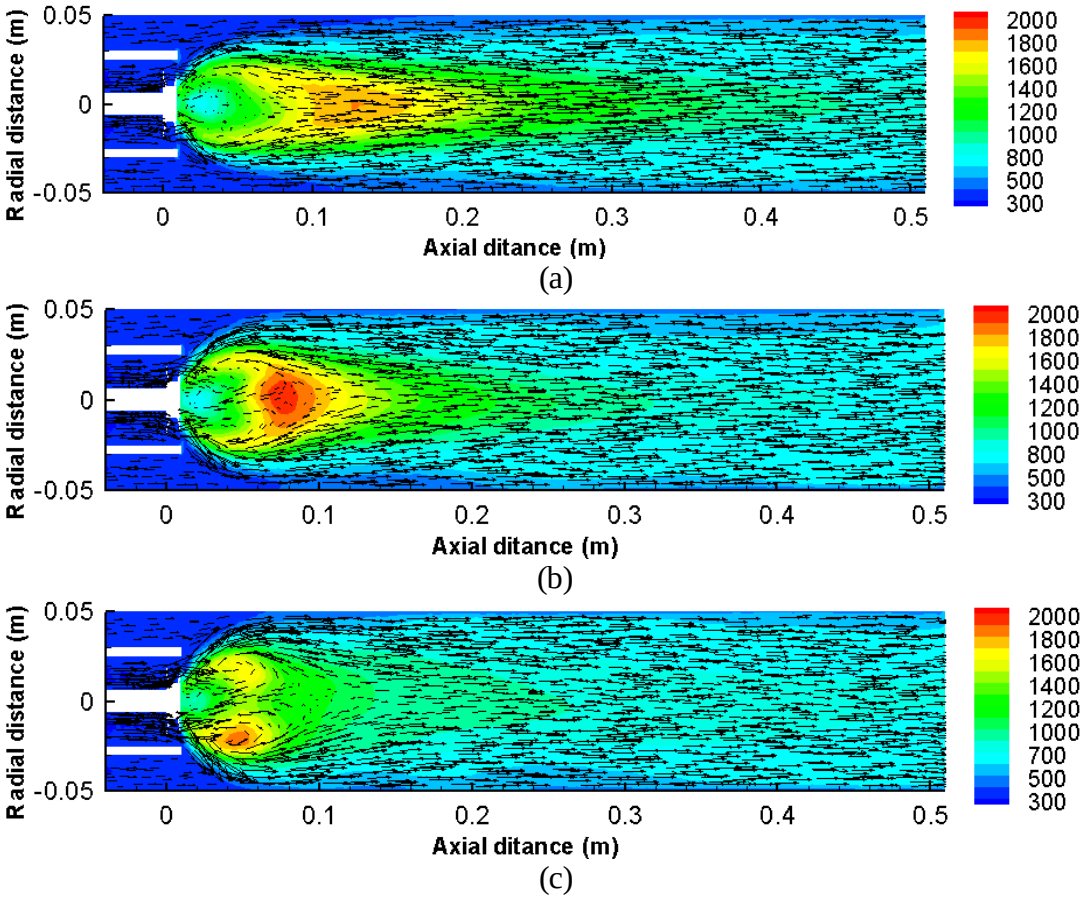

Figure 6.4 Velocity vector and Temperature distributions across the vertical plane through the combustor axis for three different air flow splits between primary and secondary streams (a) 30:70, (b) 40:60 and (c) 50:50.

Figure 6.5 compares the centreline temperature variations in the combustor for the three different air flow splits. It is seen that in all the cases, the temperature at the plane of the atomizer (x=0) is somewhat high. It first decreases over a very short length in the downstream direction and then increases to reach a peak value. Subsequently, the temperature decreases again till the combustor exit plane is reached. The temperature on the atomizer surface is high because of the incident radiation from the flame. The peak centreline temperature is the maximum for the 40:60 flow split case, though in the 30:70 flow split case the maximum temperature is reached at a further downstream location. In case of 50:50 air flow split, the maximum centreline temperature is much lower and occurs closer to the inlet plane. This variation in the centreline distributions can be clearly explained from the

respective temperature contour plots. For the 30:70 and 40:60 air flow splits, the maximum temperature zones are located on the centreline. On the other hand, in the 50:50 case, the maximum temperature zone occurs in an annulus, which is away from the centre, and the peak centreline temperature is much less.

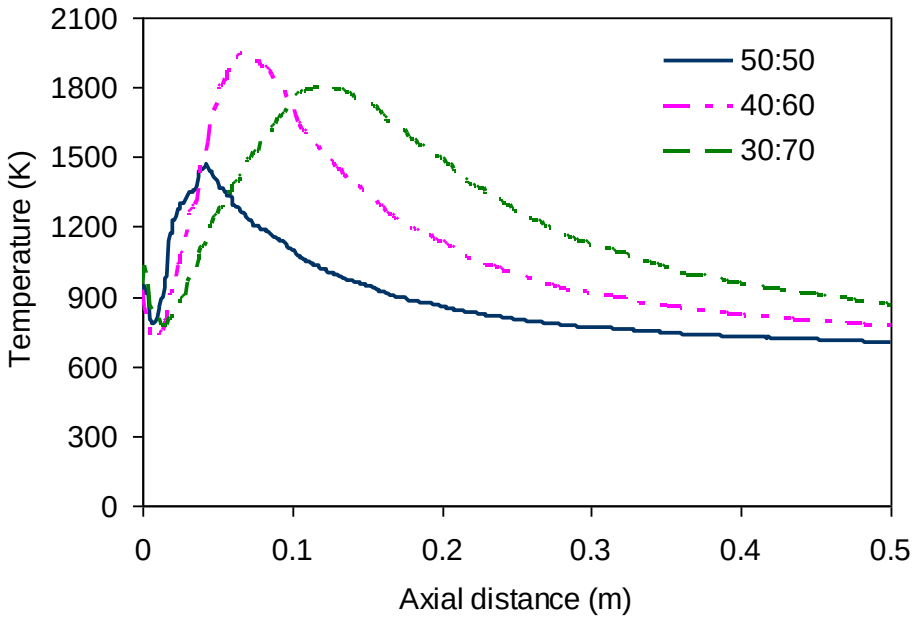

Figure 6.5 Variation of centreline temperature along the length of the combustor for different air flow splits between primary and secondary streams.

The variation in gas temperature at the combustor exit often has significance. In case of gas turbine, the exit gas temperature distribution depicts the combustor pattern factor. A low pattern factor, signifying more uniform exit gas temperature, is desirable for the health of the turbine. **Figure 6.6** shows the radial variation of the gas temperature at the exit to the combustor for the three different air flow splits. More uniform temperature variation is obtained when the air flow split is 50:50. As the primary air fraction is less, the peak temperature at the exit plane, occurring at the axis of the combustor, increases and the non-uniformity in the temperature distribution becomes more. This is because of the fact that in the case of 30:70 air flow split, the flame is longer and the maximum temperature in the combustor occurs closer to the exit plane. Therefore, the distance available to transport the energy in the lateral direction becomes considerably shorter. As a result, greater non-uniformity in the temperature distribution prevails at the exit plane. When the primary air fraction increases to 40% of the total air flow, the flame shortens in length and the maximum

temperature on the centreline occurs earlier along the combustor. The temperature variation flattens at the exit due to increased transport of energy in the radial direction. In the third case of 50% primary air, the maximum temperature is reached even earlier and at an off-axis location. Therefore, not only the axial length available for energy transport is more but also the radial distance over which energy has to be transported becomes less. As a result, the most uniform exit temperature distribution among the three cases is obtained with the 50:50 air flow split.

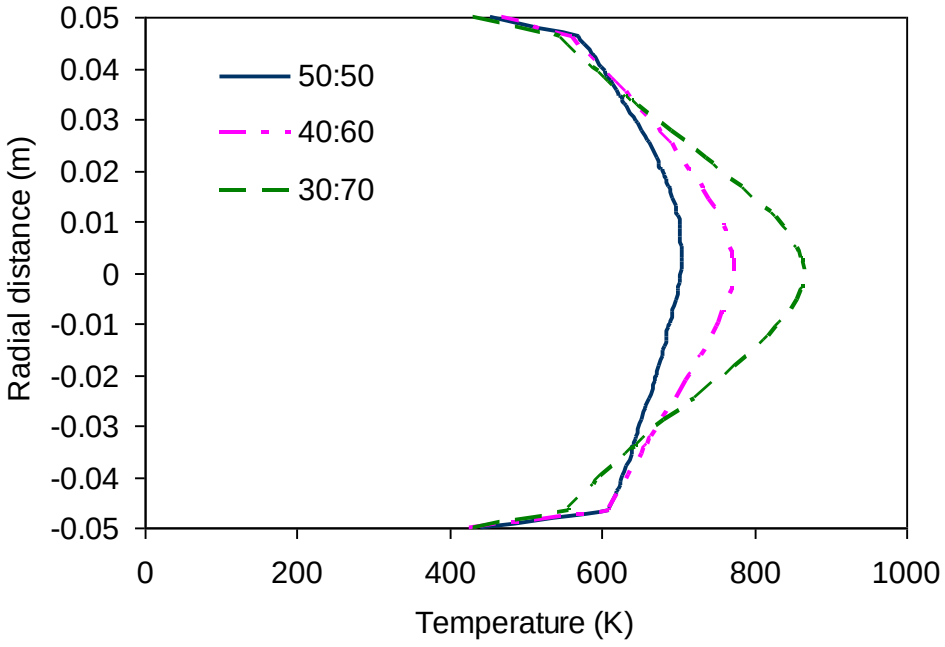

Figure 6.6 Variation of exit gas temperature from the combustor at three different air flow splits between primary and secondary streams.

6.4 Soot distribution in the combustor

The soot distributions in the combustor are plotted in **Figures 6.7(a)-(c)** for the three different air flow splits. The soot laden zone is prolonged and the peak soot volume fraction is more when the primary air fraction is less. This is due to the fact that with the lower primary air, the soot precursor concentration in the flame region increases. The higher precursor concentration along with the extended high temperature zone results in increased formation of soot over the combustor. It is further to be noted from the soot distribution patterns that, under all the three cases, the maximum soot volume fraction occurs on the centreline of the combustor.

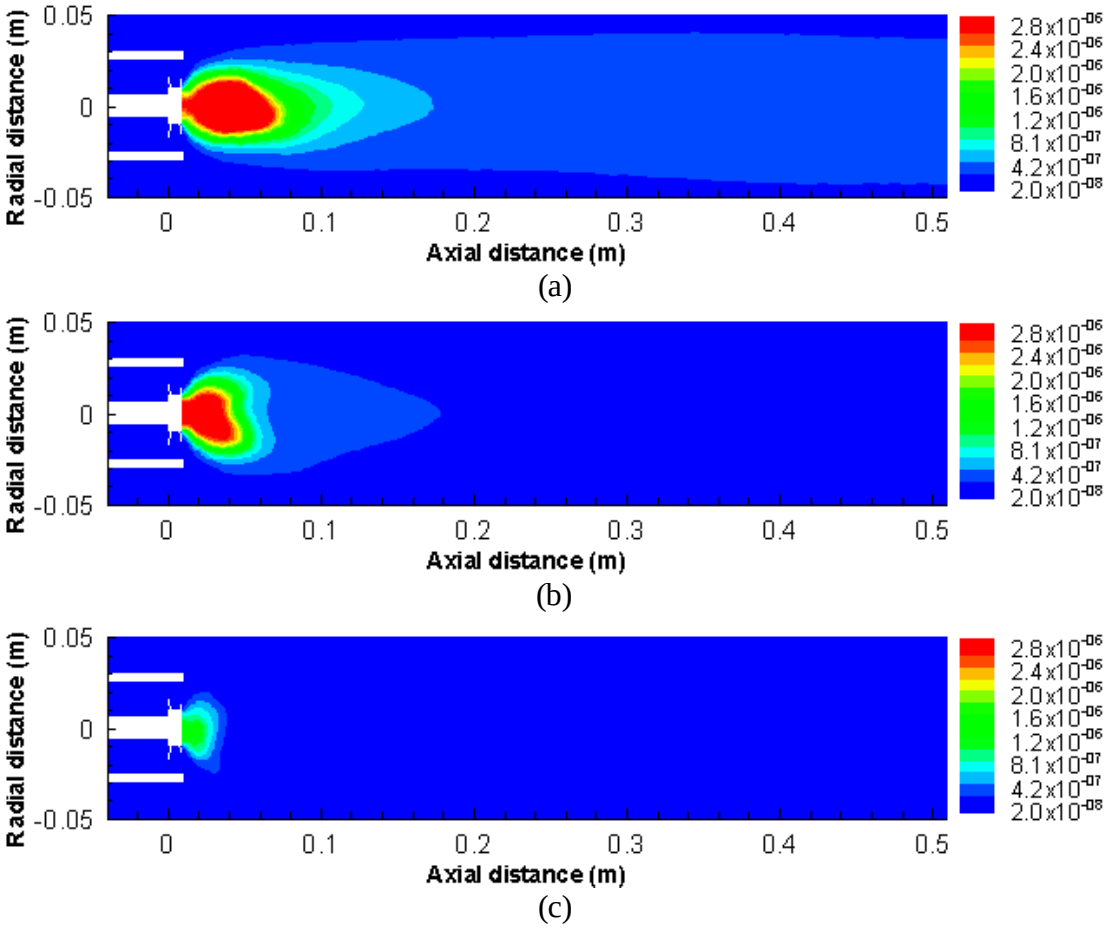

Figure 6.7 Soot volume fraction distributions across the vertical plane through the combustor axis for three different air flow splits between primary and secondary streams (a) 30:70, (b) 40:60 and (c) 50:50.

Figure 6.8 shows the variation of soot volume fraction on the centreline of the combustor for three different air flow splits. The peak soot volume fraction on the centreline is about 3 times higher in the 30:70 split case and more than 1.1 times higher in the 40:60 split case, compared to the 50:50 split case. Furthermore, it is seen from the soot contours that the concentration of soot near the fuel injector (x=0) remains quite high. This results in the deposition of considerable soot on the atomizer body after continuous operation, which is also evident in the experiments. The higher soot volume fraction near the atomizer with lower primary air results in faster build up of soot on the atomizer surface. When the soot build up becomes large, the atomization quality of the fuel suffers and the combustion gets affected.

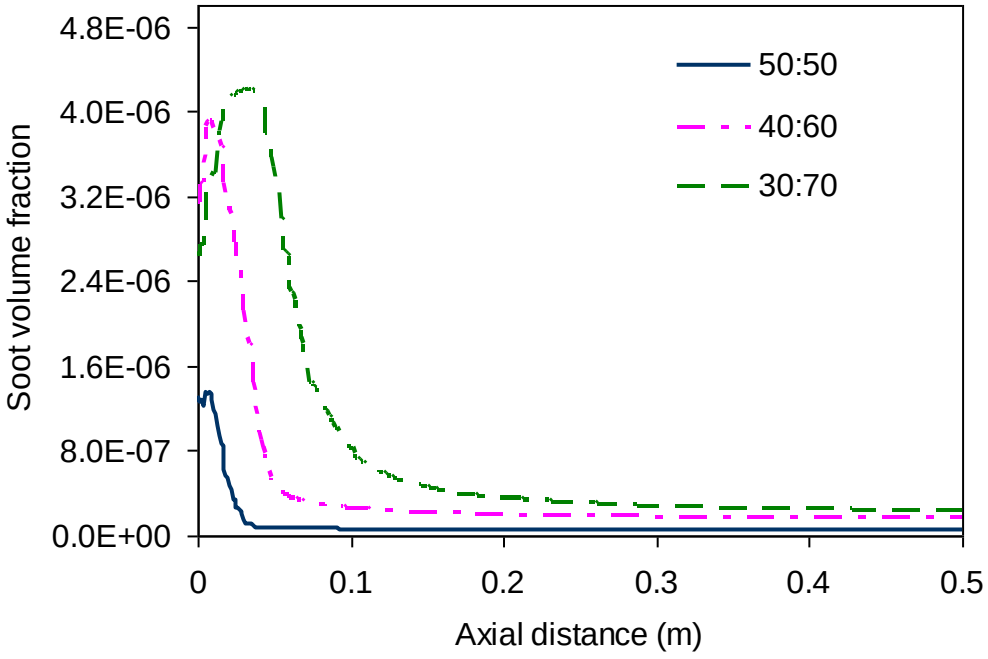

Figure 6.8 Variation of soot volume fraction along the combustor centreline for three different air flow splits between primary and secondary streams.

6.5 Temperature and incident radiative heat flux on combustor wall and fuel injector

The soot laden gas at high temperature causes increased radiation from the flame zone. The concentration of soot in the flame zone is dependent on the quantity of primary air supplied to the combustor. On the other hand, the secondary air, which enters along the outer wall of the combustor, helps to keep the wall surface cool. Therefore, the split between the primary and secondary air flow into the combustor will have an effect on the combustor wall and fuel injector surface temperatures.

This is evident in **Figure 6.9(a),** which plots the variation of incident radiative heat flux on the combustor peripheral wall for the three different air flow splits. Taking into account that there is not much deviation from symmetry in the temperature distribution, the plot has been made only along a line in the axial direction. The corresponding wall surface temperatures are plotted in **Figure 6.9 (b)**. It is clearly evident from **Figure 6.9(a)** that the highest radiative flux on the wall is incident around the flame close to the inlet to the combustor. This is caused by the high temperature of the flame and the high luminous radiation from the soot present in the flame zone. At the downstream location, the radiative flux on the wall is mostly

from the participating gases in the flow. The maximum incident heat flux due to radiation on the peripheral wall is achieved when the primary air flow is 30% of the total air flow. The soot volume fraction in the flame is much higher in this case, which is the prime reason of the increased radiative flux. The maximum incident radiation decreases by more than 50% when the primary air fraction is increased to 50% of the total flow. However, the peripheral wall of the combustor is cooled convectively by the flow of secondary air adjacent to the wall. The secondary air enters the combustor co-axially with the primary air flow and grazes along the wall, while exchanging energy with the high temperature core as well as with the combustor wall. When the primary air fraction is more, the fraction of the secondary air is less and it gives less convective cooling of the wall. **Figure 6.9(b)** shows the distribution of wall temperature along the length of the combustor. The wall temperature is seen to increase along the combustor length in all the three cases. However, the highest wall temperature is attained with the 50:50 air flow split and the lowest with 30:70 split. This is attributed to the fact that even with a much higher incident radiation in the 30:70 flow split case, the higher convective cooling due to increased secondary air flow keeps the wall at a lower temperature. On the contrary, though in the 50:50 case, the maximum radiative flux incident on the wall is low, but the wall temperature reaches a higher value as the secondary air flow adjacent to the wall is less.

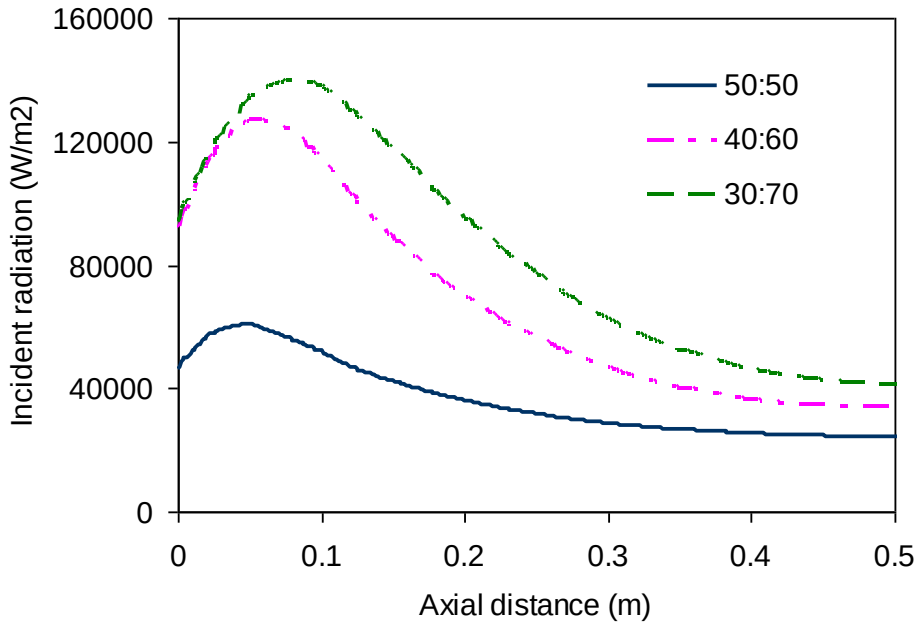

(a)

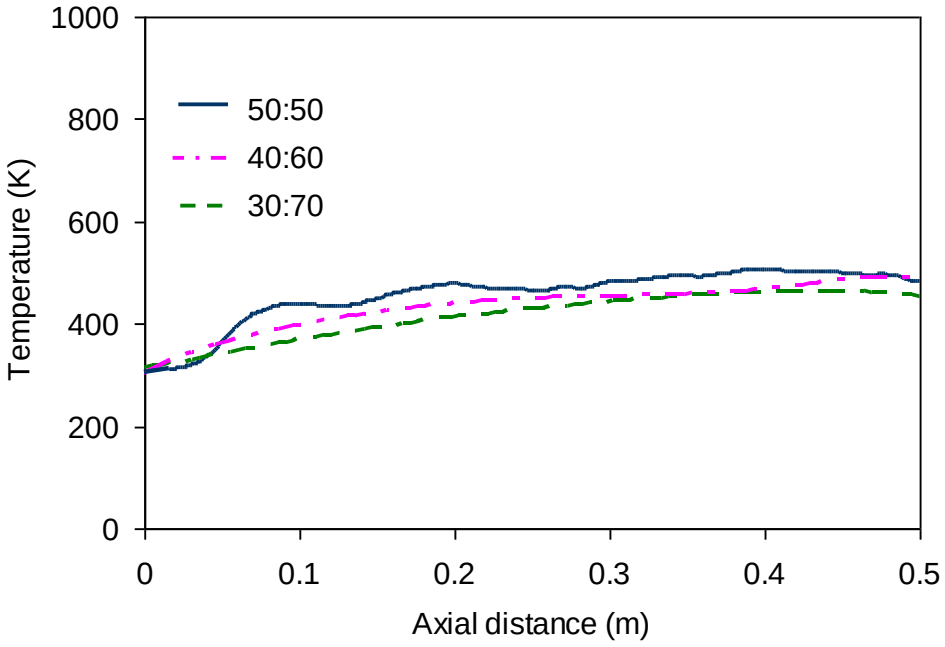

(b)

Figure 6.9 Variation of (a) incident radiation, (b) outer wall temperature along the combustor length for three different air flow splits.

An efficiency (η) term has been defined as the ratio of the total energy flow rate at the outlet to that at inlet. The calculated efficiency values have been listed in **Table 6.1**. It shows that as the swirl number is increased the combustor efficiency decreases.

Table 6.1 Combustor efficiency at different air split.

mass flow distribution primary :Secondary	$\eta = \frac{Total\ energy\ flow\ rate\ at\ combustor\ outlet}{Total\ energy\ flow\ rate\ at\ combustor\ inlet}$
30:70	90.91%
40:60	90%
50:50	89.4%

It is also significant to study the incident heat flux and the surface temperature on the fuel injector considering the life of the injector. **Figure 6.10** and **6.11** show the incident radiation flux and surface temperature, respectively, on the swirler –injector assembly at the inlet to the combustor for the three different cases of air flow splits. It

is clearly seen that the fuel injector is the more critical part than the swirler as it receives more radiative heat flux and attains a higher temperature. On the other hand, the primary air, which directly flows over the swirler, keeps the surface of the swirler cool. The incident radiation on the fuel injector is the highest for the case of lowest primary air fraction (**Figure 6.10(a)**) due to increased radiation from the flame. This is attributed to the higher soot concentration in the flame in this case. The high incident radiation causes the fuel injector surface temperature to reach a value above 1100 K in this case (**Figure 6.11(a)**). The incident radiation flux on the injector surface reduces as the primary air fraction is increased (**Figures 6.10(b)** and **(c)**). However, the surface temperature distributions on the injector (**Figures 6.11(b)** and **(c)**) do not show a decrease in value for the corresponding cases. This may be attributed to the stronger convective heat transfer with the increase in primary air fraction. When the primary air flow rate increases, the central recirculation zone established on the combustor axis becomes more intensified. As a result, the high temperature gas from the downstream flows back with a higher velocity towards the injector. The resulting higher convective heat transfer offsets the lower incident radiative heat flux and maintains the injector nearly at the same high temperature for all the three cases. Thus the fuel injector remains as the more critical component of the combustor and its material has to be selected properly to save it from failure.

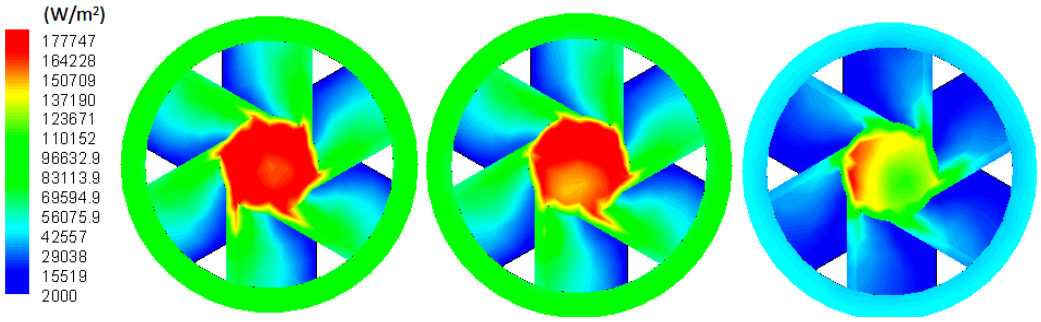

Figure 6.10 Distributions of incident radiation on the swirler–injector planes for three different air flow splits between primary and secondary streams (a) 30:70, (b) 40:60 and (c) 50:50.

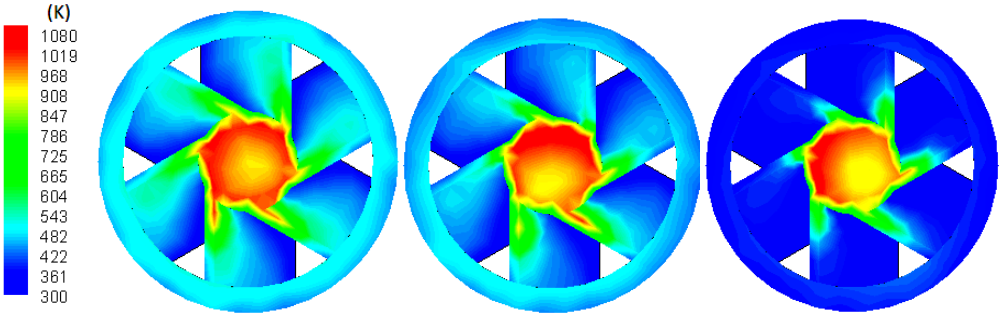

Figure 6.11 Temperature distributions across the swirler–injector plane for three different air flow splits between primary and secondary streams (a) 30:70, (b) 40:60 and (c) 50:50.

6.6 Conclusion

The model combustor under consideration has an air flow split between primary and secondary streams entering co-axially. The effect of air flow distribution on different combustor parameters has been investigated by considering three primary to secondary flow rates as 30:70, 40:60 and 50:50. The results show that as the proportion of the primary air increases from 30% to 50% of the total air flow, the flame becomes more compact. This leads to less soot production in the flame zone and a more uniform temperature pattern factor at the combustor exit. With the reduction in soot formation, the incident radiative heat flux decreases with the increase in primary air fraction. The increase in primary air from 30% to 50% of the total air flow reduces the maximum incident heat flux on the peripheral wall by more than 50%. However, reduction in the air flow rate near the combustor wall leads to higher wall temperature, particularly close to the inlet. In addition, the lower soot formation in the flame at higher primary air fraction decreases the radiative heat flux from the flame on the injector surface by more than 25%. However, the convective heat transfer to the injector surface counterbalances the variation in radiative heat flux and the injector surface temperature remains nearly the same under all the three air flow splits.

Chapter 7

Effect of swirl on soot and radiative heat transfer

7.1 Introduction

In gas turbine combustor, the primary air enters into the combustor through a set of inclined vanes called swirler. Due to the swirl imparted to flow by the vane, the pressure near the axis falls to create an adverse pressure gradient; as a consequence of which a central recirculation zone is formed. Swirl flows are used widely in gas turbine combustors to promote flame stability, improve combustion efficiency and control emission of pollutants [15]. Swirl in the primary flow significantly influences the flow and flame structures in the combustor. The stronger recirculation at high swirl draws more air into the flame region reduces the flame length and peak flame temperature and also brings the soot laden zone closer to the inlet plane. As a result, the radiative heat flux on the peripheral wall decreases at high swirl and also shifts closer to the inlet plane. However, increased swirl increases the combustor wall temperature due to radial spreading of the flame. The high incident radiative heat flux and the high surface temperature make the fuel injector a critical item in the combustor. The injector peak temperature increases with the increase in swirl flow mainly because the flame is located closer to the inlet plane. On the other hand, a more uniform temperature distribution in the exhaust gas can be attained at the combustor exit at high swirl condition.

In this chapter the same 3-D geometry as shown in **Figure 7.1** has been used as described in previous chapter. The mass flow rate of air is set at 0.04 kg/s at 300K temperature as in the previous chapter. The total intake air has been split to 50% for each air inlet— primary and secondary. The effects of degree of swirl on various combustion parameters have been studied by considering three different swirler vane angles of 40^0, 50^0 and 60^0, respectively. The simulation of combustion process in this current work is conducted with laminar flamelet model that has been described in chapter 3.4.

In this work a non dimensional swirl number has been used that represents the vane angle along with primary inlet diameter and hub diameter. The swirl number is calculated using the relation as given in Eq. 2.16.

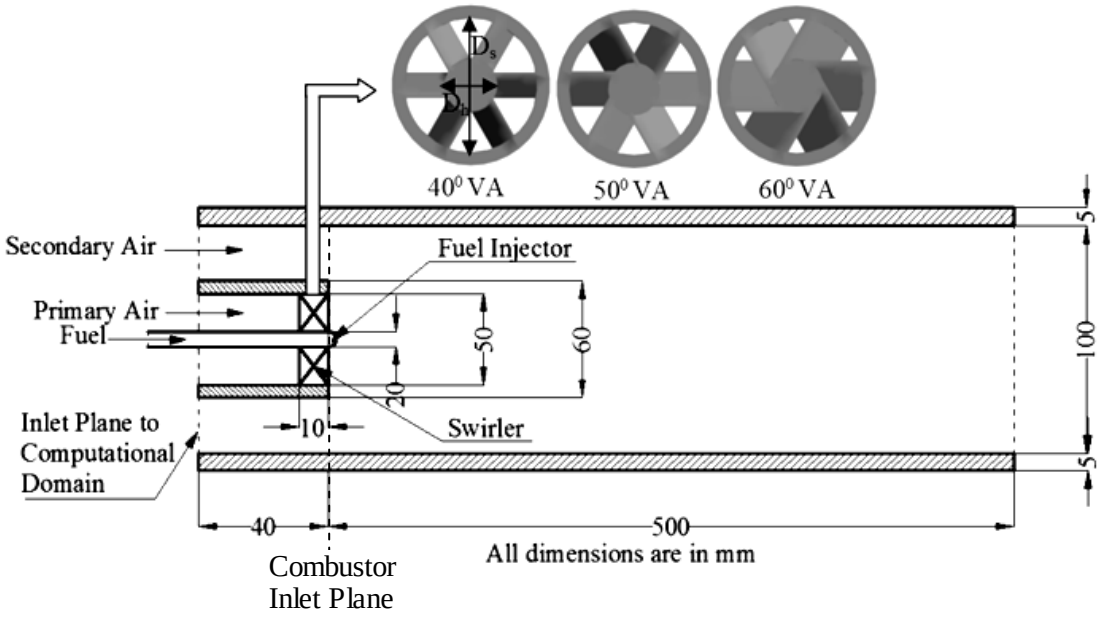

Figure 7.1 Schematic of the model combustor along with the swirlers with different vane angles

For both primary and secondary inlet, turbulent intensity is set at 4% and length scale is 0.007m. Pressure outlet boundary condition has been chosen for the outlet boundary. The materials for all the walls are specified as stainless steel. The walls are assumed to be no slip and a mixed (convection and radiation) boundary condition has been given to account the heat loss from the system to the atmosphere. A calculated value for heat transfer coefficient in between the outer wall and surrounding atmosphere has been specified along with the external emissivity and internal

emissivity for the wall surface material. Ambient temperature has been set at 300K and the thickness of the wall is taken as 5mm. However, the fuel injector wall is considered as adiabatic. For dispersed phase calculation, all the walls are specified as reflecting wall.

In this work, the effects of different swirl levels on soot formation and temperature distribution in the combustor have been studied numerically. The computational work has been carried out with three different swirler vane angles of 40^0, 50^0 and 60^0 in the primary air flow. The corresponding swirl numbers are 1.038, 1.474 and 2.142, respectively. The numerical results for the three different cases have been presented in the following sections. It has been observed that except near the inlet plane of the combustor, close to the swirler, sufficient axial symmetry in the results have been achieved. Therefore, the results have mostly been presented in the vertical plane passing through the axis of the combustor.

7.2 Velocity and temperature distributions

The temperature contours in the vertical planes across the combustor axis along with the velocity vectors in that plane have been shown in **Figure 7.2 (a) to 7.2 (c)**, for the three swirl cases considered. The flame region can be depicted by the high temperature zone formed in the combustor. From the figures it is evident that the flame in the combustor is quite long for the lowest swirl (SN=1.038) in primary air flow while, with the increase in swirl strength the flame becomes progressively shorter. The tangential entry of the primary flow forms a central toroidal recirculation zone around the axis of the combustor. At low swirl (SN=1.038), the strength of the recirculation zone is rather weak. The injected fuel evaporates and mixes with air to form the fuel-air mixture which, driven by the flow, moves axially forward to burn around the central axis. As a result, the highest temperature zone is located on-axis and the flame occurs downstream to the central on-axis vortex. When the swirl number is increased to 1.474, the central recirculation becomes stronger. The strong recirculating bubble concentrates the fuel-air mixture closer to the inlet than before. The highest temperature contours, representing the flame zone, still remain on the axis (**Figure 7.2 (b)**) but moves nearer to the inlet. However, the peak temperature is increased because of more intense combustion than in the previous case. At the

maximum swirl number considered (SN = 2.142), the reverse flow due to recirculation becomes so strong that it draws the gas from the downstream location to move it upstream with high velocity (**Figure 7.2 (c)**). The strong reverse flow splits the flame and shifts it off-axis. As a result, the flame becomes annular in shape and spreads in the radial direction. Moreover, the strong vortical structures in the recirculation bubble create a lot of turbulence in the flow. The turbulence increases the transport rate of heat leading to a decrease in the peak temperature.

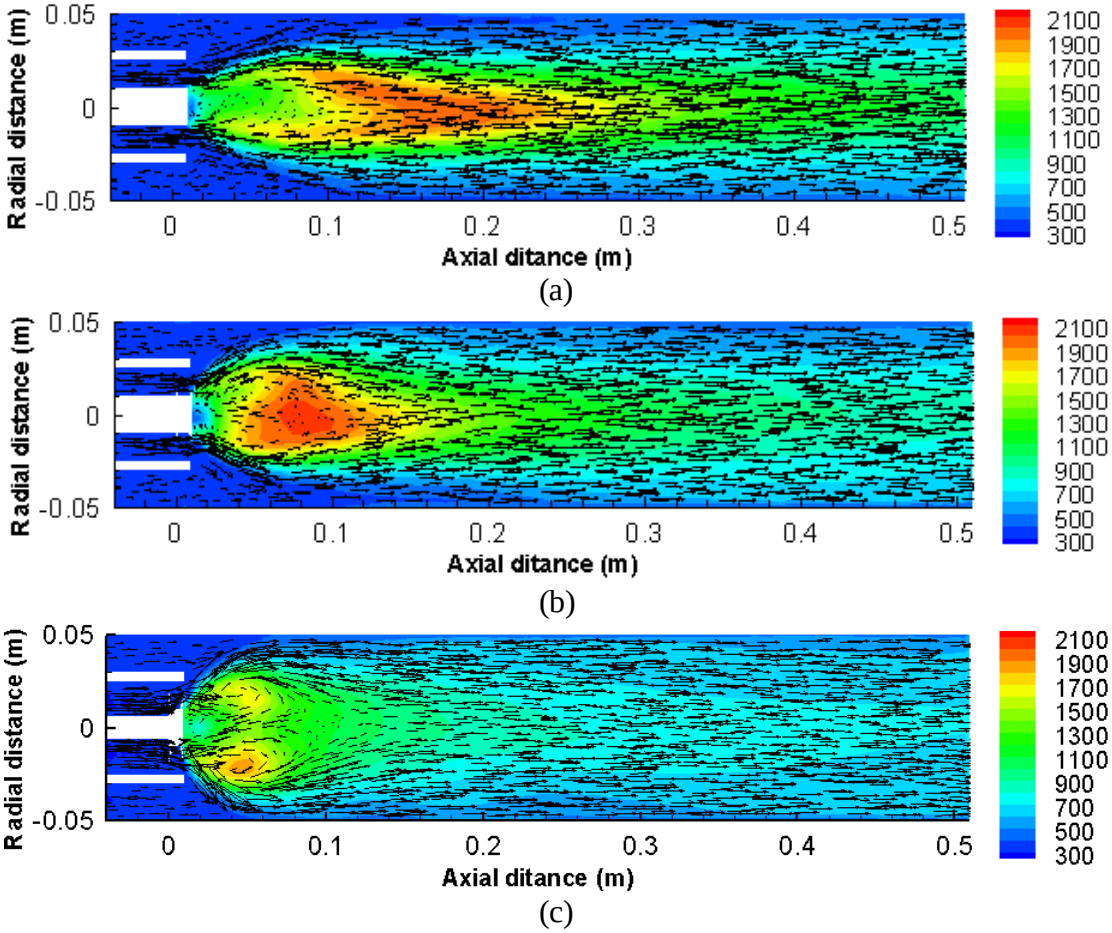

Figure 7.2 Temperature variation on the central vertical combustor plane along with superimposed velocity vectors at different swirler vane angles (a) 40^{O} (b) 50^{O} (c) 60^{O}

The temperature distribution along the combustor centreline illustrates the flame structure. **Figure 7.3(a)** portrays the temperature distributions along the central axis at different swirl levels. At swirl number of SN=1.038, the centreline temperature first increases to reach the peak value of 1977 K at a distance of 0.1718 m from the combustor inlet plane (shown in **Figure 7.1**). The temperature decreases along the

axial direction after reaching the peak value. The same trend in centreline temperature distribution is also followed for SN=1.474. However, in this case, the peak temperature is attained at a relatively upstream location (0.067 m from combustor inlet plane) and the peak temperature value is also a little higher (2050 K). The change in the distribution is attributed to the shorter flame length with SN=1.474 than with SN=1.038. The centreline temperature distribution finds some difference at SN=2.142. In this case, the temperature is about 915 K on the injector located at the combustor entry plane, which is higher than the corresponding values in the previous two cases. The temperature first drops over a little length and then increases to reach the peak value at 0.043 m from the combustor inlet. The peak centreline temperature is only 1467 K in this case, which is much lower than the same in the previous two cases of lower swirl number. The high temperature on the injector surface for the high swirl case can be attributed to the radiation from the flame, which is short and located close to the injector. Thus the effect of radiative heating on the injector is much stronger in this case. Moreover, as the flame shifts to an off-axis location at high swirl, the peak temperature on the centreline becomes lower than in the other two cases.

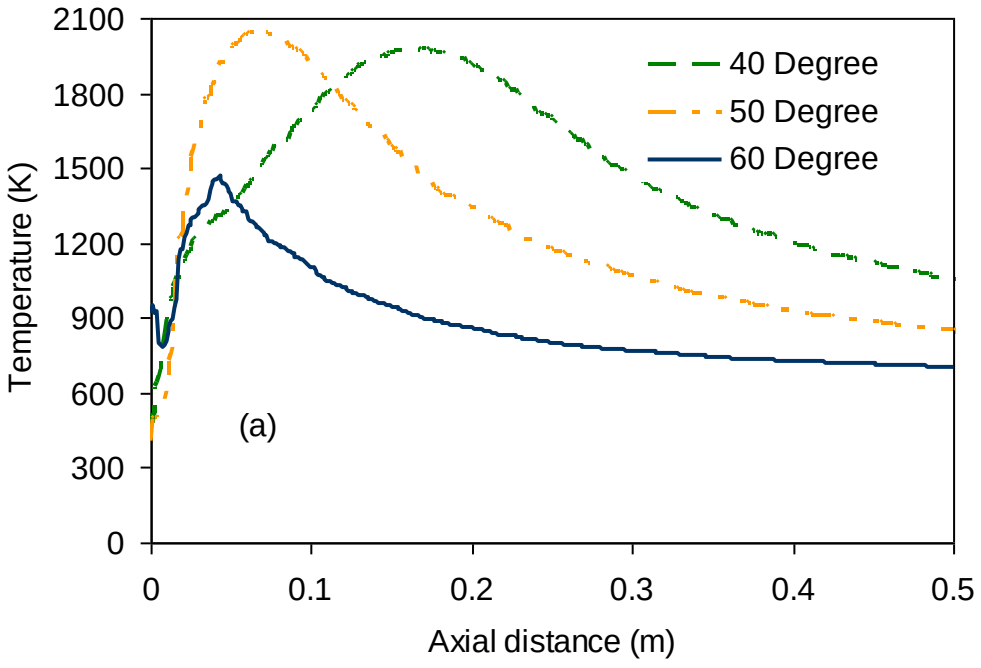

(a)

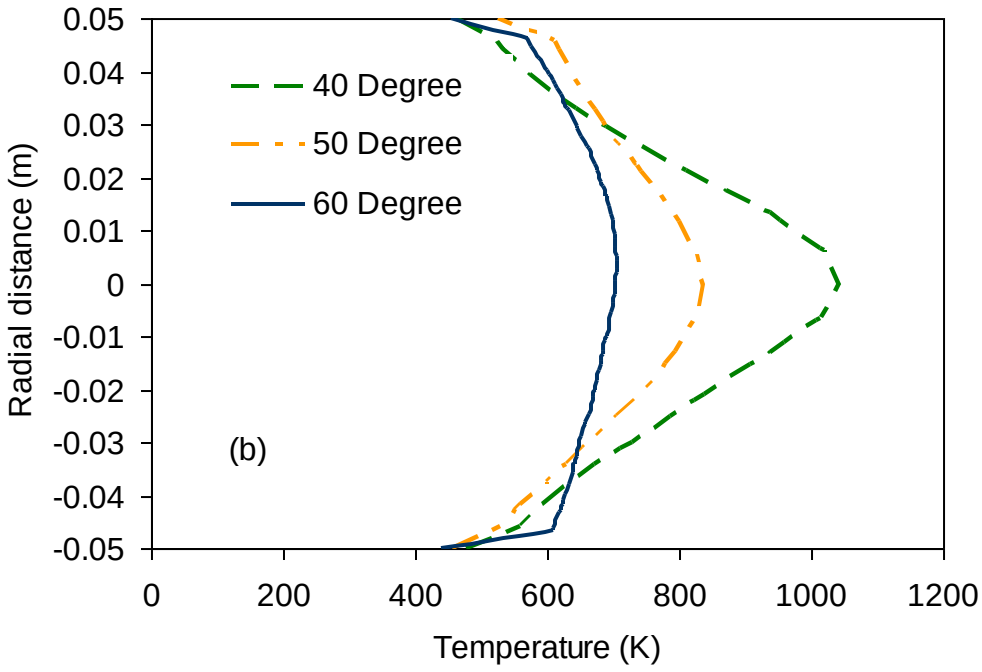

(b)

Figure 7.3 Variation of temperature (a) along the axis (b) across the radius at exit plane, at different swirler vane angles

Figure 7.3(b) shows the radial temperature distribution at the exit plane of the combustor for the three different swirl cases. The temperature distribution at the exit determines the pattern factor for the gas turbine and should have an acceptable uniformity (low pattern factor) to improve the life of the turbine. It has already been discussed that with the decrease in swirl strength, the flame length increases and the combustion occurs much away from the inlet plane of the combustor. As a result, there will be less time available for the transport of energy in order to achieve a uniform temperature distribution in the gas. Thus the distribution of temperature along the radial direction becomes poor. On the other hand, the temperature distribution is more uniform at higher swirl, where the flame is compact, spreads radially and has lower peak temperature. Therefore, the higher swirler vane angle will result in a better pattern factor in this case.

7.3 Soot volume fraction distribution

Figure 7.4(a) to 7.4(c) shows the distribution of soot volume fraction on the vertical plane across the combustor axis for different swirl levels. From these contours it has

been found that the soot laden zone is established around the central axis in all the cases. Soot in non-premixed flame forms in the fuel-rich zone, where the concentrations of the soot precursors remain high. As the injector is located centrally on the axis the fuel-rich zone is formed around the central axis only. The soot laden zone shifts location in different cases based on the concentration of precursor species and temperature. In the lowest swirl case, the flame shifts away from the injector driven by the flow field in the combustor and accordingly shifts the soot laden zone to a downstream location (**Figure 7.4(a)).** As the inlet swirl level is increased the soot laden zone is drawn closer to the inlet (**Figure 7.4(b)).** At the highest swirl case, the peak soot location occurs closest to the injector plane (**Figure7.4(c)).** The peak soot volume fraction is a little higher in the case of SN=2.142 compared to the other two cases. However, in all the three cases, the soot formed in the flame gets oxidized downstream and becomes negligible at the exit of the combustor.

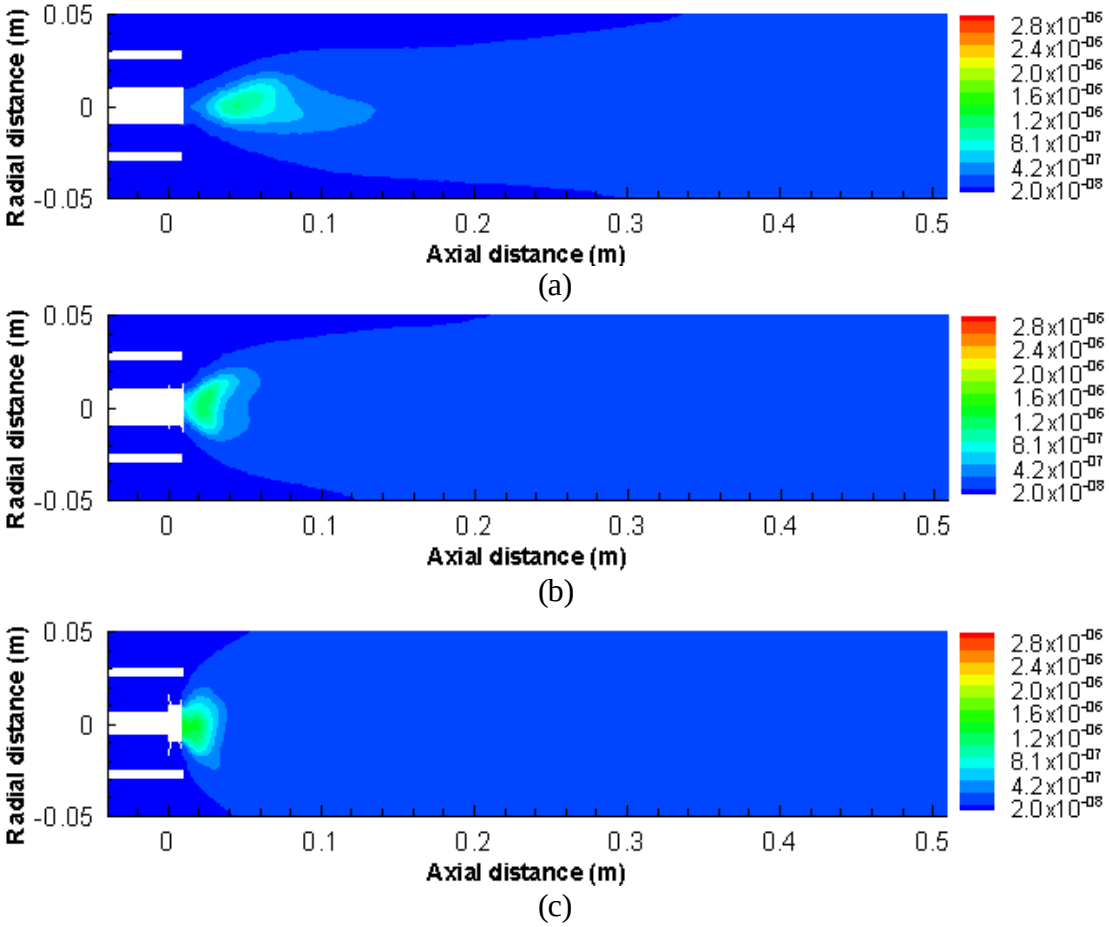

Figure 7.4 Soot volume fraction distribution on the central vertical combustor plane at different swirler vane angles (a) 40^{O} (b) 50^{O} (c) 60^{O}

7.4 Species mass fraction distribution along the axis

Figure 7.5(a) to 7.5(c) shows the distribution of various major species and OH along the central axis of the combustor for swirl numbers of 1.038, 1.474 and 2.142, respectively. The concentration of OH species (shown on the secondary axis) is plotted in the figures to identify the reaction zone on the combustor centreline. In the lowest swirl case (**Figure 7.5(a)**), the fuel ($C_{12}H_{23}$) vapour mass fraction close to the injector is 0.845. The fuel vapour concentration drops rapidly to become less than 0.001 at around 0.13 m from the injector plane. The O_2 mass fraction at this distance is nearly 0.003 and it increases from this point in the downstream direction. The peak in the OH-concentration, however, occurs at 0.2 m, where the CO_2 also peaks in concentration and CO concentration has fallen down to a small value. It indicates that the OH- radical is primarily responsible to form CO_2 by reacting with CO. The maximum H_2O mass fraction on the central-axis occurs a little before the peak in CO_2 is attained.

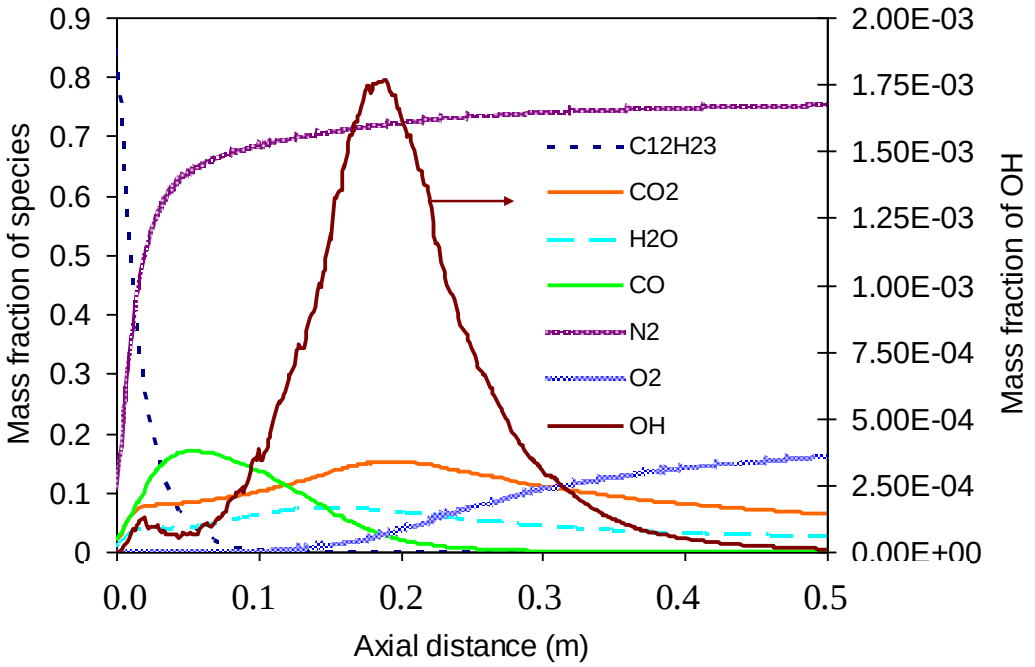

(a)

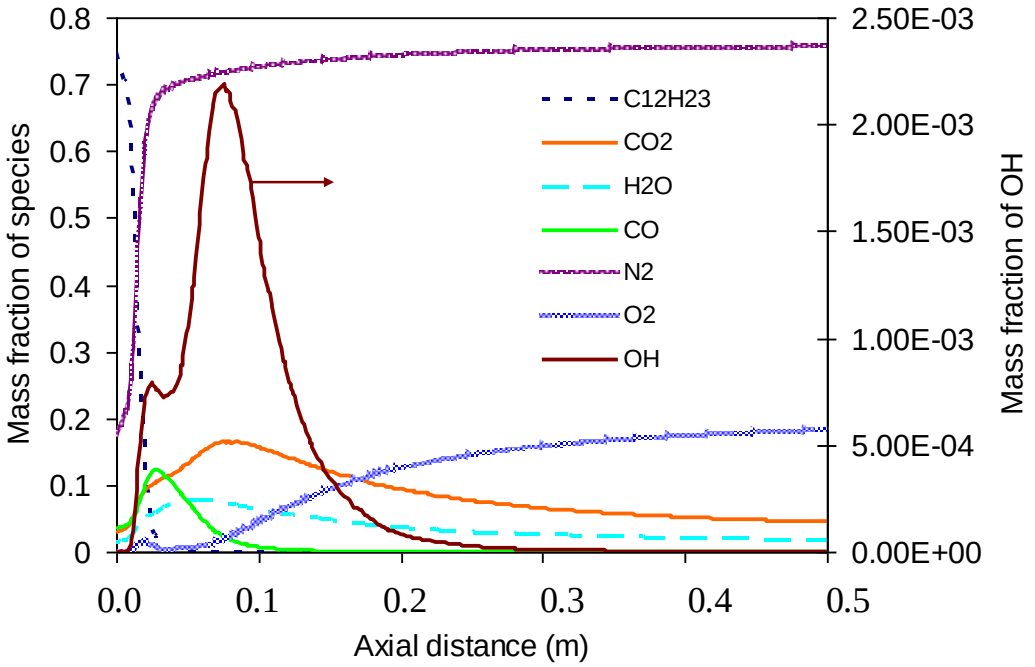

(b)

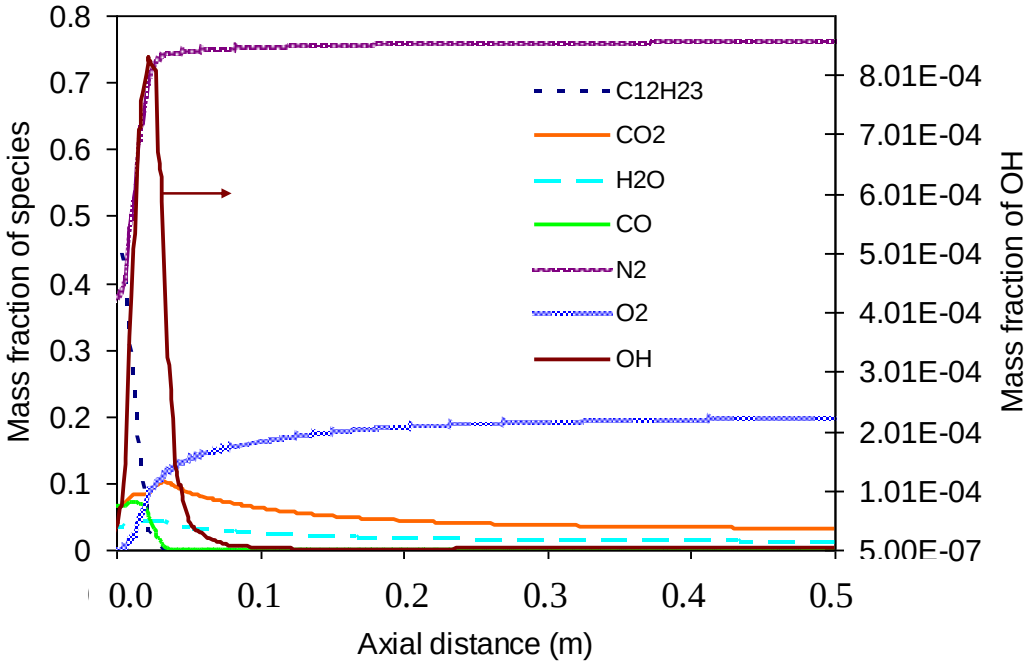

(c)

Figure 7.5 Distribution of species mass fraction along the axis at (a) 40^{O} (b) 50^{O} (c) 60^{O} swirler vane angle

As the swirl number is increased to 1.474, the flame becomes shorter in length while maintaining around the centreline. The peak OH- mass fraction occurs at 0.086 m in this case, as shown in **Figure 7.5(b).** The location of peak OH-mass fraction moves even closer to the injector plane (0.043 m) as the swirl number is further increased to 2.142. Moreover, in this case, the peak OH- mass fraction value (~8×10^{-4}) is less than that in the previous two cases (~2×10^{-3}). This can be attributed to the off-axis flame location in the highest swirl number case. The strong central recirculation brings back gaseous mixture from the downstream to the upstream location. As a consequence, the concentration of fuel vapour near to the injector is much less for SN=2.142 case than in the other two cases. The centreline oxygen concentration also begins to rise quite early in the highest swirl case. It indicates the influence of swirl on the mixing of the fuel and air and confirms the reason of early soot oxidation noted before. The effect of dilution of the product stream with the secondary air beyond the flame zone gradually increases the oxygen concentration and decreases the concentrations of the product species, like CO_2 and H_2O. CO concentration drops down to zero much before the combustor outlet indicating completion of the combustion reaction in the overall fuel lean environment.

7.5 Temperature and incident radiation on combustor wall and swirler-injector

The temperature along the combustor wall is considered as a significant parameter concerning the metallurgical barrier for wall material as well as to minimise the heat loss. In a non-premixed combustion system, as in the combustor, radiation from the flame is one of the vital modes of heat transfer both due to very high flame temperature and increased flame emissivity by soot. **Figure 7.6(a)** shows the incident radiation along the combustor wall for three different swirl levels. It has already been discussed that with weaker swirl in flow, the flame becomes stretched in the axial direction. Therefore the highest incident radiation flux on the wall for weaker swirl case (SN=1.038) occurs at a location furthest from the injector plane (0.1258 m). Increase in swirl number (SN=1.474) makes the flame shorter. Accordingly, the peak radiative flux location is drawn towards the inlet (0.0844 m). Moreover, the magnitude of the peak flux is found to decrease from 70445 W/m^2 at SN=1.038 to 65776 W/m^2 at SN=1.474. This lowering in the magnitude of the peak flux may be

attributed to the smaller size of the flame emitting radiation. When the swirl number is further increased to SN=2.142, the location of the peak incident radiation flux on the wall moves further towards the inlet (0.0467 m) and the peak value decreases further (60813 W/m^2). This is due to the lower temperature of the flame as well as shorter flame length in this case of operation.

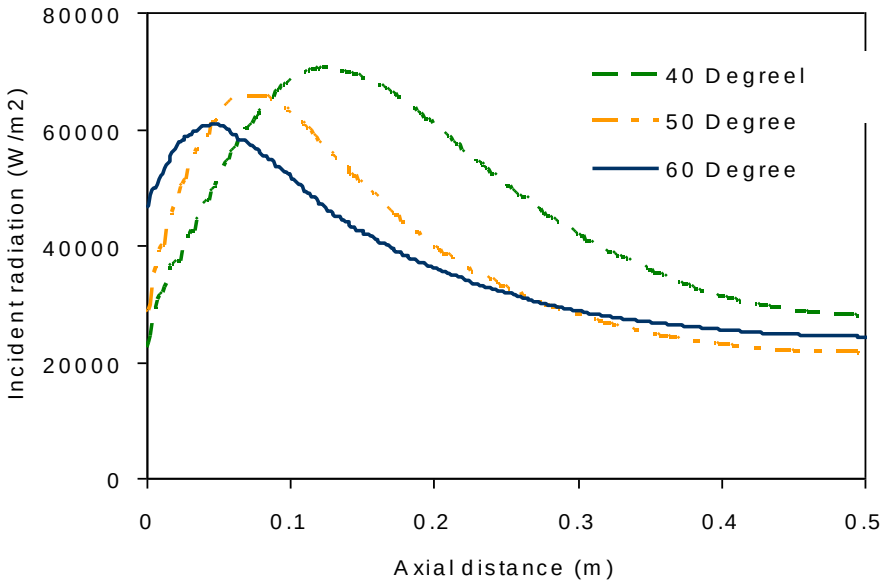

(a)

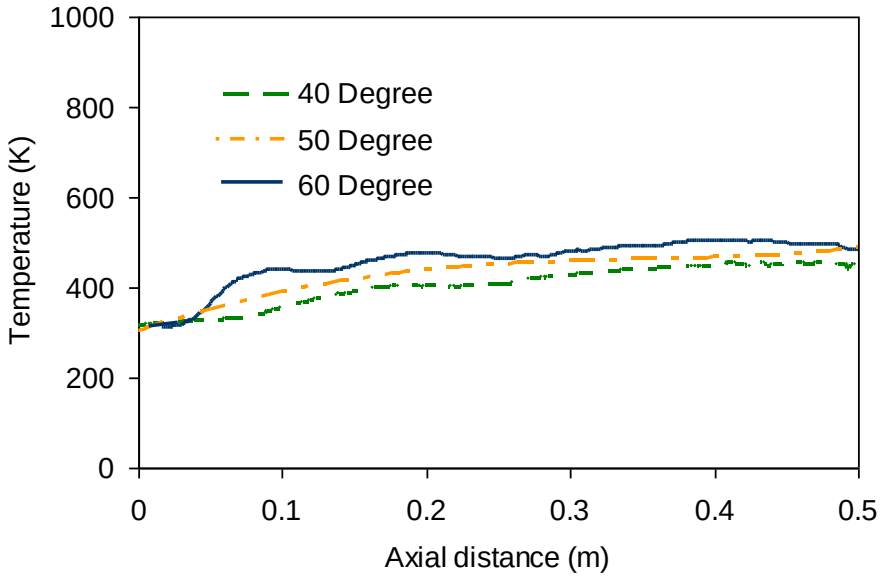

(a)

Figure 7.6 Variation of (a) incident radiation, (b) temperature along the combustor wall at different swirler vane angles

In contrast to the above, operation at lower swirl provides low combustor wall temperature as shown in **Figure 7.6(b)**. In this case, the weaker tangential momentum in the flow is unable to spread the flame radially. On the other hand, the secondary air admitted into the combustor moves along the wall surface, causing a wall cooling effect. At higher swirl, the stronger tangential momentum spreads the flame outwardly and mixes the hot products of combustion with the secondary air. Consequently the wall cooling effect by secondary air is reduced. Thus the wall temperature for the case of higher swirl is always more throughout the length of the wall as compared to weaker swirl, even though the former case experiences lower incident radiation on to the wall. The higher wall temperature results in more heat loss through the outer wall in case of the high swirl case and reduces the efficiency of the combustor. An efficiency (η) term has been defined as the ratio of the total energy flow rate at the outlet to that at inlet. The calculated efficiency values have been listed in **Table 7.1**. It shows that as the swirl number is increased the combustor efficiency decreases.

Table 7.1 Combustor efficiency at different swirl level

Swirl No.	$\eta = \frac{\textit{Total energy flow rate at combustor outlet}}{\textit{Total energy flow rate at combustor inlet}}$
1.038	91.6%
1.474	90.6%
2.142	89.4%

Another important consideration in the combustor performance is the heat transfer to the swirler-injector assembly. **Figure 7.7(a) to 7.7(c)** depicts the incident radiation on the swirler-injector plane at different swirl levels. It has been clearly seen that the incident radiation flux on the injector region is much more than that on the swirler vanes. In fact, the peak incident heat flux on the injector is even higher than its peak value on the outer wall surface (**Figure 7.6(a)**). A little asymmetry is observed in the incident radiation flux on the injector surface. It may be attributed to the presence of the vane swirler and its effect on flow near the injector. Though, the effects of radiation on the injector in both low and medium swirl cases are almost same, it is

increased in the high swirl case of SN = 2.142. The increased incident radiation flux at high swirl can be attributed both to the proximity of the flame to the injector and increase in soot volume fraction in the flame there. The incident radiation on the swirler vane also increases with the increase in swirl level.

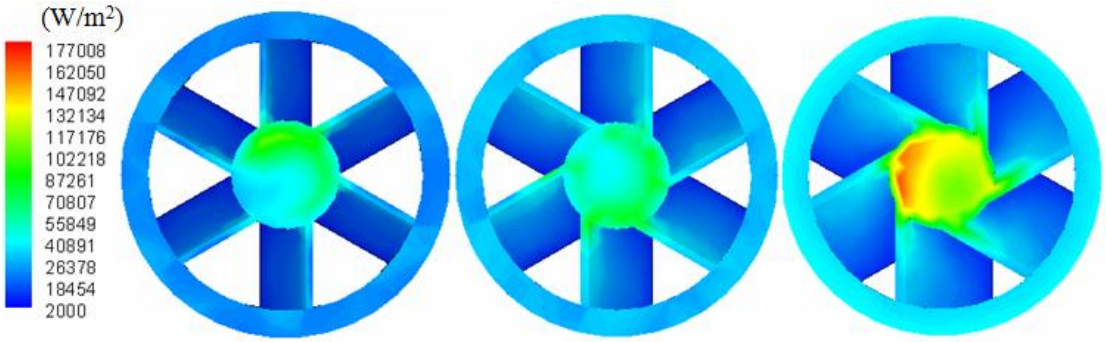

(a) (b) (c)

Figure 7.7 Distribution of incident radiation on swirler-injector plane for different swirler vane angles (a) 40^O (b) 50^O (c) 60^O

Temperatures of swirler vanes and injector are important considering the proximity of these parts to the soot laden flame zone. These parts should be able to withstand the maximum temperature on them and the materials of the parts have to be accordingly chosen. **Figure 7.8(a) to 7.8(c)** shows the distributions of temperature on swirler-injector plane at three different swirl levels. It is revealed from the figures that the temperature on the injector plane for the highest swirl case (SN = 2.142) is much more than those in the other two cases. It may be attributed to the proximity of the flame to the injector at high swirl flow and the resulting higher incident radiative heat flux on the injector surface. It is further interesting to observe that the peak temperature of the injector surface does not increase with the inlet swirl number progressively. Rather, the lowest peak temperature on the injector was found at moderate swirl (SN = 1.474) of the primary flow. With swirl in the primary flow of air, the strength of the central toroidal recirculation increases in strength. The recirculated fluid flows over the injector to give a convective cooling effect to the surface. At mild swirl (SN = 1.038), the cooling effect is less due to weaker recirculation bubble and the injector surface peak temperature increases again in comparison to that at moderate swirl (SN = 1.474). It is also observed from the figures that the temperature of swirler vanes is much less than that of the injector due

to the cooling effect induced by the air flowing over them. Moreover, the vane temperature is high only at the edge facing the flame in the combustor. The swirler vane temperature progressively increases with the increase in the swirl level. This is primarily due to increased incident radiation heat flux on the vane at higher swirl. However, the peak temperature of the swirler vane is much less than that of the injector.

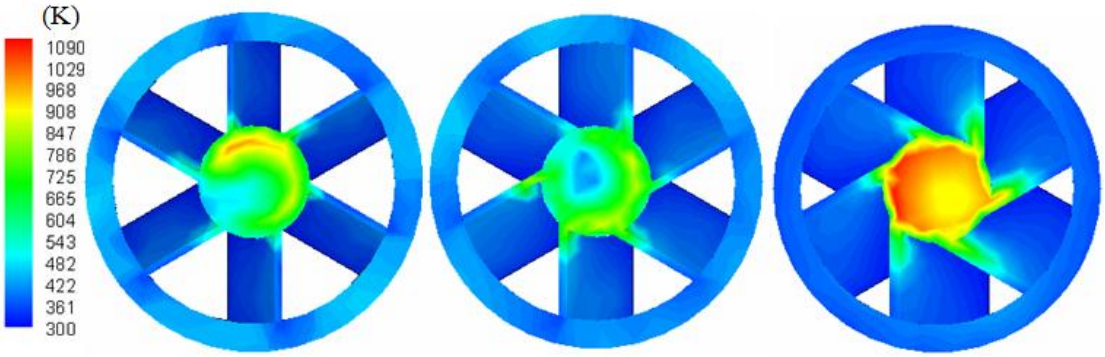

(a) (b) (c)

Figure 7.8 Distribution of temperature on swirler-injector plane for different swirler vane angles (a) 40^O (b) 50^O (c) 60^O

7.6 Conclusion

In this chapter, a numerical study has been presented investigating the effects of inlet swirl on spray combustion of kerosene issued from a pressure swirl atomizer in a cylindrical combustion chamber. It is found that increased swirl in the primary air flow shortens the flame. When the swirl is sufficiently strong, the flame even changes to an annular structure following a strong recirculation. Moreover, under high swirl, the peak temperature in the flame decreases due to the mixing of excess air in the flame region. The species concentrations across the flame show that the flame length can be mapped well by the OH-distribution in the combustor. The soot laden zone comes closer to the inlet following the increase in swirl. However, in all the cases studied, the soot formed in the flame gets subsequently oxidized avoiding any emission from the combustor. The longer flame at lower swirl, increases the incident radiation heat flux on the peripheral wall of the combustor and steer the peak radiative zone downstream along the combustor wall. The combustor wall temperature is found to increase with the increase in swirl, resulting in an increase in

heat loss and decrease in efficiency of the combustor. On the other hand, the incident radiation heat flux on the injector-swirler assembly increases with the increase in swirl number. The injector is found to be the more critical item, experiencing much higher temperature than that of the swirler vanes. The injector peak temperature increases with the increase in swirl flow mainly because of the location of the flame close to the inlet plane. The exhaust gas temperature distribution, however, becomes more uniform with the increase in swirl, as the flow mixing in the combustor is enhanced.

Chapter 8

Overall Conclusion and Scope of Future Work

8.1 Overall Conclusion

Combustion of liquid fuels has wide applications. However, the simulation of the process is highly complicated as it involves many physical and chemical phenomena, like turbulent transport, radiation, evaporation in two phase motion and chemical reaction. The main aim of this work is to choose proper models to simulate the spray combustion problem in a model gas turbine combustor and also to study the following.

i) the effect of air mass flow distribution on temperature field and soot formation considering radiation.

ii) the effect of inlet swirl on temperature field, soot formation and species concentration considering radiation.

However selection of turbulent model for swirl inlet, as in case of the combustor, is a prominent part of the thesis which has been discussed in brief in chapter 2. Two equation turbulence models along with RANS simulation are widely used for their computational economy. It has been found from the present study that realizable k-ε model predicts better than standard k-ε model and RNG k-ε model in swirl flow. RNG k-ε model fails to predict mild swirl flow because it becomes more responsive to the effects of rapid strain and streamline curvature. On the other hand in contrast to

standard k-ε model, realizable k-ε model considers a variable C_μ in the eddy viscosity expression, which is expressed as a function of the mean strain, mean rate of rotation and turbulence quantities, which causes better prediction for swirling flow. Therefore Realizable k-ε model is used to simulate the combustion problem in this work.
In spray combustion problem as there is an interaction between gas phase and liquid phase, Eulerian-Lagrangian frame has been used to simulate the problem which includes mass interaction, momentum interaction and heat interaction between gas phase and droplet phase. LISA model is used to determine the spray distribution for a hollow cone injector. DO radiation model is used to put the effect of radiation in the simulation process.

Another contribution of this thesis is the comparison of three combustion models such as: eddy dissipation model, laminar flamelet model and constrained equilibrium model. The results are validated with the experimental results obtained from in-house experimental setup. Liquid kerosene ($C_{12}H_{23}$) is used as fuel in this work. It has been found that eddy dissipation model predicts poorly due to the single step reaction mechanism with empirical rate constants and due to its dependency on the turbulent quantities. The wall temperature is highly over predicted near the flame region and the exit temperatures along the radius are also found to be over predicted. Both laminar flamelet model and constrained equilibrium model predict fair results which are close to each other. The key finding from this part of the thesis is that, the constrained equilibrium model can predict accurate result with less CPU time if, the constraint condition is chosen correctly. In this work, the constraint is set by setting the rich flammability limit (RFL) at 1.5 times of equivalence ratio (equivalence ratio is 0.064), thus setting the RFL at 0.096. However, the choice of the correct RFL value remains a tedious job and needs validation. Therefore, in case the correct chemical mechanism for the reaction of a fuel is unavailable or complex, constrained equilibrium model can be properly set to predict the combustion of the fuel. Otherwise, the laminar flamelet model with the detailed chemical mechanism may be chosen as the combustion model even though it takes little more CPU time.

Modelling of soot for kerosene spray flame is a major contribution from this study. Two equation semi empirical soot model is used [98] to simulate the soot formation. Acetylene is considered as the precursor species for nucleation and also as the surface growth species. In this work, the model constants for the soot processes

have been modified suitably for the kerosene fuel. The model constants are selected through validation with the experimentation of Young et al.[142] and with the PAH model of Wen et al. [104]. The predicted soot distribution and temperature distribution along the axis and the predicted temperature along radius at different positions above inlet are very much close to experimental data.

The selected models are used to simulate the combustion in a 3-D model gas turbine combustor. The effect of air mass flow distribution on temperature field and soot formation considering radiation has been studied. It has been found that increase in air supply through primary swirled inlet decreases the flame length. When the primary air increases to 50% of the total air the flame gets split due to the strong back-flow. Therefore with a higher supply of primary air, the centreline temperature decreases. Moreover in same case the soot formation also becomes lesser because the flame temperate reduces due to breaking of flame but the wall temperature increases. Due to the higher wall temperature heat loss increases through wall. Therefore the overall combustor efficiency decreases but the pattern factor at outlet becomes better. It is also found that with decrease in air supply through primary inlet; increase the temperature of swirler assembly due to higher incident radiation. However the patter factor increases with increase in air supply through the primary inlet.

The effects of swirl level on soot and heat transfer also have been studied. It has been depicted that, at lower swirl, the flame length increases. As the swirl level increases the flame length become shorter. At certain swirl level (60^o vane angle), the flame is divided and the centreline temperature decreases. However the soot formation does not affect much with swirl level. But at higher swirl the soot laden zone become closer to injector tip. The injector plane area also becomes hotter as swirl level increases. The combustor efficiency is better at lower swirl as comparatively lesser heat loss occurs in this case. Moreover it is also found that the peak value of OH mass fraction becomes closer to the inlet plane with the increase in swirl level. Therefore the oxidation of soot becomes more effective near the inlet region. Another finding is that, where the CO_2 reaches its peak in concentration, CO concentration has fallen down to a small value. It indicates that the OH- radical is primarily responsible to form CO_2 by reacting with CO. The pattern factor at exit is more uniform in case of higher swirl but combustor efficiency decreases in same

case. Finally it has been concluded that to get desired output, more air should be supplied through primary inlet with a better swirling action.

8.2 Scope of future work

- In this work only three different two equation turbulent model as well as three different combustion models are validated. Different other turbulent models, combustion models and radiation models may be used and the accuracy of the problem can be checked.
- In this work Moss Brookes soot model is modified for kerosene fuel considering acetylene as precursor species as well as surface growth species. The soot model can be modified for other heavy hydrocarbon fuels by considering acetylene as precursor and surface growth species or by considering benzene as precursor as well as surface growth species.
- In this work the RFL of constrained equilibrium model has been chosen by checking at what RFL value the mean temperature variation with mean mixture fraction of constrained equilibrium model is closer to the variation of mean temperature with mean mixture fraction at highest scalar dissipation rate of flamelet model. A simple mathematical relation can be developed to establish the proper value of RFL.
- In this work both primary and secondary air is fed axially into the combustor. No study has been conducted with feeding of dilution air. The effect of dilution air on temperature distribution and soot formation through radial entry can be studied.

References

[1] Moin P, Apte SV. Large-eddy simulation for realistic gas turbine combustors, AIAA J. 44 (4) (2006) 698–708.

[2] Mondal S, Datta A, Sarkar A. Influence of side wall expansion angle and swirl generator on flow pattern in a model combustor calculated with k–ε model, International Journal of Thermal Sciences, (2004) 43, 901–914.

[3] Li L, Liu T, Peng XF. Flow characteristics in an annular burner with fully film cooling", Applied Thermal Engineering (2005) 25, 3013–3024.

[4] Mare F di, Jones WP, and Menzies KR. Large eddy simulation of a model gas turbine combustor, Combustion and Flame 137 (2004) 278–294.

[5] Jones WP, Marquis AJ, Vogiatzaki K. Large-eddy simulation of spray combustion in a gas turbine combustor, Combustion and Flame, (2014) 161(1) pp.222–239

[6] Khalil AEE, Gupta AK. Swirling distributed combustion for clean energy conversion in gas turbine applications, Applied Energy, (2011) 88, 3685-3693.

[7] Yehia A Eldrainy, Khalid M Saqr, Hossam S Aly, Mohammad Nazri Mohd Jaafar. CFD insight of the flow dynamics in a novel swirler for gas turbine combustors, International Communications in Heat and Mass Transfer, (2009) 36, 936–941.

[8] Vasudevan A, and Ganesan V. Simulation of Isothermal Flow Field Structure in a Gas Turbine Combustor, SAE Technical Paper 2001-28-0026, 2001, doi:10.4271/2001-28-0026.

[9] Favaloro SC, Nejad AS, and Ahmed SA. Experimental and computational investigation of isothermal swirling flow in an axisymmetric dump combustor, Journal of Propulsion and Power, (1991), 7(3) pp. 348-356.

[10] Benim AC, Escudier MP, Nahavandi A, Nickson AK, Syed KJ, Joos F. Experimental and numerical investigation of isothermal flow in an idealized swirl combustor, International Journal of Numerical Methods for Heat & Fluid Flow, (2010) 20(3), pp.348-370

[11] Koutmos P, McGuirk JJ. Isothermal flow in a gas turbine combustor- A benchmark experimental study, Experiments in Fluids (1989) 7, 344-354

[12] Kenbar AMA, Beltagui SA, Maccallum NRL. Combustion Aerodynamics of a Gas-Fired Furnace with Peripheral Fuel Injection, Experimental Thermal and Fluid Science, (1995)10, pp.335-346.

[13] Foster PJ, Macinnes JM, Schubnell F. Isothermal Modelling of a Combustion System With Swirl: a Computational Study, Combust. Sci. and Tech., (2000) 155, pp. 51-74.

[14] De Ashoke, Zhu Shengrong, Acharya Sumanta, An Experimental and Computational Study of a Swirl-Stabilized Premixed Flame, Journal of Engineering for Gas Turbines and Power, (2010) Vol. 132 / 071503-1.

[15] Feikema D, Chen Ruey-Hung, James FD, Enhancement of Flame Blowout Limits by the Use of Swirl, COMBUSTION AND FLAME, (1990)80: 183-195.

[16] Fureby C, Grinstein FF, Li G, Gutmark EJ. An experimental and computational study of a multi-swirl gas turbine combustor, Proceedings of the Combustion Institute (2007) 31 pp. 3107–3114.

[17] Moin P, Apte SV, Large-eddy simulation for realistic gas turbine combustors, AIAA J. 44 (4) (2006) 698–708.

[18] Yan Ying-wen, Zhao Jian-xing , Zhang Jing-zhou, Liu Yong., Large-eddy simulation of two-phase spray combustion for gas turbine combustors, Applied Thermal Engineering 28 (2008) 1365–1374.

[19]You D, Ham F, Moin P. Large-eddy simulation analysis of turbulent combustion in a gas turbine engine combustor, Center for Turbulence Research Annual Research Briefs 2008.

[20] Luo K, Pitsch H, Pai MG. Center for Turbulence Research Annual Research Briefs 2009.

[21] Bastiaansy RJM, Vremanz AW, Pitsch H, DNS of lean hydrogen combustion with flamelet-generated manifolds, Center for Turbulence Research Annual Research Briefs 2007.

[22] Tolpadi AK. Calculation of two phase flow in gas turbine combustor, ASME J. Engrs. Gas Turbine and Power, (1995) 117(4), pp. 695-703.

[23] Datta A, and Som SK. Combustion and emission characteristics in a gas turbine combustor at different pressure and swirl conditions, Appl. Thermal Engineering, (1999) 19(9), pp. 949-967.

[24] Watanabe H, Matsushita Y, Aoki H, Miura T. Numerical simulation of emulsified fuel spray combustion with puffing and micro-explosion, Combustion and Flame, (2010) 157, pp. 839-852.

[25] Gou Baoyu, Team AG Langrish, David F Fletcher. An assessment of turbulence models applied to the simulation of a two-dimensional submerged jet, Applied Mathematical Modelling (2001) 25 pp. 635-653.

[26] German AE, Mahmud T. Modelling of non-premixed swirl burner flows using a Reynolds-stress turbulence closure, (2005) Fuel 84 pp. 583–594.

[27] Zhu J, and Shih TH. Computation of confined co-flow jets with three turbulence models, Int. J. Numer. Methods Fluids, (1994) 19(10), pp. 939-956.

[28] Karagoz I, Kaya F. CFD investigation of the flow and heat transfer characteristics in a tangential inlet cyclone, International Communications in Heat and Mass Transfer (2007) 34 (9-10) , pp. 1119-1126.

[29] Xia JL, Yadigaroglu G, Liu YS, Schmidli J. Numerical and experimental study of swirling flow in a model combustor, Int. J. Heat Mass Transfer. (1998) 41(11), pp. 1485-1497.

[30]Escue Andrew, Cui Jie. Comparison of turbulence models in simulating swirling pipe flows, Applied Mathematical Modeling, (2010) 34 pp.2840–2849.

[31] Yajun Li, Zheng Hongtao, Yong Mu, Biyong Cheng, Application of Turbulent Models on Simulation of Intense Swirling Flow Combustor, 2011 Asia-Pacific Power and Energy Engineering Conference, APPEEC 2011.

[32] Karim VM, Bart M, and Erik D. Comparative Study of k-ε Turbulence Models in Inert and Reacting Swirling Flows, (2003) AIAA Paper No. 2003-3744.

[33] Joung D and Huh KY. Numerical Simulation of Non-Reacting and Reacting Flows in a 5 MW Commercial Gas Turbine Combustor, (2009) ASME Paper No. GT 2009-59987.

[34] Zeinivand H and Bazdidi-Tehrani F. Influence of stabilizer jets on combustion characteristics and NOx emission in a jet-stabilized combustor, Applied Energy (2012) 92, pp. 348-360.

[35] Dorfner V, Domnick J, Durst F, Kohler R. Viscosity and Surface Tension Effects in Pressure Swirl Atomization, Atomization and Sprays, (1995) vol. 5, pp. 261-285.

[36] Han Z, Parrish Sc, Farell PV, Reitz RD. Modeling Atomization Processes of Pressure-Swirl Hollow-Cone Fuel Sprays, Atomization and Sprays, (1997) vol. 7, pp. 663-684.

[37] Schmidt DP, Nouar I, Senecal PK, Rutland CJ, Martin JK and Reitz RD. Pressure-Swirl Atomization in the Near Field. SAE Paper (1999) 01-0496, SAE.

[38] Senecal PK, Schmidt DP, Nouar I, Rutland CJ, Reitz RD, Corradini ML. Modeling high-speed viscous liquid sheet atomization, International Journal of Multiphase Flow 25 (1999) pp. 1073-1097.

[39] Jianqing Xue, (2004) Computational simulation of flow inside pressure-swirl atomizers, PhD. Thesis, Division of Research and Advanced Studies of the University of Cincinnati.

[40] Shim Young-Sam, Choi Gyung-Min, Kim Duck-Jool, Numerical and experimental study on hollow-cone fuel spray of high-pressure swirl injector under high ambient pressure condition, Journal of Mechanical Science and Technology 22 (2008) pp. 320-329.

[41] Bafekr Sajed Hadi, Shams Mehrzad, Ebrahimi Reza, Shadaram Abdollah, Numerical Simulation of Pressure-Swirl Spray Dispersion by Using Eulerian-Lagrangian Method, Journal of Dispersion Science and Technology, (2010) 32(1) pp. 47-55.

[42] Lee, Chang Sik Kim Hyung Jun, Park Sung Wook, Atomization characteristics and prediction accuracies of hybrid break-up models for a gasoline direct injection spray, Proc. Instn Mech. Engrs Vol. 218 Part D: J. Automobile Engineering.

[43] Bashirnezhad K, Moghiman M, Amoli M. Javadi, Tofighi F, Zabetnia S. Effect of Fuel Spray Angle on Soot Formation in Turbulent Spray Flames, (2009) International Journal of Aerospace and Mechanical Engineering 3:4.

[44] Ma L, Zhu S, Rodrigues HRC, Tummers MJ, Van Der Meer TH, Roekaerts DJEM. Numerical investigation of ethanol spray-inhot-coflow flame using steady flamelet model, Çeşme, Izmir, Turkey, September 8-13, 2013.

[45] Pandey Vivek, De Ashoke, Kushari Abhijit. Numerical Investigation of Combustion Characteristics in a Liquid Fuelled Can Combustor, GTINDIA 2012-9719, pp. 571-579.

[46] Zeoli N, Gu S. Numerical modelling of droplet break-up for gas atomization, Computational Materials Science, (2006) 38 pp. 282–292.

[47] Tratnig Andreas, Brenn Gunter. Drop size spectra in sprays from pressure-swirl atomizers, International Journal of Multiphase Flow, (2010) 36 pp. 349–363.

[48] Spalding DB. Mixing and chemical reaction in steady confined turbulent flames. In 13th Symp. (Int'l.) on Combustion. The Combustion Institute, 1970.

[49] Magnussen BF and Hjertager BH. On mathematical models of turbulent combustion with special emphasis on soot formation and combustion, In 16th Symp. (Int'l.) on Combustion. The Combustion Institute (1976).

[50] Khalid M Saqr, Hossam S Aly, Mohsin M Sies, Mazlan A Wahid, Effect of free stream turbulence on NOx and soot formation in turbulent diffusion CH4-air flames, International Communications in Heat and Mass Transfer (2010) 37 pp. 611–617.

[51] Gassoumi Taoufik, Guedri Kamel, Said Rachid, Numerical Study of the Swirl Effect on a Coaxial Jet Combustor Flame Including Radiative Heat Transfer, Numerical Heat Transfer, Part A, (2009) 56: 897–913.

[52] Kamnis S, Gu S, Numerical modelling of propane combustion in a high velocity oxygen–fuel

thermal spray gun, Chemical Engineering and Processing (2006) 45 pp. 246–253.

[53] Magnussen BF. On the Structure of Turbulence and a Generalized Eddy Dissipation Concept for Chemical Reaction in Turbulent Flow. Nineteeth AIAA Meeting, St. Louis, 1981.

[54] Magnussen BF. The Eddy Dissipation Concept, Presented at task leader meeting, Lund, Sweden, 1989.

[55] Dmitry A Lysenko, Ivar S Ertesvag, Kjell Erik Rian, Numerical Simulations of the Sandia Flame D Using the Eddy Dissipation Concept, Flow, Turbulence and Combustion, December 2014, Volume 93, Issue 4, pp 665-687.

[56] Kai CUI, Bing LIU, Yuxin WU, Hairui YANG, Junfu LU, Hai ZHANG, Numerical Simulation of Oxy-coal Combustion for a Swirl Burner with EDC Model, Chinese Journal of Chemical Engineering, (2014) 22 (2) Pages 193–201.

[57] Graca M, Duarte A, Coelho PJ, Costa M. Numerical simulation of a reversed flow small-scale combustor, Fuel Processing Technology, (2013) Volume 107, Pages 126–137.

[58] Spalding DB. Combustion and Mass Transfer, Pergamon Press, Oxford (1979).

[59] Favre A. Statistical Equations of Turbulent Gases, in Problems of Hydrodynamics and Continuum Mechanics, SIAM, Philadelphia, (1969). pp. 231–266.

[60] Sivathanu YR, and Faeth GM, Generalized State Relationships for Scalar Properties in Nonpremixed Hydrocarbon/Air Flames, COMBUSTION AND FLAME (1990) 82 pp. 211-230.

[61] Pope SB. Combustion modelling using probability density function method, Chapter 11, 1990, Americann institute of aeronautics and astronautics.

[62] Hudong Chen, Shiyi Chen, Robert H. kraichnan, Probablity distribution of a stochastically advanced scalar field, Physical review letters, The American physical society, 1989.

[63] Pope SB. PDF methods for turbulent reactive flows, Progress in Energy and Combustion Science, (1985) 11, pp. 119-192.

[64] Pope **S**B. Stochastic lagrangian models for turbulence, Annual Reviews of Fluid Mechanics, (1994) Vol. 26, 23--63.

[65] Dopazo C, in: Libby PA, Williams FA. (Eds.), Turbulent Reactive Flows, Academic Press, London, 1994.

[66] Pope SB. Turbulent Flow, Cambridge Univ. Press, Cambridge, 2000.

[67] Evans M, Hastings N, Peacock B. Statistical Distributions, 3rd edn, Wiley Series in Probability and Statistics, (2000) John Wiley & Sons, New York.

[68] Williams FA. Description of Turbulent Diffusion Flames, (1975) PlenumPress, 1st edition.

[69] Peters N. Laminar diffuusion flamelet models in non-premixed turbulent combustion, Progress in Energy and Combustion Science, (1984) vol. 10, pp. 319.

[70] Bray KN, and Peters N, Laminar Flamelets in Turbulent Flames. In P. A. Libby and F. A. Williams, editors, Turbulent Reacting Flows, pages 63–94. Academic Press, 1994.

[71] Peters N. Turbulent Combustion, (2000) Cambridge monographs on mechanics, Cambridge University Press, Cambridge UK.

[72] Li G, Naud B, Roekaerts D. Numerical investigation of a bluff-body stabilised nonpremixed flame with differential Reynolds-stress models, Flow, Turbul. Combust., (2003) 70, pp. 211–240.

[73] Hollmann C, Gutheil E. Modeling of turbulent spray diffusion flames ncluding detaied chemistry, Twenty-sixth Symp. (Int) on Combustion, (1996) pp. 1731-1738.

[74] Fallot L, Gonzalez M, Elamraoui R, Obounou M. Modelling finite rate chemistry effects in non premixed turbulent combustion: Test on the bluff-body stabilized flame, Combustion and Flame (1997) 110 pp. 298 318.

[75] Seunghwan Keum, Hong G. Im, and Dennis N. Assanis, A spray-interactive flamelet model for direct injection engine combustion, Combust. Sci. Technol., (2012) 184 pp.469–488.

[76] Baba Yuya, Kurose Ryoichi, Analysis and flamelet modelling for spray combustion, J. Fluid Mech. (2008), vol. 612, pp. 45–79.

[77] Merci B, Dick E, Vierendeels J, Roekaerts D, Peeters TWJ. Application of a new cubic turbulence model to piloted and bluff-body diffusion flames, Combust. Flame, (2001) 126, pp. 1533–1556.

[78] Hossain M, Malalasekera W. A combustion model sensitivity study for CH_4/H_2 bluff-body stabilized flame, Proc. IMechE Part C: J. Mech. Engg. Sci., (2007) 221, pp. 1377-1390.

[79] Richter H, Howard JB. Formation of polycyclic aromatic hydrocarbons and their growth to soot – a review of chemical reaction pathways, Prog. Energy Combust. Sci. (2000) 26, pp. 565–608.

[80] Mansurov ZA. Soot formation in combustion processes, Combust. Explo. Shock Waves, (2005) 41 (6) 727–744

[81] Haynes BS, Gg. Wagner H. Soot formation. Prog. Energy Combust.Sci., (1981) 7:229–273.

[82] Glassmann I. Soot formation in combustion processes. In Twenty-Second Symposium (International) on Combustion, The Combustion institute (1988) pages 295–311.

[83] Frenklach M. Reaction mechanism of soot formation in flames. Phys. hem. Chem. Phys., (2002) 4:2028–2037.

[84] Mansurov ZA. Soot formation in combustion processes (Review) Combustion, Explosion and shock waves, (2005) Vol. 41, No. 6, pp. 727-744.

[85] Kennedy Ian M. Models of soot formation and oxidation, Prog. Energy Combust. Sci. (1997) Vol. 23, pp. 95-132.

[86] Calcote HF, Manos DM. Effect of molecular structure on incipient soot formation, Combustion and Flame, (1983) vol. 49, pp. 289.

[87] Khan M and Greeves G. A Method for Calculating the Formation and Combustion of Soot in Diesel Engines. In Afgan NH and Beer JM. editors, Heat Transfer in Flames, chapter 25. Scripta, Washington DC, 1974.

[88] Tesner PA, Tsygankova LP, Guilazetdinov LP, Zuyev VP, Loshakova GV. The formation of soot from aromatic hydrocarbons in diffusion flames of hydrocarbon-hydrogen mixtures. Combustion and Flame, (1971) 17 pp. 279–285.

[89] Young KJ, Moss JB. Modelling sooting turbulent jet flames using an extended flamelet technique. Combust. Sci. and Tech, 105:33–53, 1995

[90] Kollmann W, Kennedy IM, Metternich M, Chen JY. Application of a soot model to a turbulent ethylene diffusion flame. Chapter; Soot Formation in Combustion,Volume 59 of the series Springer Series in Chemical Physics pp 503-526.

[91] Kronenburg A, Bilger RW, Kent JH. Modeling soot formation in turbulent methane-air jet diffusion flames. Combustion and Flame, (2000) 121 pp. 24– 40.

[92] Bai XS, Balthasar M, Mauss F, Fuchs L. Detailed soot modeling in turbulent jet diffusion flames, Twenty-Seventh Symposium (International) on Combustion, The Combustion Institute, (1998) pp. 1623–1630.

[93] Kennedy IM, Kollmann W, Chen JY. A model for the soot formation in laminar diffusion flame, Combust. Flame, (1990) 81 73–85.

[94] Coelho PJ, Carvalho MG. Modelling of soot formation and oxidation in turbulent diffusion flames, Journal of thermophysiscs and heat transfer, (1995) Vol. 9, No. 4.

[95] Moss JB, Stewart CD, Young KJ. Modeling soot formation and burnout in a high temperature laminar diffusion flame burning under oxygen-enriched conditions, Combust. Flame (1995) 101 pp. 491–500.

[96] Kumar Sunil, Ray Anjan Kale SR. A soot model for transient, spherically symmetric n-heptane droplet combustion, Combust. Sci. and Tech., (2002) 174(9): pp. 67-102.

[97] Christopher W. Lautenberger, John L. de Ris, Nicholas A. Dembsey, Jonathan R. Barnett, Howard R. Baum. A simplified model for soot formation and oxidation in CFD simulation of non-premixed hydrocarbon flames, Fire Safety Journal 40 (2005) 141–176.

[98] Brookes SJ and Moss JB. Predictions of soot and thermal radiation properties in confined turbulent jet diffusion flames. Combustion and Flame, (1999) 116 pp. 486–503.

[99] Sivathanu YR and Gore JP. Effects of Gas-Band Radiation on Soot Kinetics in Laminar Methane/Air Diffusion Flames, Combustion and Flame, (1997) 110 pp. 256-263.

[100] Kaplan CR, Patnaik G and Kailasanath K. Universal Relationships in Sooting Methane-Air Diffusion Flames, Combustion Science and Technology, (1998) 13 pp. 39-65.

[101] Mandal Bijan Kumar, Datta Amitava and Sarkar Amitava, A Computational Study of the Soot Formation in Methane-Air Diffusion Flame During Early Transience Following Ignition, Engineering Letters, 16:3, EL_16_3_04.

[102] Smooke MD, McEnally CS, Pfefferle LD, Hall RJ and Colket MB. Computational and experimental study of soot formation in a coflow, laminar diffusion Flame, Combustion and Flame, (1999) 117 (1-2) pp. 117- 139.

[103] Moss JB, Aksit IM. Modelling soot formation in a laminar diffusion flame burning a surrogate kerosene fuel, Proc. Combust. Inst. (2007) 31 pp. 3139–3146.

[104] Wen Z, Yun S, Thomson MJ, Lightstone MF. Modeling soot formation in turbulent kerosene/air jet diffusion flames, Combust. Flame, (2003) 135 pp. 323– 340.

[105] Watanabeyz H, Kurosez R, Komoriz S, Pitsch H. Center for Turbulence Research, Proceedings of the Summer Program 2006.

[106] Christopher W. lautenberger, John L. de Ris, Nicholas A. Dembesey, Jonathan R. Barnett, Howard R. Baum, A simplified model for soot formation and oxidation in CFD simulation in CFD simulation of non-premixed hydrocarbon flames.

[107] Wang Hu, Reitz Rolf Deneys, Yao Mingfa, Yang Binbin, Jiao Qi, Qiu Lu, Development of an n-heptane-n-butanol-PAH mechanism and its application for combustion and soot prediction, Combustion and Flame, (2013) 160 pp. 504–519.

[108] Massimiliano Di Domenico, Peter Gerlinger, Manfred Aigner, Development and validation of a new soot formation model for gas turbine combustor simulations, Combustion and Flame, (2010) 157 pp. 246–258.

[109] Siegel R and Howell JR. Thermal Radiation Heat Transfer. Hemisphere Publishing Corporation, Washington DC, 1992.

[110] Fiveland WA. A discrete-ordinates method for predicting radiative heat transfer in axisymmetric enclosure. ASME 82-HT-20, 1982.

[111] Carlson BG, Lathrop KD. Transport theory—the method of discrete ordinates. In: Greenspan H, Kelber CN, Okrent D, editors. Computing methods in reactor physics. London: Gorden and Breach; 1993. p. 165–266.

[112] Howell JR. The Monte Carlo Method in Radiative Heat Transfer, J. Heat Transfer, (1998), Vol. 120, pp. 547-560.

[113] Stewart FR and Cannon P. The Calculation of Radiative Heat Flux in a Cylindrical Furnace Using the Monte Carlo Method, Trans. Canadian Soc. Mech. Engg., (1971) Vol. 3, No. 1, pp. 10-16.

[114] David Joseph, Patrice Perez, Mouna El Hafi, Benedicte Cuenot CERFACS, Toulouse, France Discrete Ordinates and Monte Carlo Methods for Radiative Transfer Simulation Applied to Computational Fluid Dynamics Combustion Modeling, ASME Journal of Heat Transfer, MAY 2009, Vol. 131 / 052701-1.

[115] Malalasekera W, Versteeg HK, Henson JC, Jones JC. Calculation of radiative heat transfer in combustion systems. Clean Air, (2002) 3 (1), pp. 113-143.

[116] Chandrashekhar S. 1950, Radiative Transfer, Clarendon, Oxford.

[117] Theory guide Ansys Fluent 13.0.

[118] Beltrame A, Porshnev P, Merchan-Merchan W, Saveliev A, Fridman A, Kennedy LA. Petrova O, Zhdanok S, Amouri F, Charon O. Soot and NO formation in methane–oxygen enriched diffusion flames, (2001)Volume 124, Issues 1–2, Pages 295–310.

[119] Adams BR and Smith PJ. Modelling Effects of Soot and Turbulence-Radiation Coupling on Radiative Transfer in an Industrial Furnace, HTD, (1994) Vol. 276, pp. 177-190.

[120] Adams BR and Smith PJ. Three-dimensional Discrete Ordinates Modelling of Radiative Transfer in Industrial-Scale Furnaces, HTD, (1992) Vol. 203, pp. 137-144.

[121] Fengshan Liu, Hongsheng Guo, Gregory J. Smallwood, Omer L. Gu1lder, Effects of gas and soot radiation on soot formation in a co-flow laminar ethylene diffusion flame, Journal of Quantitative Spectroscopy & Radiative Transfer, (2002) 73 pp. 409–421.

[122] Watanabeyz H, Kurosez R, Komoriz S, Pitsch H. Effects of radiation on spray flame characteristics and soot formation, Combustion and Flame, (2008) Volume 152, Issues 1–2, Pages 2–13.

[123] Fenimore CP and Jones GW. Oxidation of soot by hydroxyl radicals. J. Phys. Chem., (1967) 71 pp. 593–597.

[124] Gary N. Coleman and Richard D. Sandberg, A Primer on Direct Numerical Simulation of Turbulence Methods, Procedures and Guidelines, (March 2010)] , Technical Report AFM-09/01a.

[125] Launder BE and Spalding DB. The numerical computation of turbulent flows, Comput. Methods Appl. Mech. Eng., (1974) Vol. 3, pp. 269-289.

[126] Rahim A, Singh SN and Veeravalli SV. Liner dome shape effect on the annulus flow characteristics with and without swirl for a can-combustor model, Proc. IMechE Vol. 221 Part A: J. Power and Energy, pp 359-369.

[127] Lefebvre AH, Ballal DR. Gas turbine combustion: alternative fuel and emissions. Taylor and francis group; 2010.

[128] C.H. Wang, J.H. Wu, S.J. Liu, L.P. Kou, Characteristic of turbulent flow in the jackets with triangular helical ducts, Chapter · November 2013 DOI: 10.1201/b16125-6, In book: Chemical Engineering III, pp.23-28.

[129] Bradshaw P, Cebeci T, Whitelaw JH. Engineering calculation methods for turbulent flow, (1981), Academic press, London.

[130] Lefebvre AH and Wang XF. Mean drop sizes from pressure-swirl nozzles, Journal of Propulsion and Power, (1987) Vol. 3, No. 1 pp. 11-18.

[131] Morsi SA, Alexander AJ. An investigation of particle trajectories in two phase flow system, J. Fluid Mech., (1972) 55(2) pp. 193-208.

[132] Ranz WE, Marshall WR. Jr. Evaporation from Drops, Part I, Chem Eng Prog. (1952) 48(3) pp. 141-146.

[133] Ranz WE, Marshall WR. Jr. Evaporation from Drops, Part II, Chem Eng Prog. (1952) 48(4) pp. 173-180.

[134] Versteeg HK, and Malalasekera W. An Introduction to Computational Fluid Dynamics The Finite Volume Method. Second Edition, (2007) Pearson Education, Harlow, England; 1995.

[135] Kundu KP, Penko PF, and Yang SL. Simplified Jet-A/Air combustion mechanisms for calculation of NOx emissions. 1998; Paper No. AIAA-98-3986.

[136] Li G, Naud B and Roekaerts D. Numerical investigation of a bluff-body stabilised nonpremixed flame with differential Reynolds-stress models, Flow, Turbul. Combust., (2003) 70, pp. 211–240.

[137] Modest MF, Radiative heat transfer, Second edition, vol. 1, McGraw-Hill Inc., NY, USA, 1993.

[138] Beji Tarek, Zhang Jianping and Delichatsios Michael. Soot Formation and Oxidation in Fires from Laminar Smoke Point Measurements, The Institute for Fire Safety Engineering Research and Technology (FireSERT), University of Ulster, Newtownabbey, BT37 0QB, Northern Ireland.

[139] Hall RJ, Smooke MD, Colket MB. In Physical and Chemical Aspects of Combustion: A Tribute to Irvine Glassman, F.L. Dryer and R.F. Sawyer (Ed.), Gordon & Breach, 1997, p. 189.

[140] Harris SJ and Weiner AM. Surface growth of soot particles in premixed ethylene/air flames. Combust. Sci and Tech, (1983) 31 pp.155–167.

[141] Thomas F. DeBold, laminar smoke points of coflowing diffusion flames in microgravity, Master of Science, 2012, Department of Fire Protection Engineering, University of Maryland.

[142] Young KJ, Stewart CD, Moss JB. Soot formation in turbulent nonpremixed kerosene-air flames burning at elevated pressure: Experimental measurement, Symposium (International) on Combustion, (1994) 25 pp. 609-617.

[143] Shih TH, Liou WW, Shabbir A, Yang Z and Zhu J. A new k-ε eddy viscosity model for high Reynolds number turbulent flows, Computer Fluids, (1995) 24(3), pp. 227-238.

[144] Paul SC, Paul MC. Radiative heat transfer during turbulent combustion process, Int. Commun. Heat Mass Transfer, (2010) 37, pp. 1–6.

[145] Ghose P, Patra J, Datta A, Mukhopadhyay A. Effect of Air Flow Distribution on Soot Formation and Radiative Heat Transfer in a Model Liquid Fuel Spray Combustor Firing Kerosene, International Journal of Heat and Mass Transfer, (2014) 74, pp. 143-155.

[146] Basak A, Patra J, Ganguly R, Datta A. Effect of transesterification of vegetable oil on liquid flow number and spray cone angle for pressure and twin fluid atomizers, (2013) Fuel, 112, pp. 347-354.